AN OCEAN SURFACE WIND VECTOR MODEL FUNCTION FOR A SPACEBORNE MICROWAVE RADIOMETER AND ITS APPLICATION

by

SEUBSON SOISUVARN
M.S. University of Central Florida, 2001

A dissertation submitted in partial fulfillment of the requirements
for the degree of Doctor of Philosophy
in the School of Electrical Engineering and Computer Science
in the College of Engineering and Computer Science
at the University of Central Florida
Orlando, Florida

Fall Term
2006

Major Professor: W. Linwood Jones

ABSTRACT

Ocean surface wind vectors over the ocean present vital information for scientists and forecasters in their attempt to understand the Earth's global weather and climate. As the demand for global wind velocity information has increased, the number of satellite missions that carry wind-measuring sensors has also increased; however, there are still not sufficient numbers of instruments in orbit today to fulfill the need for operational meteorological and scientific wind vector data. Over the last three decades operational measurements of global ocean wind speeds have been obtained from passive microwave radiometers. Also, vector ocean surface wind data were primarily obtained from several scatterometry missions that have flown since the early 1990's. However, other than SeaSat-A in 1978, there has not been combined active and passive wind measurements on the same satellite until the launch of the second Advanced Earth Observing Satellite (ADEOS-II) in 2002. This mission has provided a unique data set of coincident measurements between the SeaWinds scatterometer and the Advanced Microwave Scanning Radiometer (AMSR).

AMSR observes the vertical and horizontal brightness temperature (T_B) at six frequency bands between 6.9 GHz and 89.0 GHz. Although these measurements contain some wind direction information, the overlying atmospheric influence can easily obscure this signal and make wind direction retrieval from passive microwave measurements very difficult. However, at radiometer frequencies between 10 and 37 GHz, a certain linear combination of vertical and horizontal brightness temperatures causes the atmospheric dependence to be nearly cancelled and surface parameters such as wind speed, wind direction and sea surface temperature to dominate the resulting signal. This brightness temperature combination may be expressed as AT_{BV}-T_{BH},

where *A* is a constant to be determined and the T_{BV} and T_{BH} are the brightness temperatures for the vertical and horizontal polarization respectively. In this dissertation, an empirical relationship between the AMSR's AT_{BV}-T_{BH} and SeaWinds' surface wind vector retrievals was established for three microwave frequencies: 10, 18 and 37 GHz. This newly developed model function for a passive microwave radiometer could provide the basis for wind vector retrievals either separately or in combination with scatterometer measurements.

To my parents

Vice Admiral Vichit Soisuvarn, Royal Thai Navy (Ret.) and Nangnoi Soisuvarn

ACKNOWLEDGMENTS

This dissertation would not be possible without the guidance and assistance from many people. First of all, I am grateful to my advisor Professor W. Linwood Jones who has patiently mentored and provided guidance through my graduate study. I also would like to thank him for his professional experience that he brought to classroom and the research, from which I have learned a lot, and finally, I want to thank him for providing financial support through out my Ph.D. graduate program.

I really appreciate the kind guidance from Dr. Zorana Jelenak, and I am thankful for her donating her precious time to spend on my research. Without her suggestion, this dissertation would not be possible. I also thank her for serving as my committee member.

I would like to thank Dr. R. Scott Dunbar of JPL who provided AMSR overlay data that used in this dissertation and also patiently answered questions about the data. I also want to thank JPL for the SeaWinds science data product used through their PODAAC oceans website.

I want to thank Dr. Laurence Connor who made GDAS data available and provided great IDL codes for GDAS/SeaWinds/AMSR collocations. I also want to thank Dr. Paul Chang who provided the powerful computers at the NOAA Science Center where the intensive data processing was performed.

Finally I want to thank my committee members: Professor Takis Kasparis, Mr. James Johnson and Dr. Stephen Wiechecki Vergara who provided detailed suggestions and corrections.

This dissertation was sponsored by a grant from the National Polar-orbiting Operational Environmental Satellite System Integrated Program Office (NPOESS IPO).

TABLE OF CONTENTS

LIST OF FIGURES

LIST OF TABLES

LIST OF ACRONYMS/ABBREVIATIONS

ADEOS	Advanced Earth Observing Satellite
AMI	Active Microwave Instrument
AMSR	Advanced Microwave Scanning Radiometer
CMIS	Conical Scanning Microwave Imager/Sounder
DMSP	Defense Meteorological Satellite Program
ERS	European Remote Sensing Satellite
ESA	European Space Agency
EUMETSAT	European Organization for the Exploitation of Meteorological Satellites
GDAS	Global Data Assimilation System
GMF	Geophysical Model Function
JAXA	Japan Aerospace Exploration Agency (formerly NASDA)
JPL	Jet Propulsion Laboratory
LEO	Low Earth Orbit
NASA	National Aeronautics and Space Administration
NASDA	National Space Development Agency (currently JAXA)
NCEP	National Centers for Environmental Prediction
NESDIS	National Environmental Satellite, Data, and Information Service
NPOESS	National Polar-orbiting Operational Environmental Satellite System

NOAA	National Oceanic and Atmospheric Administration
NRCS	Normalized Radar Cross Section
NRL	Naval Research Laboratory
NSCAT	NASA Scatterometer
NWP	Numerical Weather Prediction
QuikSCAT	Quick Scatterometer
SASS	Seasat-A Satellite Scatterometer
SSM/I	Special Sensor Microwave/Imager
SST	Sea Surface Temperature
WVC	Wind Vector Cell

CHAPTER ONE: INTRODUCTION

Remote sensing is broadly defined as the acquisition of information about an object or medium without being in physical contact with it. In practice, remote sensing is commonly utilized for the observation of environmental parameters of the Earth or a planet at great distances from aircraft, spacecraft, or satellites. Most remote sensing techniques makes use of the electromagnetic (EM) radiation emitted or reflected from the object being observed. Objects interact differently within the electromagnetic spectrum according to their EM properties and geophysical conditions. With a large variety of EM interaction between the objects/media, over the entire range of the electromagnetic spectrum from long wavelength radio waves, microwave, infrared, visible, ultraviolet, x-ray and gamma-rays, it is possible to use remote sensing techniques for gathering information about the Earth's geophysical environment.

The information acquired from a remote sensing instrument, particularly from an electromagnetic sensor, is generally classified into three kinds as spatial information, spectral information and intensity information [1]. Spatial information is more important when studying phenomena that have small spatial scale variability and contrast and high spatial resolution information is needed such as a two-dimensional image. Spectral information is required where the scene exhibits high variability to EM wavelength (frequency), such as classification of vegetation type using multi-spectral imagery. Intensity information becomes more important than spatial and spectral information in an application where radiometric intensity information is sensitive to the changes of the phenomenon being studied. An example of this is in the retrieval of the Earth's atmosphere and surface geophysical parameters.

Microwave sensors play a dominant role in environmental remote sensing of the Earth's atmosphere and surface that contain water in vapor, liquid and frozen forms, such as water vapor, cloud liquid water, rain, sea surface temperature, soil moisture and sea ice. Microwave sensors operate independent of the solar illumination, which means observations are possible all day and night independent of sunlight. In addition, the atmosphere is mostly transparent to microwaves, which makes them capable of penetrating through clouds and to some extent through rain to gather information about the surface. The microwave transmission through the atmosphere is compared with that for other EM spectral regions in Fig. 1. Moreover, microwave observations provide information that is complementary to that available in the visible and infrared regions [1 – 4].

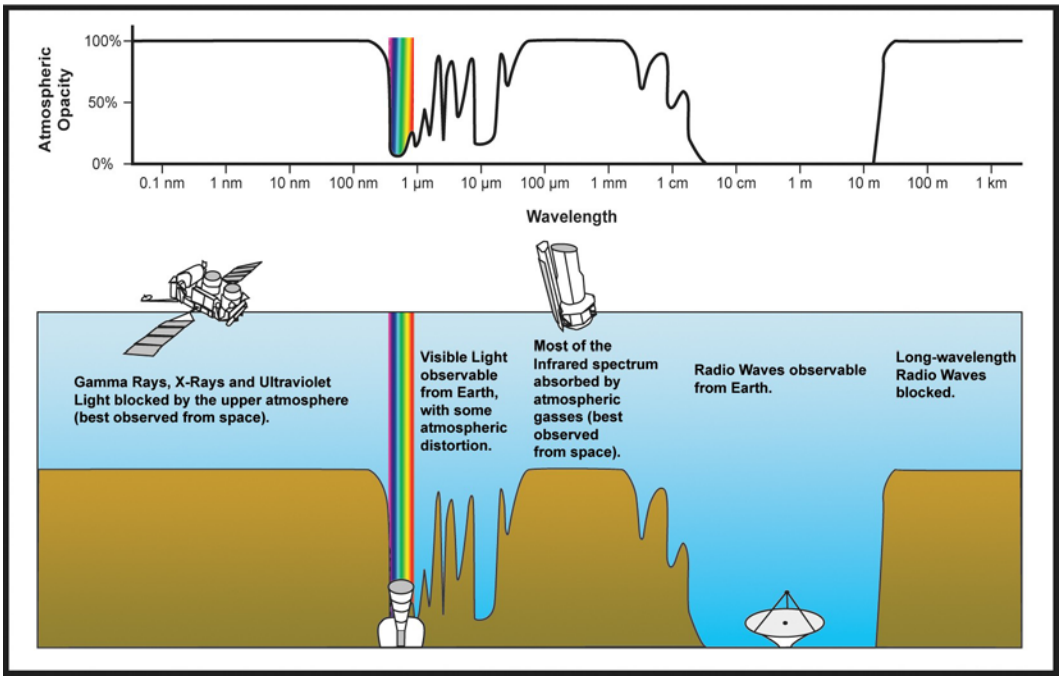

Figure 1: Atmospheric transmissivity in electromagnetic spectrums [*from NASA*].

Microwave remote sensing is classified into two categories: active and passive. In active microwave remote sensing, the measurements are made by radar, with the transmitter providing the source of electromagnetic illumination and the receiver collects the energy that is reflected or scattered back from the object or scene under measurement. The characteristics of the energy received depend on the scattering properties of the object. An active microwave instrument that is specifically designed to measure ocean surface wind vectors (speed and direction) is known as a scatterometer.

In contrast to active remote sensing, passive microwave remote sensing simply receives the naturally emitted blackbody radiation from the scene that is illuminated by the sensor antenna field of view. A passive microwave instrument is commonly called a microwave radiometer and normally operates in multi-frequency and dual linear polarized channels. Because of the significant changes in microwave emissivity with frequency for many physical media, simultaneous observations at multiple channels are capable of retrieving atmospheric and oceanic parameters such as water vapor, cloud liquid water, rain rate, sea surface temperature (SST) and near-surface wind speed.

Frequently, the geophysical parameter of interest may not be measured directly using remote sensing; however, some other variables, which are highly correlated with the parameter of interest, can be measured. For example, while the surface wind vector can not be measured directly by a scatterometer, there exists a unique relationship between wind vector and the wind roughened surface parameter called the normalized radar cross section (NRCS), which can be measured. Using an empirical relationship known as the Geophysical Model Function (GMF), the wind vector can be inferred indirectly from the NRCS measurement. Another example is that oceanic and atmospheric parameters may be related to the radiation intensity measured by a

radiometer and are proportional to the equivalent physical temperature of a blackbody that is also known as a brightness temperature (T_B). Using a non-linear algorithm, these geophysical parameters can be inferred from multi-channel microwave radiance measurements.

A unique feature of the Earth's surface is the World oceans that cover approximately three quarters (71%) of the entire earth's surface as shown in Fig. 2. This vast amount of the water undoubtedly influences the global weather and climate in general because oceans currents distribute the ocean's stored heat and moisture to the atmosphere. The surface wind plays a dominant role in the ocean transport mechanisms; and because of the Coriolis forces of earth rotation, currents flow in clockwise rotation in the northern hemisphere and counter-clockwise in the southern hemisphere as depicted in Fig. 3.

Further, in the atmosphere one of the most extreme weather events that form over oceans are tropical cyclones, also known as hurricanes or typhoons depending on where they occur. Over the years, hurricanes have caused more destruction in the United States than any other type of natural disaster. The years 2004 and 2005 have been particularly destructive in Florida and the Gulf States, and the expectation is that high hurricane activity will persist for years to come. The best way to minimize the financial and social impact of hurricanes is through preparedness, which relies on monitoring storms and predicting their growth and movement as they develop and make landfall. The accurate and timely knowledge of the oceanic winds would greatly improve storms prediction and provide more timely warning. Further, surface wind information is currently one of the essential parameter required by numerical weather prediction (NWP) models. Therefore, the accurate measurement of the ocean surface wind, both in magnitude and direction, is vital information for NWP modelers, scientist and forecasters in their attempt to understand the Earth's global weather and climate for prompt and accurate forecasting.

The advent of the Earth orbiting satellites makes the global near-surface wind monitoring possible. Compared to a point measurement by ships or buoys, satellite measurements provide nearly global coverage with much more frequent observations. The wide coverage capability of low earth orbit (LEO) satellites allows monitoring of rapidly changes in surface wind conditions and the overlying atmosphere. The long duration and repetitive observation of remote sensing satellites also allows for long-term time series study of global weather and climate changes.

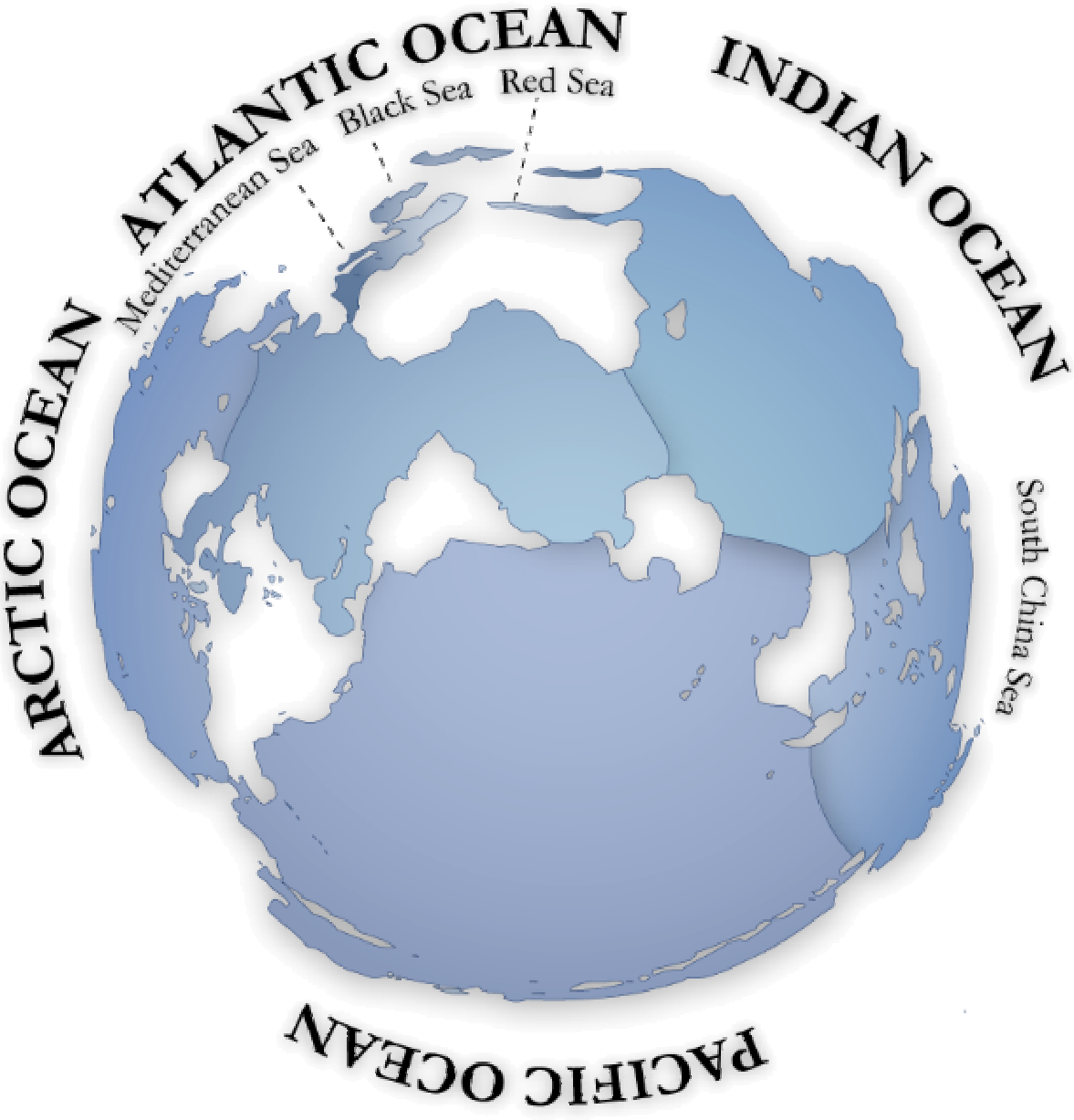

Figure 2: The World oceans [*from http://en.wikipedia.org/wiki/Image:Oceans.png*].

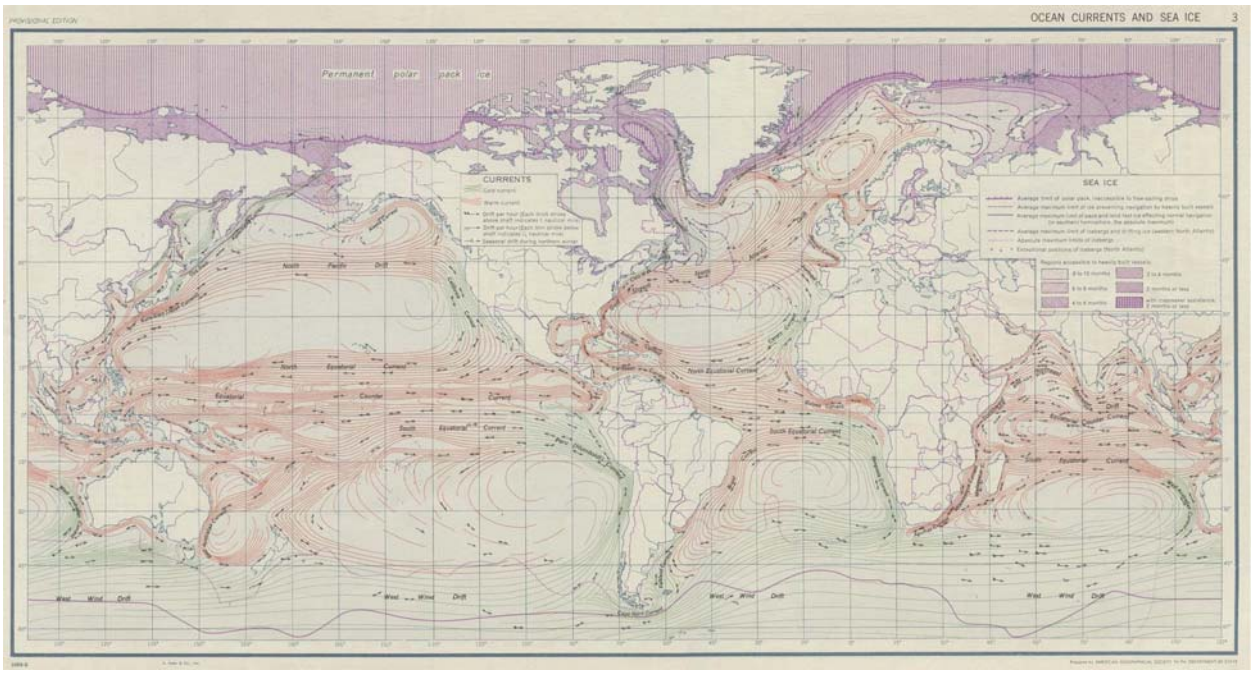

Figure 3: Ocean current circulation [*from Univ. of Texas: http://www.lib.utexas.edu/maps/world_maps/ocean_currents_1943.jpg*].

The first spaceborne wind scatterometer, on NASA's SeaSat mission in 1978, proved that the global ocean surface wind vector (speed and direction) retrievals from space are possible [5, 6]. This mission was followed by a series of satellite scatterometers that started with the European Remote Sensing Satellite (ERS-1) Active Microwave Instrument (AMI) in the early 1990's [7]. But, there have never been sufficient numbers of instruments simultaneously in operation to fulfill either operational meteorological or scientific requirements.

Most operational meteorological satellites carry passive microwave radiometers such as the series of SSM/I instruments on board the Defense Meteorological Satellite Program (DMSP) satellites. These microwave imagers are capable of accurately measuring oceanic surface wind speed but not wind direction. However this has changed with the launch of the first fully

polarimetric microwave radiometer, WindSat, built and launched by the U.S. Naval Research Laboratory, Washington DC in January 2003. The WindSat instrument is capable of measuring full wind vector information [8]. Since a conical scanning microwave radiometer also provides other valuable oceanic and atmospheric geophysical information such as sea surface temperature (SST), integrated water vapor, cloud liquid water, and rain rate, it would be highly beneficial to combine active and passive microwave technologies to obtain improved observation of both the ocean surface wind and other atmospheric and oceanic geophysical parameters.

The Advanced Earth Observing Satellite (ADEOS)-II also known as Midori-II was launched in December 2002 by the Japan Aerospace Exploration Agency (JAXA) formerly known as the National Space Development Agency (NASDA). ADEOS-II carried five Earth observing sensors, with two being the Advanced Microwave Scanning Radiometer (AMSR) and the SeaWinds scatterometer. This was the first satellite mission (since SeaSat) that carried both a microwave scatterometer and a radiometer, thus providing an opportunity to explore the possibility of combining passive and active measurement techniques for the improved retrieval of the global ocean surface wind vectors. Even though the ADEOS-II operation terminated prematurely in October 2003 due to the failure of the satellite power system, sufficient data were collected to allow for the evaluation of this exciting new combined active/passive remote sensing technique.

AMSR was a microwave radiometer that acquired brightness temperature measurements between 6.9 GHz and 89 GHz [9]. Unlike a fully polarimetric radiometer, such as WindSat, the AMSR only observed the principle polarizations (vertical and horizontal) from six frequency channels. Although the vertical and horizontal brightness temperatures depend on wind velocity, the contribution of the wind direction signal to overall brightness temperature measurements is

quite small, especially for low wind speeds, and it is easily obscured by the contribution from other atmospheric parameters, such as cloud liquid water and water vapor at higher frequencies and sea surface temperature at lower frequencies. Thus, AMSR brightness temperatures alone do not contain sufficient information to retrieve wind direction with the required accuracy of < 20°. However, a linear combination between the vertical and horizontal brightness temperatures was found to contain relatively strong wind directional signals [10 – 12]. This brightness temperature combination is mostly independent of the atmosphere and is predominantly a function of sea surface temperature (SST), wind speed and direction. The linear combination may be expressed as AT_{BV}-T_{BH}, where A is a constant dependent on frequency [12], and the T_{BV} and T_{BH} are the brightness temperatures for the vertical and horizontal polarization respectively.

The stronger sensitivity of this radiometric combination on wind direction provides a potential tool for wind vector retrieval from a passive microwave radiometer at moderate to high wind speeds [10 – 12]. However for low to moderate wind speed, the wind direction signal is relatively weak and still lies within the instrument noise level. Therefore full wind vector retrievals from solely passive microwave measurements using V- and H-pol measurements alone or their linear combination are not possible for all wind speed regimes.

On the other hand, with multi-azimuth look backscatter measurements from a microwave scatterometer, it is possible to measure the ocean wind vector. To retrieve ocean surface wind vector information from this scatterometer measurement, a point on the ocean surface must be observed at multiple-look azimuth angles (both forward and aft viewing). The SeaWinds that flew on ADEOS-II was a Ku-band scatterometer that utilized a conically scanning geometry while acquiring measurements using outer beam vertical and inner beam horizontal polarization. As the satellite moves, multiple points on the ocean surface were observed with the SeaWinds

scatterometer, first from forward look V-pol, followed by H-pol, and then the aft look H-pol, finally followed by V-pol respectively. These measurements were collocated within one wind vector cell and used in a geophysical retrieval algorithm. In this way, an azimuthal diversity between measurements was achieved that is necessary for unambiguously deriving the wind vector.

The wind vector retrievals from scatterometer measurements acquired today are generally better than the scientific accuracy requirement (~ 2 m/s speed and < 20° direction) [13]. However, at present, there are no future plans for a new Ku-band wind scatterometer to fly in space and fulfill the increasing wind vector data demand. Because the scatterometer is a high cost instrument to build, an alternative lower-cost instrument or technique to infer ocean wind direction is highly desirable.

This dissertation investigates combining passive and active microwave measurements for wind vector retrievals from space. We use the radiometric measurement from the AMSR on ADEOS-II and only the coincident forward look radar backscatter measurement from the SeaWinds scatterometer. The measurement geometry illustrated in Fig. 4 shows the multi-frequency brightness temperatures and fore-look V and H-pol sigma-0 measurements at the wind vector cell (WVC). In contrast to both the fore and aft multi-azimuth geometry that is required now for the wind scatterometers, a fore-look only design using combined active and passive instruments within a common antenna could provide a simplified and potentially lower cost instrument capable of retrieving wind speed and direction simultaneously with other oceanic and atmospheric parameters.

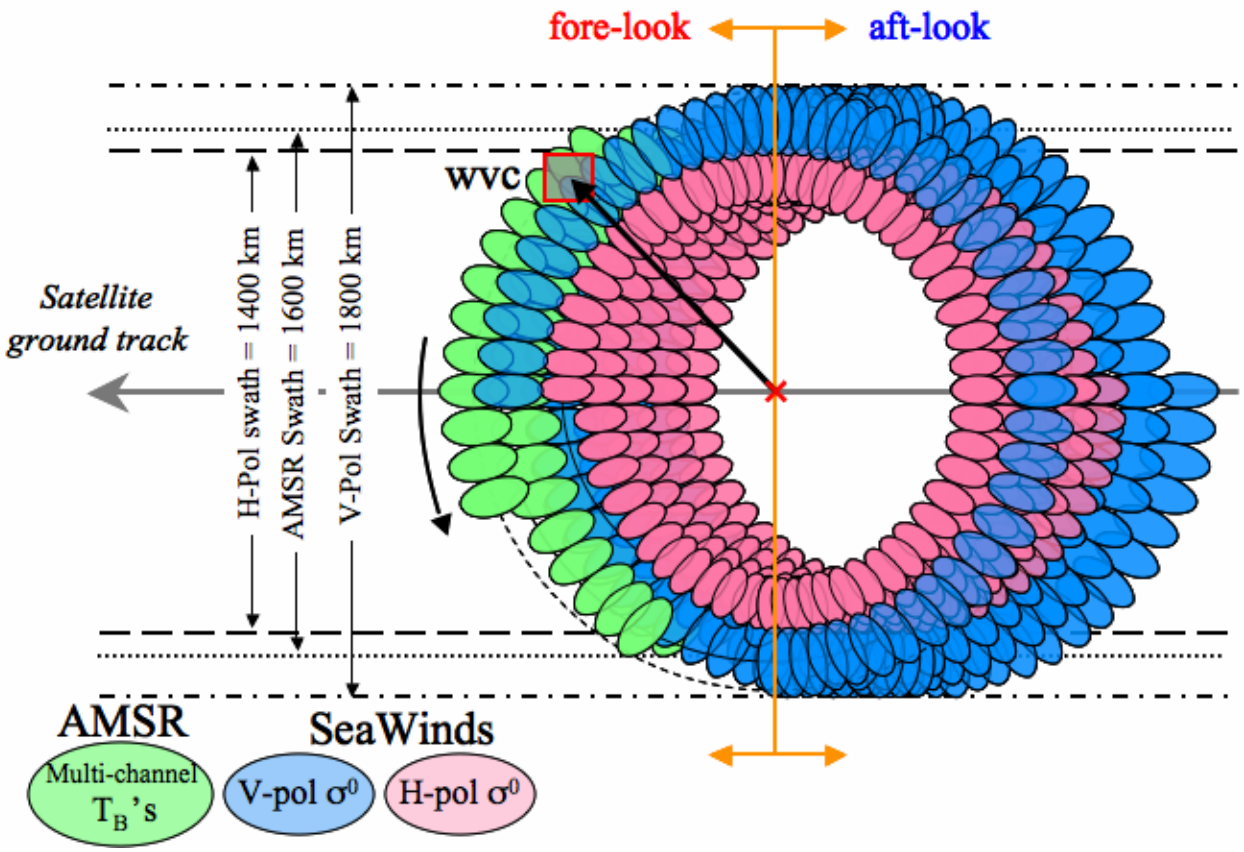

Figure 4: ADEOS-II Geometry.

The dissertation is organized as follows: •Chapter 2 provides a brief history and literature review of the ocean surface wind vector satellite missions and techniques. An introduction to active and passive microwave remote sensing is also presented in this chapter. •Chapter 3, which is the basis of this dissertation, discusses the dataset that was used in the development of the radiometric wind vector model function. This is followed by the derivation of the "*A*" parameter that causes the brightness temperature combination AT_{BV}-T_{BH} to be independent of the atmospheric parameters. The radiometric wind vector model function development is presented for AT_{BV}-T_{BH} to show that an empirical relationship does exist between the wind vector and the radiometric observation. Finally in this chapter the model function equations are presented and the corresponding coefficients are derived. •Chapter 4 presents the application of the passive model function with the fore-look SeaWinds' backscatter measurements to retrieve wind vector and to evaluate the potential of this novel wind vector retrieval technique. The results of a validation and performance analysis are presented. •Chapter 5 presents a summary, conclusions, and possible improvements for future works.

CHAPTER TWO: MICROWAVE REMOTE SENSING

The primary objective of this chapter is to provide an overview of microwave remote sensing over the ocean for vector wind retrieval. A historical background of the ocean wind vector measurement from space is presented. The principle concept of radiometry along with the basic operation of the radiometer is discussed. Geophysical parameter retrieval by a radiometer are possible using the principle of radiative transfer theory. The wind vector signal from a radiometer measurement that was investigated in the literature is also discussed. As shown in the section below, historically, the vector wind retrieval from space was primary achievable with scatterometry. The wind vector retrieval from a scatterometer, which is a particular type of radar, is possible by using a relationship between a wind vector and the normalized radar cross section (NRCS) known as the Geophysical Model Function (GMF). Basic radar principles are briefly discussed in the following section.

Brief History of Wind Measurement from Space

The ocean surface wind observation using a wind scatterometer was started with several airborne experiments during the late 1960's [6, 14]. The first experimental ocean wind vector measurement from space is dated back to the Skylab S-193 that flew in space from 1973 – 1974. In 1978, with the launch of Seasat, which operated for 99 days, the Seasat-A Satellite Scatterometer (SASS) demonstrated a proof of concept for ocean wind vector measurement from space [5, 6]. Since then, the wind vector measurement from a scatterometry has been well established. However, further scientific and engineering improvement was needed before becoming a routine wind measurement from space [6].

During the 1980's, there were several attempts in the U.S. to launch a satellite scatterometer, all of these programs failed because of lack of funding. On the other hand, the European Space Agency (ESA) successfully launched the first Earth Remote Sensing satellite (ERS-1) in 1991 that carried the Active Microwave Instrument (AMI) capable of wind vector retrieval [7]. This was followed by a duplicate instrument that flew on the second Earth Remote Sensing satellite (ERS-2) in 1995, the ERS-1 continue to operate until 2000 far exceeding its expected lifespan. The data from ERS-2 was available until 2003 when it was terminated due to the failure of an on-board tape drive.

In 1996, the first U.S. scatterometer since Seasat, the NASA Scatterometer (NSCAT) developed at the Jet Propulsion Laboratory, was carried on board Japan's first Advanced Earth Observing System (ADEOS) satellite, also known as Midori. ADEOS was developed by the National Space Development Agency (Japan) now called Japan Aerospace Exploration Agency (JAXA). Unfortunately NSCAT operated only for about one year (until the mid-1997) due to the failure of the spacecraft electrical power subsystem. A follow-on mission was planned on Japan's second ADEOS, however ADEOS-II was not launched until 2002. In the mean time, NASA and the Jet Propulsion Laboratory came up with a mission to fill the gap of wind vector observations between NSCAT and ADEOS-II with a new designed instrument on QuikSCAT. QuikSCAT carried only one instrument, a scatterometer called SeaWinds [15].

Since its launch in 1999, QuikSCAT continues to operate until the present day (2006). A duplicate SeaWinds instrument was launched on ADEOS-II in 2002. Unfortunately due to another spacecraft power system failure, ADEOS-II operated only during 2003. Therefore it only provided a limited data set of about six months. Thus, active microwave scatterometers, only, were used for ocean surface wind vector measurements for over three decades. In 2003, the

WindSat polarimetric microwave radiometer, built and developed by the U.S. Naval Research Laboratory (NRL), was launched on the Coriolis satellite to demonstrate wind vector measurement from space using a passive microwave instrument [8]. WindSat also served as a pathfinder for a future instrument, the Conical Scanning Microwave Imager/Sounder (CMIS) that was planed to be launched by the National Polar-orbiting Operational Environmental Satellite System (NPOESS) in 2010. Due to budgetary constraints, CMIS was cancelled this year (2006). Currently there is no wind sensor instrument planned to replace the cancelled CMIS.

The most recent scatterometer, the Advanced Scatterometer (ASCAT), was successfully launched on October 19, 2006 on the MetOp-A satellite. The ASCAT is the follow-on instrument to the one flown on the ERS-1 and ERS-2 satellites. The MetOp-A is the first satellite in a series of three satellites of the Meteorological Operational (MetOp) satellite programme managed by the EUMETSAT's Polar System (EPS), the joint space segment from ESA and the European Organisation for the Exploitation of Meteorological Satellites (EUMETSAT).

As part of the follow-on mission after the ADEOS series, JAXA is now planning two series of satellites called GCOM, with each series composed of three satellites. The first series iscalled GCOM-W with the first satellite scheduled to launch in 2009, and the first satellite in the second series called GCOM-C will be launched in 2010. The JAXA is now discussing the possibility of NASA supplying a similar SeaWinds scatterometer on the GCOM-W to be included with an AMSR instrument. Both sensors would be similar to those flown on ADEOS-II, and are the only two instruments to be carried on GCOM-W.

Radiometry

Radiometry is a field of science and engineering that relates non-coherent (noise) electromagnetic blackbody radiation measurements to geophysical information from the objects and media observed. All matter, at temperature above absolute zero; both absorb and emit non-coherent electromagnetic energy simultaneously. According to thermodynamic principals, absorption of incident electromagnetic energy by a medium is transformed into thermal energy, thus causing the physical temperature of the material to rise. To maintain thermal equilibrium, the energy then emitted by matter is in proportion to its physical temperature.

An ideal material that is a perfect absorber is called a blackbody. The object absorbs all the incident energy with zero reflection. Since the blackbody is a perfect absorber, it is a perfect emitter as well. According to Planck's radiation law, the blackbody radiates energy uniformly in all directions with spectral power density (flux) per unit area per unit frequency given by

$$S_f = \frac{2\pi h f^3}{c^2}\left(\frac{1}{e^{hf/kT}-1}\right), \text{ W/m}^2\text{/Hz} \tag{2.1}$$

where h = Planck's constant = 6.63×10^{-34} joules

k = Boltzmann's constant = 1.38×10^{-23} joules/K

c = speed of light = 3×10^8 m/s

T = absolute temperature, K

f = radiation frequency, Hz

[2] and illustrated in Fig. 5.

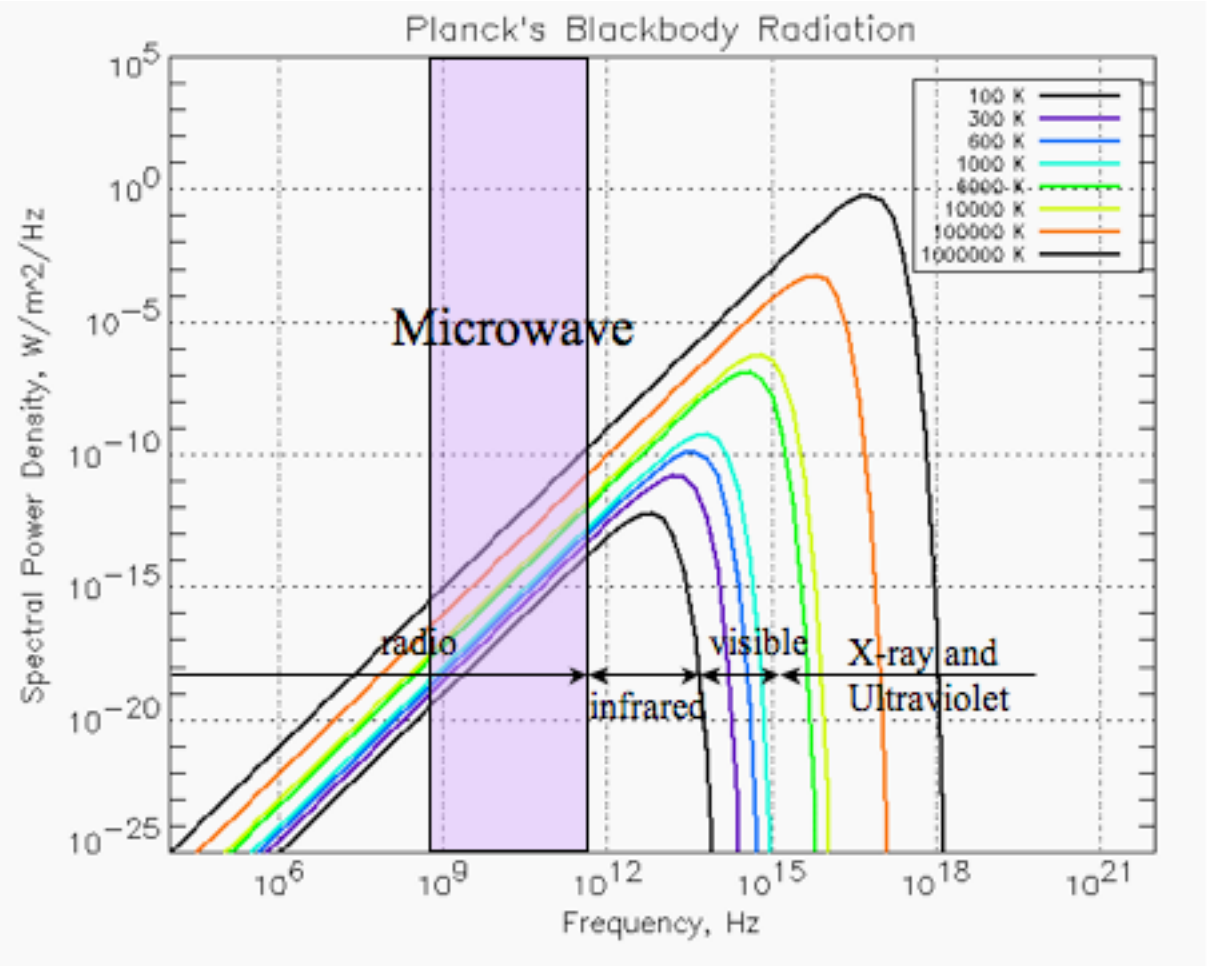

Figure 5: Plank's blackbody radiation law.

Over the lower frequency range in the microwave region, according to the Rayleigh-Jeans law, the spectral density from (2.1) may be presented in a reduce form using the approximation that $hf << kT$ given by

$$S_f = \frac{2\pi f^2 kT}{c^2} = \frac{2\pi kT}{\lambda^2} \tag{2.2}$$

[2] and illustrated in Fig. 6.

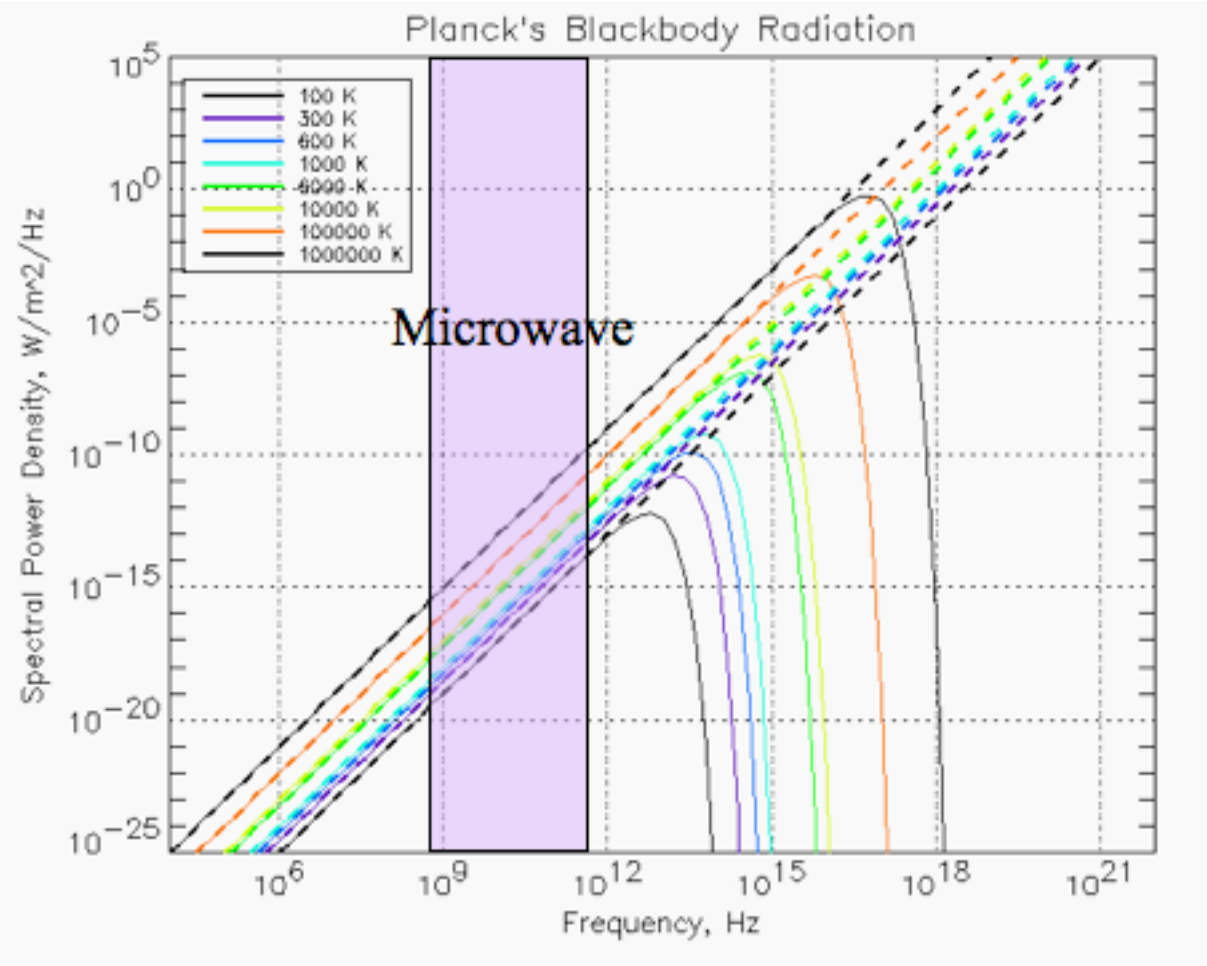

Figure 6: Rayleigh-Jeans Approximation.

Consider an isotropic transmitting antenna. The flux density radiated in free space to distance R is given by [2, 16]

$$S = \frac{P_t}{4\pi R^2}, \text{ W/m}^2 \tag{2.3}$$

The power at the receiving antenna according to the Friss transmission formula is [2, 16]

$$P_r = SA_{eff} = \frac{P_t}{4\pi R^2} A_{eff} \tag{2.4}$$

where P_t = transmitted power, W

P_r = received power, W

A_{eff} = effective capture area of the receiving antenna, m^2

The effective area of the receiving antenna A_{eff} may be related to the solid angle of the antenna pattern by [2, 16]

$$A_{eff} = \frac{\lambda^2}{\Omega_p} \tag{2.5}$$

The solid angle of the receiving antenna pattern is defined in terms of the normalized radiation pattern $F_n(\theta,\phi)$ given by [2, 16]

$$\Omega_p = \iint_{4\pi} F_n(\theta,\phi)d\Omega \tag{2.6}$$

When considering that the receiving antenna illuminated an instantaneous field of view (IFOV) over the target with an area A_t, the solid angle subtended from the receiving antenna at distance R to the target may be related by [2, 16]

$$\Omega_p = \frac{A_t}{R^2} \tag{2.7}$$

This relationship of the IFOV with the solid angle is illustrated in Fig 7. Now by substituting (2.7) into (2.5), the relationship between effective area of the receiving antenna and the IFOV over the target is derived as [2, 16]

$$A_{eff} = \frac{\lambda^2 R^2}{A_t} \tag{2.8}$$

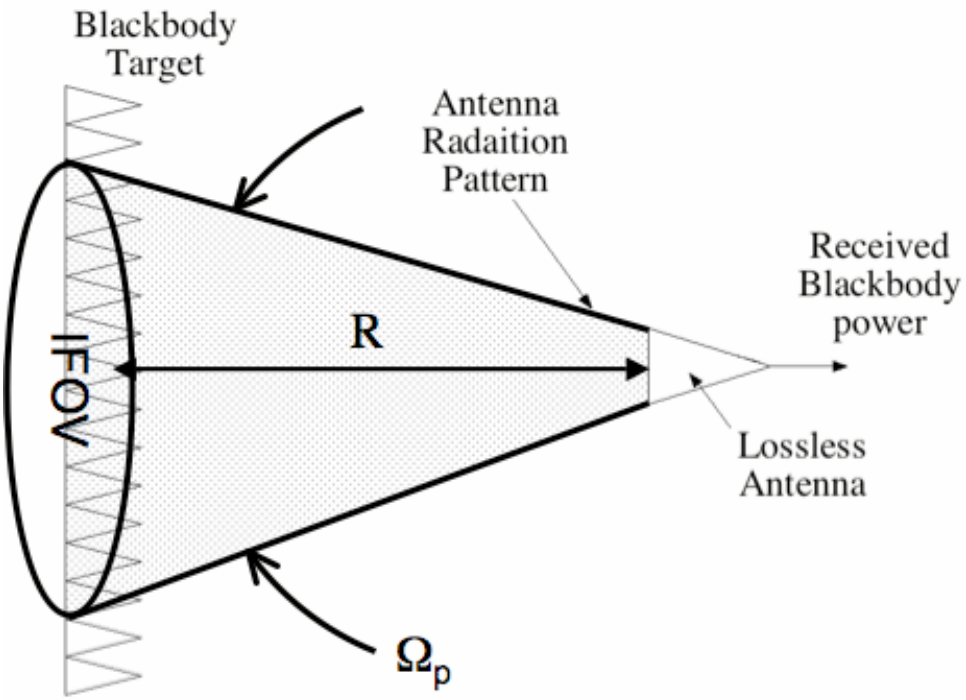

Figure 7: Antenna IFOV.

As discussed earlier, radiometry involves the measurement of the self-emitted noise-like electromagnetic radiation from an object. A radiometer is a passive system, which means there is no transmission source other than the blackbody self-emission (unlike a radar or communication system). The matter emits radiometric energy according to Planck's blackbody radiation law and, in the microwave region, the emitted power, in the sense of transmitted power P_t given in the Friss transmission formula, may be written in terms of the flux density over the area A_t as given by [2, 16]

$$P_t = SA_t = \frac{2\pi kT}{\lambda^2} A_t \tag{2.9}$$

From the Friss transmission formula given in (2.4), the received power at the antenna yield after substitute (2.8) and (2.9) into (2.4) simplifies to a form in terms of the blackbody absolute temperature T to be [2]

$$P_r = \frac{2\pi kTA_t}{\lambda^2}\frac{2}{4\pi R^2}\frac{\lambda^2 R^2}{A_t} = kT \text{, W/Hz} \tag{2.10}$$

Note that the factor of 2 in the middle term of (2.10) is accounted for by semi-isotropic radiation from the target to the antenna (hemispherical radiation pattern). The received power from (2.10) is a power per unit Hertz. Thus the power received by a radiometer over a bandwidth B becomes [2]

$$P_r = kTB \tag{2.11}$$

Equation (2.11) provides a linear relationship of the received power with the media absolute physical temperature. This simple relationship allows the interchangeability of the power received and the blackbody temperature given a known bandwidth. The blackbody physical temperature T is referred to as the radiometric temperature. A similar result found by Nyquist for the noise power available at a resistive termination of a transmission line with a physical temperature T [2].

For a non-blackbody material, referred to as a "graybody", the power density with respect to a blackbody is defined as the emissivity given as [2]

$$e = \frac{S_{non-blackbody}}{S_{blackbody}} \tag{2.12}$$

A blackbody equivalent radiometric temperature is defined as a brightness temperature in term of the material physical temperature given by [2]

$$T_B = eT_{phy} \tag{2.13}$$

Consider a scenario in Fig. 8 where a radiometer views the Earth's surface from space over the ocean. From the theory of radiative transfer, the total radiometric temperature collected by the antenna comprises several components of the brightness temperatures along the path of propagation. A simple form of the apparent brightness temperature at the antenna maybe expressed as [2]

$$T_{AP} = T_{BU} + \tau\left(T_{refl} + T_B\right) \tag{2.14}$$

where T_B = brightness temperature from the ocean surface = $e\ T_S$

T_S = sea surface temperature (SST)

$T_{refl} = r\ \mathrm{T_{Sky}} = (1\text{-}e)\ \mathrm{T_{Sky}}$

$T_{Sky} = T_{BD} + \tau\, T_C$

T_C = cosmic radiation = 2.7 K

r = ocean surface power reflection coefficient

τ = atmospheric transmissivity

T_{BU} = up-welling atmospheric radiation

T_{BD} = down-welling atmospheric radiation

When combining all of the components together, (2.14) becomes [2, 17]

$$T_{AP} = T_{BU} + \tau \cdot r \cdot (T_{BD} + \tau \cdot T_C) + \tau \cdot e \cdot T_S \tag{2.15}$$

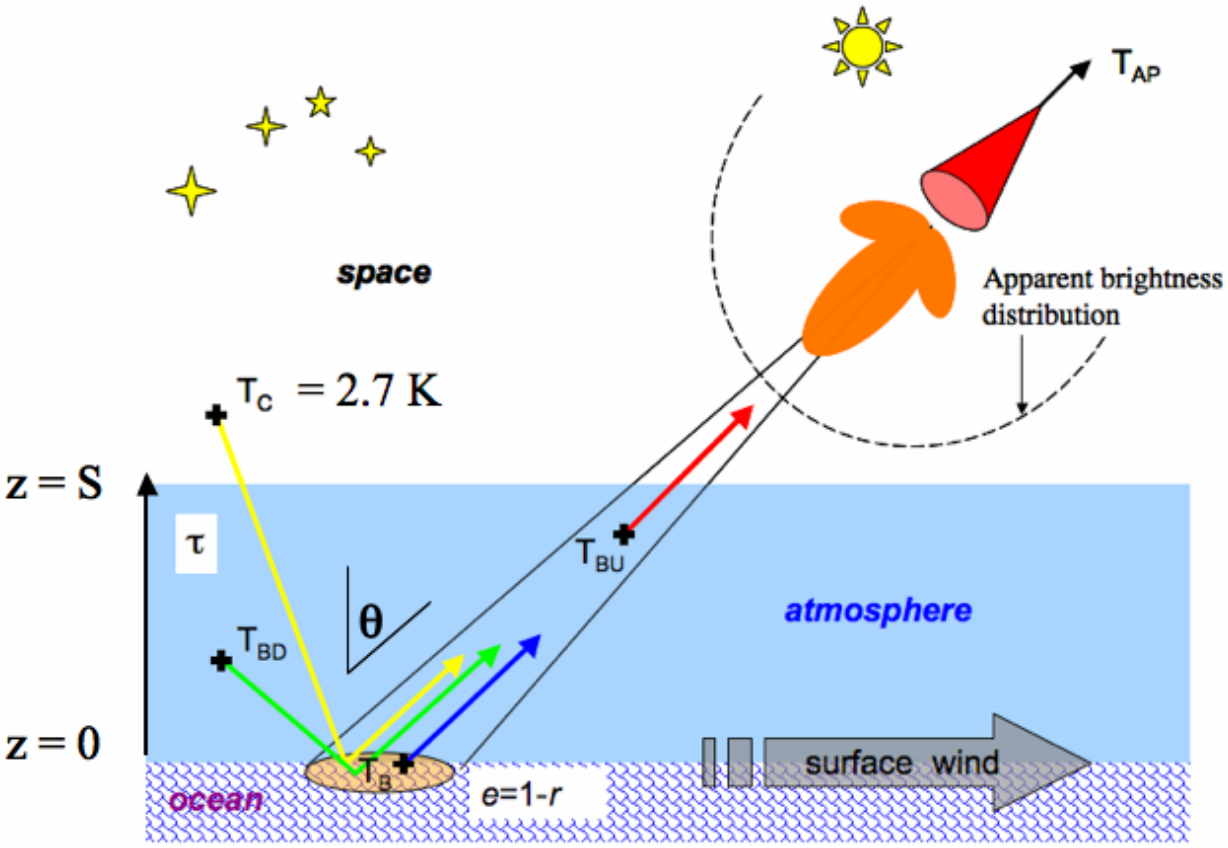

Figure 8: Radiative transfer process scenario.

The ocean grey-body emission is strongly polarized and depends upon the dielectric properties of the seawater. For the air/sea boundary, the voltage (electric field) reflection coefficient for a given polarization is determined by [2]

$$\rho_V = -\left(\frac{\varepsilon_r \cos\theta - \sqrt{\varepsilon_r - \sin^2\theta}}{\varepsilon_r \cos\theta + \sqrt{\varepsilon_r - \sin^2\theta}}\right)$$
$$\rho_H = -\left(\frac{\cos\theta - \sqrt{\varepsilon_r - \sin^2\theta}}{\cos\theta + \sqrt{\varepsilon_r - \sin^2\theta}}\right) \tag{2.16}$$

where ε_r = relative complex dielectric constant of seawater

θ = incidence angle

ρ_V and ρ_H = Fresnel voltage reflection coefficient for vertical and horizontal polarization respectively

and the emissivity is related to the voltage reflection coefficient as [2]

$$e = 1 - r = 1 - |\rho|^2 \tag{2.17}$$

where r = reflectivity or power reflection coefficient

The dielectric constant of the seawater is a function of salinity (salt content), sea temperature and surface roughness (wind speed). Thus the reflectivity r is a function of those parameters as well as the incidence angle and polarization of the electric field. In addition, when the sea becomes rough due to wind speed and the sea foam present, the changes in reflectivity or emissivity causes the brightness temperature to increase. This sensitivity of the ocean brightness temperature to surface winds enables the wind speed retrieval from a radiometer.

For the atmosphere, the up-welling and down-welling brightness temperature is determined by the atmospheric absorption. Unlike the ocean, the atmospheric emission is

isotropic and non-polarized. The upwelling and downwelling may be calculated as a function of the atmospheric physical temperature and the atmospheric absorption given as [2, 17]

$$T_{BU} = \int_0^{\infty} \alpha(z)T(z)\tau(z,S)dz$$
$$T_{BD} = \int_0^{\infty} \alpha(z)T(z)\tau(0,z)dz \tag{2.18}$$

where $T(z)$ = physical temperature of the atmosphere

α = atmospheric absorption

τ = atmospheric transmissivity

z = altitude and S = altitude at the top of the atmosphere

The atmospheric transmissivity is proportion to the absorption between the altitude z_1 and z_2 given by [2, 17]

$$\tau(z_1,z_2) = \exp\left(-\int_{z_1}^{z_2} \alpha(z)dz\right) \tag{2.19}$$

In the atmosphere, there is resonant absorption for oxygen at 60 and 120 GHz. Resonant absorption for water vapor occurs at 21, 183, and 325 GHz [2]. Also there is non-resonant absorption by cloud liquid water and rain.

Scatterometry

A scatterometer is a radar instrument specifically designed to measure the vector wind over the ocean. The wind vector retrieval from a scatterometer is achieved by the well-know relationship between wind vectors and the normalized radar cross-section (NRSC) or sigma-0 (σ^0) [18 – 20]. The sigma-0 is measured using the radar equation and the received power at the

receiver, which is similar to the radiometer infer the brightness temperature from the received power. From the Friss transmission formula, applied to a monostatic radar, the received (backscattered) power is given by [2, 3, 16]

$$P_r = \frac{P_t G_t}{4\pi R^2} \frac{\sigma}{4\pi R^2} A_{eff} \tag{2.20}$$

Since the radar is an active instrument, the transmitter provides source of radiation as shown in Fig. 9. Here the G_t is the transmitting antenna gain, and the ($1/4\pi R^2$) term accounts for the one-way free space spreading loss of propagation to the target with the radar cross section given by σ. Usually the transmitting and receiving antenna for radar system is the same thus the antenna gains are the same and be may related to the effective are A_{eff} by [2, 3, 16]

$$G = G_t = G_r = \frac{4\pi A_{eff}}{\lambda^2} \tag{2.21}$$

Substituting (2.21), in terms of A_{eff}, into (2.20) yields the monostatic radar equation for a point target [2, 3, 16]

$$P_r = \frac{P_t G^2 \lambda^2}{(4\pi)^3 R^4} \sigma \tag{2.22}$$

Since all the radar parameters are known and range R is also known from the geometry of the satellite orbit, the radar cross section can be derived from (2.22).

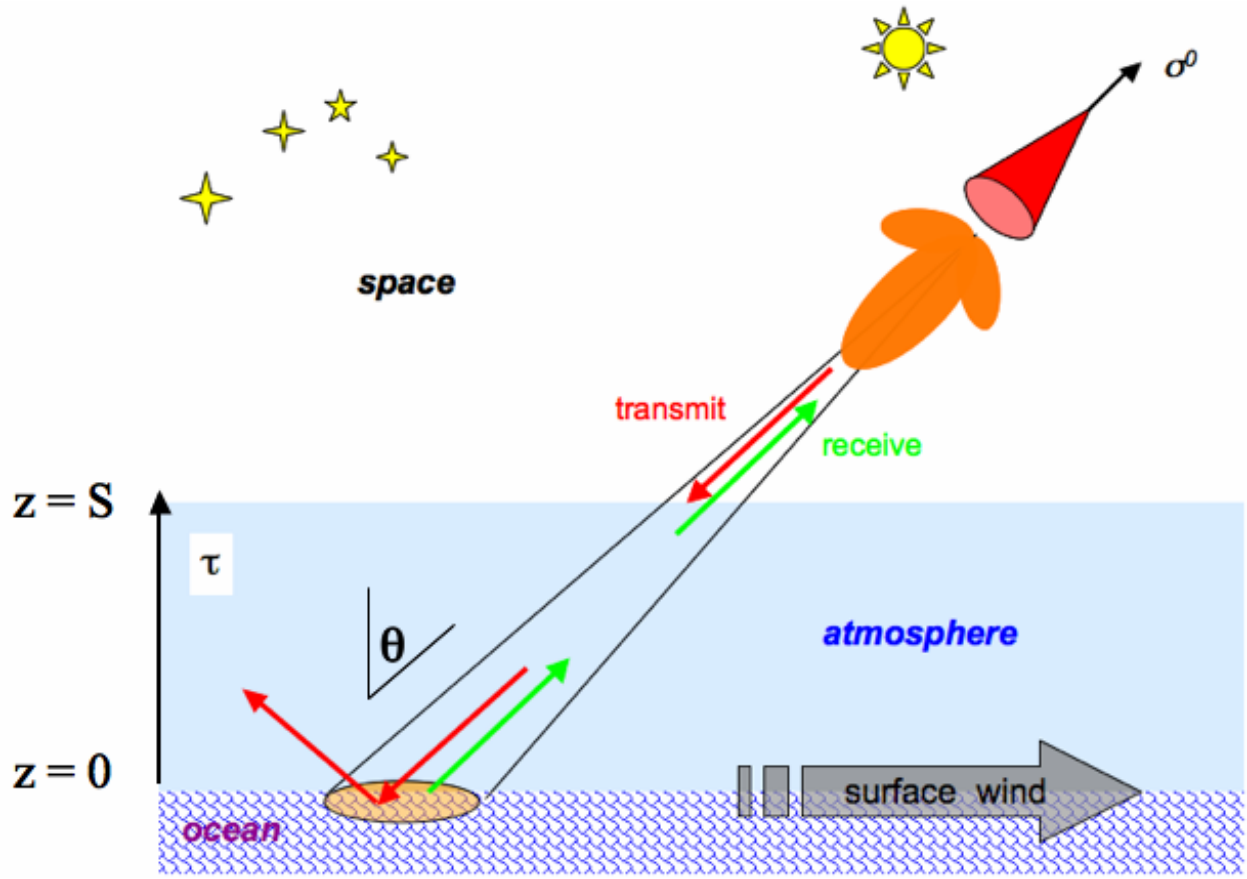

Figure 9: Radar measurement scenario.

Based upon empirical observations, the relationship between the normalized radar cross-section and wind vector is normally modeled in the form of two harmonic cosine functions given by [20]

$$\sigma^0 = C_0(wspd) + C_1(wspd)\cos(\phi) + C_2(wspd)\cos(2\phi) \tag{2.23}$$

where ϕ = wind direction relative to the radar azimuth direction

wspd = wind speed, m/s

The coefficients C_0, C_1 and C_2 are determined empirically using observed sigma-0's with known surface wind vector conditions. This results in the well-know relationship between σ^0 and wind vector known as the Geophysical Model Function (GMF) given as [18 – 20].

$$\sigma^0 = GMF(\phi, wspd, p, \theta) \tag{2.24}$$

Here the σ^0 is also a function of radar polarization (p), and θ, the incidence angle. An example of the SeaWinds scatterometer GMF (with the mean C_0 removed) is shown in Fig. 10 – 11 for vertical and horizontal with two different incidence angles.

The resulting anisotropic signal with relative wind direction is strong, however, the biharmonic nature of the GMF causes the wind direction retrieval to produce multiple solutions. The ambiguous wind vectors problem is resolved by using simultaneously measurements from multiple azimuth angles, and the retrieval algorithm is based on the maximum likelihood estimation (MLE) [21].

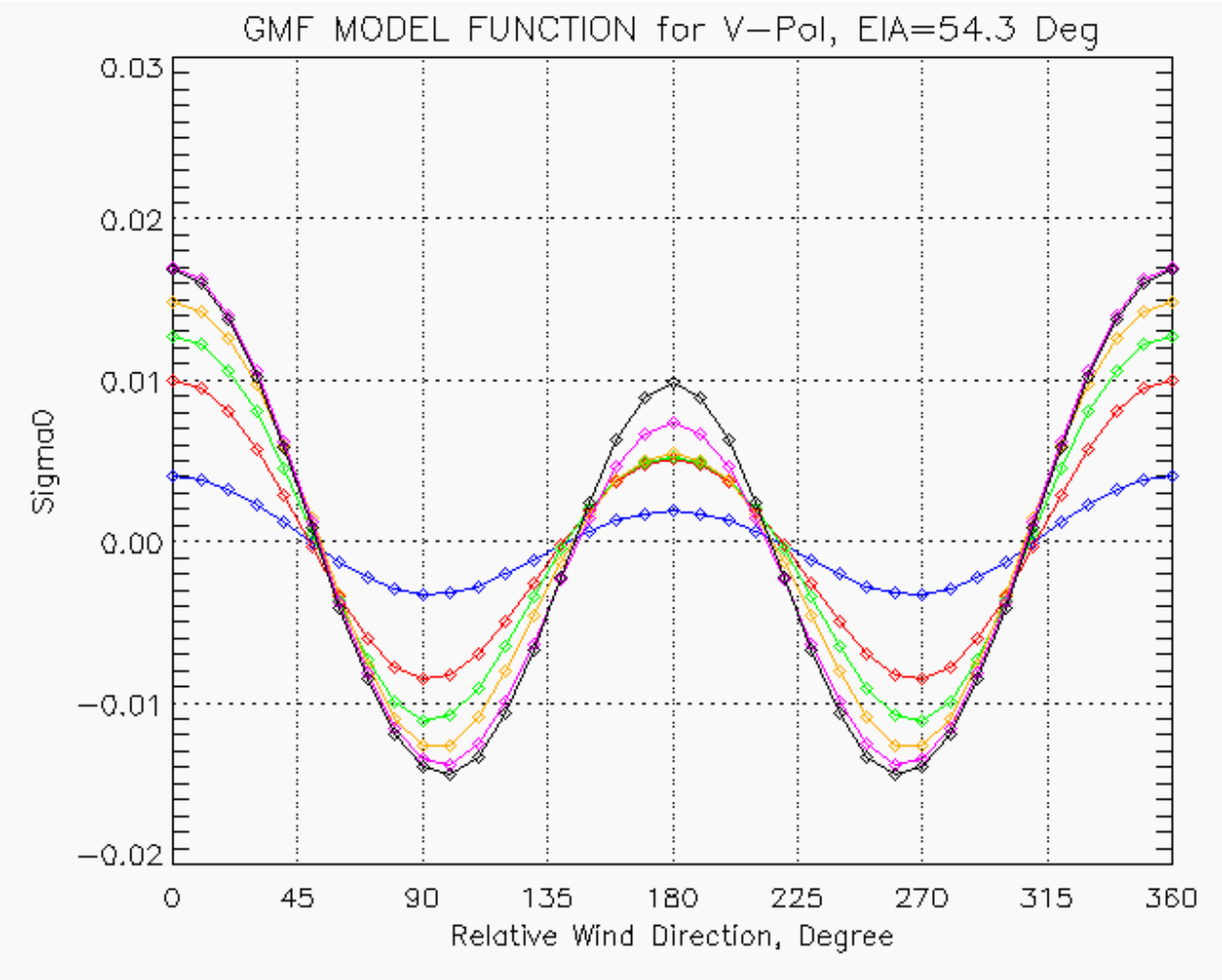

Figure 10: SeaWinds' GMF for V-pol (with C_0 term removed).

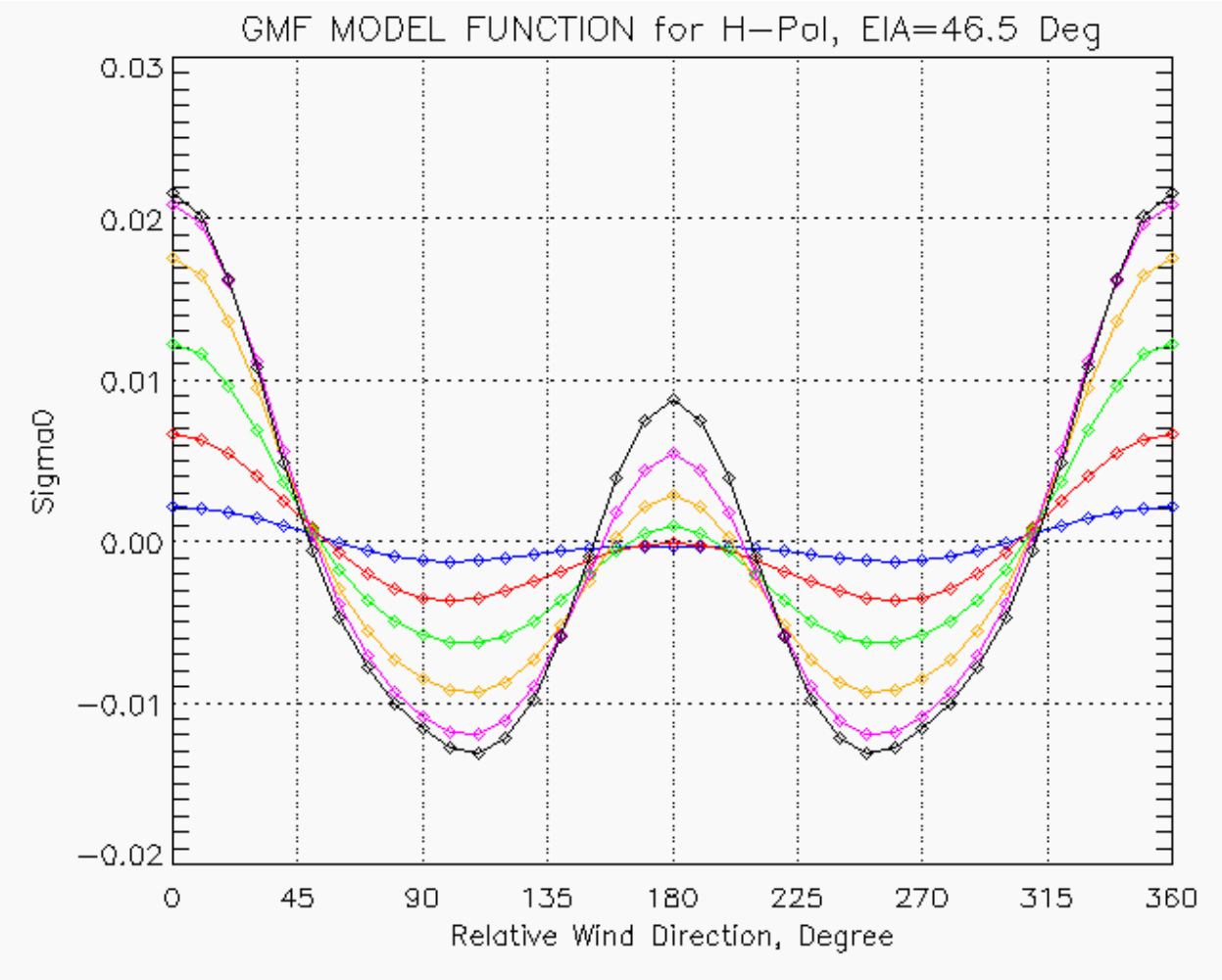

Figure 11: SeaWinds' GMF for H-pol (with C_0 term removed).

CHAPTER THREE: EMPIRICAL MODEL FUNCTION

This chapter describes a wind vector model function development for the AMSR radiometer that is the basis of the dissertation. The chapter begins with the description of the data used to train the model function, their binning scheme, and how the data were matched-up with different environmental data sources. The following section explains the relationship between the AMSR brightness temperatures and surface wind vectors. A passive wind direction signal has been discovered by Wentz [10] for vertical and horizontal polarization with the signal amplitude being between 2.0 – 3.5 K peak-to-peak for moderate wind speeds. In this dissertation, we are interested in the combination of the two T_B polarizations via a parameter simply called "*A*", which is predominantly a function of ocean surface parameters and causes the atmospheric brightness temperature components to cancel.

This brightness temperature combination was previously described by Meissner and Wentz [11], who showed that the combination of $2T_{BV}$-T_{BH} for 37 GHz was largely independent of the atmospheric water vapor and cloud liquid water. We extend their work and show that the brightness temperature combination maybe expressed as AT_{BV}-T_{BH}, where T_{BV} and T_{BH} here are the AMSR brightness temperatures of the vertical and horizontal polarization respectively. Further, this combination of AT_{BV}-T_{BH} has been investigated by Jelenak [12] for the WindSat radiometer brightness temperatures, where *A* is a constant dependent on the microwave frequency used. The AT_{BV}-T_{BH} for AMSR was also shown previously to be a constant *A* value, which varied with the radiometer frequency [22].

In this dissertation, the *A* is simultaneously calculated for each of the individual measurements. The derivation of the *A* parameter is explained below, and it is shown that this

would almost cancel the atmospheric dependence. Finally a passive model function showing the relationship between the AT_{BV}-T_{BH} and surface wind vectors was derived using a non-linear regression and the model function coefficients were determined.

Data Match-up and Binning

It is always important to use the best available data to train a model function. For the available instruments carried on the ADEOS-II satellite, the AMSR provides the source of the brightness temperature data, and the SeaWinds provides the quality source of the collocated wind speed and wind direction. These are the data sources from which the model function is developed to determine the relationship between the two quantities.

The AMSR brightness temperatures and retrieved geophysical products between April 10 and October 24, 2003 are available to the SeaWinds' science community. The AMSR overlay level 2A product used in this study contains 12 channels dual polarization brightness temperatures along with retrieved atmospheric and ocean surface parameters including, water vapor, cloud liquid water, sea surface temperature and sea surface wind speed. The list of complete parameters stored in the AMSR overlay product can be found in Appendix A. These data were formatted into wind vector cell (WVC) quadrants corresponding with the SeaWinds wind vector format of the L2B product that to be explained below. The V and H brightness temperature for 10.7, 18.7 and 36.5 GHz were used from AMSR L2A data product.

The corresponding SeaWinds science data L2A and L2B product contain ocean surface backscatter (sigma-0 or σ^0) and the retrieved wind vector respectively. In the SeaWinds product L2A, the data were recorded for each of the sigma-0 sample and their associated radar

parameters along the scan. For each SeaWinds antenna scan, this corresponds to one row of the data record, and for each orbital revolution (rev), it corresponds to 1624 rows of data records. In the product L2B, the data were gridded parallel to the measurement swath into approximately 25 km x 25 km “boxes” called the wind vector cells (WVC) containing wind vector solutions with their associated parameters. For each scan or row, it forms 76 WVCs across-track and for each rev, it forms 1624 rows along-track. The 76 x 1624 data array is stored for each rev. This structure of data is similar to that of the AMSR overlay product, except for each WVCs; it was further subdivided into quadrants. Thus, the data format for the AMSR is 4 x 76 x 1624 array; however, for SeaWinds L2A product, the data format was slightly different since it contains all of the measurement samples. The L2A data contains the same number of rows of 1624 along-track, but the number of across-track samples depends on several parameters. Provided row and WVC position (simply called “cell”) for each measurement samples, the data in the product L2A could be easily mapped to the corresponding parameters in the product L2B and AMSR overlay. Complete lists of the parameters contain in the L2A and L2B may be found in Appendix A.

For each satellite revolutions, there are a total of three files corresponding to AMSR overlay, L2A, and L2B. Since both instruments are on the same satellite, this forms a one-to-one matching between each product, and all parameters collected by both AMSR and SeaWinds are automatically spatially and temporally collocated. The only work that needs to be done is to put the different data parameters and format together into a common structure for simplicity of data processing.

The only external data source that needed to be match-up with AMSR and SeaWinds was the sea surface temperature (SST) product. Although the SST was also retrieved from AMSR, the current version of the SST retrievals has questionable accuracy. The SST from the National

Centers for Environmental Prediction's (NCEP) Global Data Assimilation System (GDAS) was the choice of the external SST source. The GDAS is a global map model of the Earth's atmosphere and ocean surface generated every 6 hours for 00Z, 06Z, 12Z and 18Z daily [23]. GDAS produces one file that corresponds to one six-hour-GDAS map; therefore, to cover one full day, a total number of four files are required. The system assimilates a variety of measurements collected from buoys, ships, planes, radiosondes, weather radars, and satellites. The current NOAA/NESDIS version of GDAS used provides a 1° x 1° global latitude/longitude grid resolution for a limited selection of parameters significant for a satellite geophysical retrievals validation [23]. Not only the SST information is available, but also the other ocean surface parameters including surface wind speeds and directions as well as other atmospheric profiles. More detail of the GDAS available parameters may be found in Appendix A.

For each rev of AMSR data, there must be corresponding GDAS parameters for each of the WVC quadrants. The collocation process between AMSR and GDAS was accomplished by first locating the GDAS files within ±3.0 hrs of AMSR rev duration time [23]. There could have been more than one GDAS file that corresponding to AMSR rev if that rev happened to exist between two consecutive GDAS days. Once the proper AMSR and GDAS files were read, for each of AMSR's WVC quadrant latitude/longitude, the closest four surrounding GDAS points were spatially interpolate to that WVC location [23] as illustrated in Fig. 12. After finding all of the WVC GDAS match-ups, a file was saved using the same data format as the AMSR's 4 x 76 x 1624 array structure.

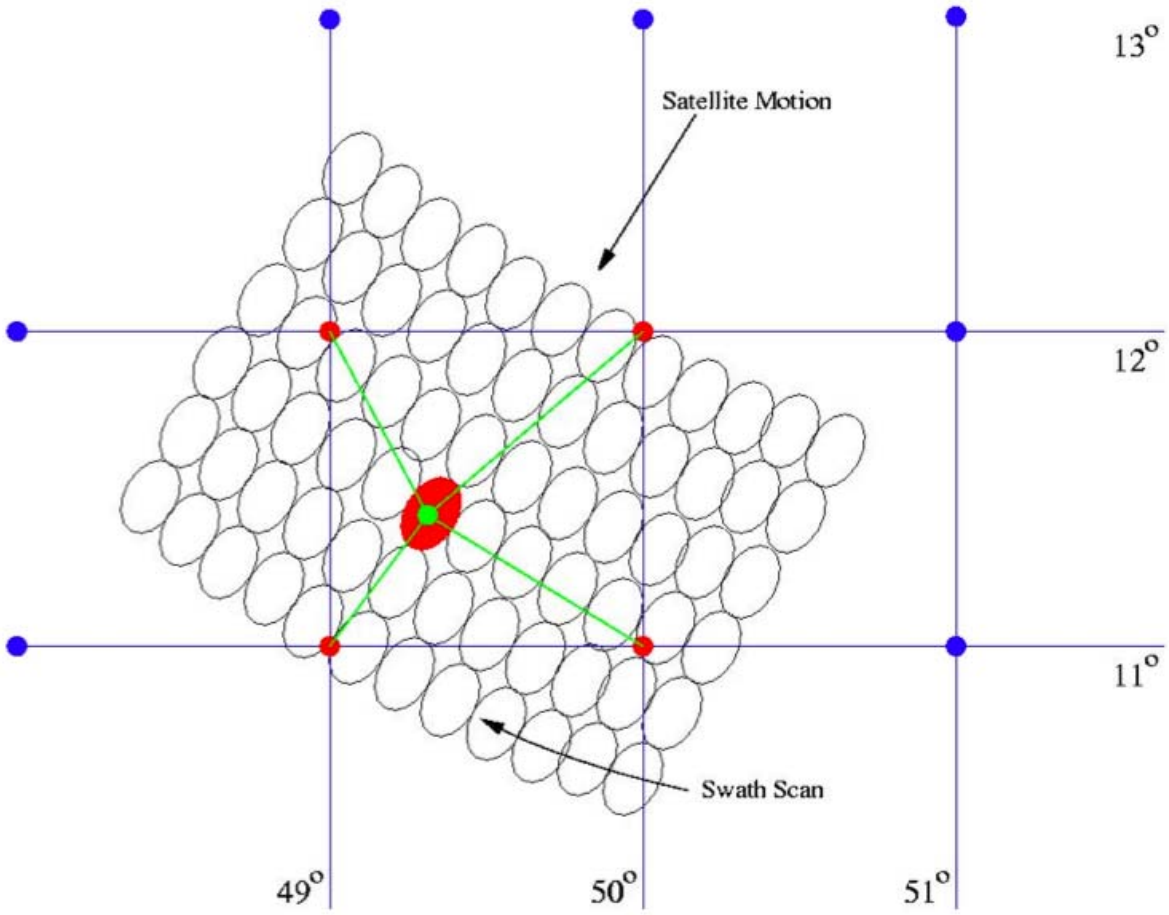

Figure 12: GDAS/Satellite match-up scheme (Courtesy of L. N. Connor) [23].

Now there are four data files: AMSR overlay, L2A, L2B and GDAS data that correspond to one orbital revolution of the satellite. As discussed previously, each of the data products have slightly different formats except for the GDAS that was made to be the same as of the AMSR overlay. It would be convenient to combine every data parameters from each of the products into a common array structure for data processing purposes. However, this would make the data structure to be too large to be implemented efficiently. Since only a subset of the parameters contain in each of the products were needed, only the parameters that were required and/or may

be useful for later use were kept in the structure, and to simplify the data format, the 76 x 1624 WVC arrays were used. The L2B data was already stored in a 76 x 1624 array thus no modification was required. In the L2A, there are “row number” and “cell” parameter that can be used to relate other parameters into a WVC, and then it can be indirectly converted into 76 x 1624 array using those parameters. For the AMSR overlay and GDAS data, the parameters in each of the WVC quadrants were simply averaged in to a single WVC to form the 76 x 1624 arrays. One of the most important required parameters was the azimuth angle of the AMSR measurement, and unfortunately, this was not provided in the AMSR overlay product. However, using the typical AMSR scan radius and WVC location, the corresponding azimuth angle can be calculated [24]. Except for small errors in spacecraft attitude, the AMSR azimuth consistently repeated for every orbit as a simple function of latitude. The algorithm and the IDL routine for AMSR azimuth calculation were given in Appendix B. When all of the selected parameters were assembled, they were stored in one collection of 76 X 1624 array structure, and these parameters may be found in Table 1.

Table 1 Match-up dataset.

Variable Name	Size	Description
LON	Float	WVC longitude
LAT	Float	WVC latitude
GDAS_SST	Float	GDAS sea surface temperature
GDAS_TPW	Float	GDAS total precipitable water
GDAS_WSPD	Float	GDAS wind speed
GDAS_WDIR	Float	GDAS wind direction
SWS_WSPD	Float	SeaWinds retrieved wind speed (selected)
SWS_WDIR	Float	SeaWinds retrieved wind direction (selected)
AMSR_WSPD	Float	AMSR retrieved wind speed
AMSR_LIQUID	Float	AMSR retrieved cloud liquid water
AMSR_WATER_VAPOR	Float	AMSR retrieved water vapor
AMSR_SST	Float	AMSR retrieved sea surface temperature
AMSR_AZIMUTH*	Float	AMSR scanning azimuth
FLAG	Float	Quality Control Flags
TBS	Float Array [6]	AMSR Brightness Temperature for 10V, 10H, 18V, 18H, 37V, 37H
SIGMA0V1	Float Array [6]	Fore V sigma-0 and related parameters (EIA, K_p's, azimuth)
SIGMA0H1	Float Array [6]	Fore H sigma-0 and related parameters
SIGMA0V2	Float Array [6]	Aft V sigma-0 and related parameters
SIGMA0H2	Float Array [6]	Aft H sigma-0 and related parameters

* AMSR azimuth was approximately calculated. The IDL routine may be found in Appendix B [24].

The data were separated into two independent datasets: one for training and another "withheld" for testing. Every three consecutive revs were used for a training set and every fourth was skipped and saved in a testing set, and all the orbits between April 10 and October 24, 2003 were used. The data were then prepared for model development by first sorting the training dataset with respect to wind speed. The retrieved wind speeds from SeaWinds L2B were used as the "surface truth" to sort the AMSR data in 1.0 m/s bins. Since all of the parameters were stored in the same structure, it conveniently provided corresponding parameters in each of the wind speed bin. Next the data were further subdivided into 2.0 degree Celsius SST bins based on the GDAS SST. Finally, the data were subdivided into ± 5.0° relative wind direction bins using the wind direction solution from the SeaWinds L2B and the AMSR azimuth angle. The data-binning scheme is illustrated in Fig. 13, and a similar binning scheme was repeated for the testing dataset.

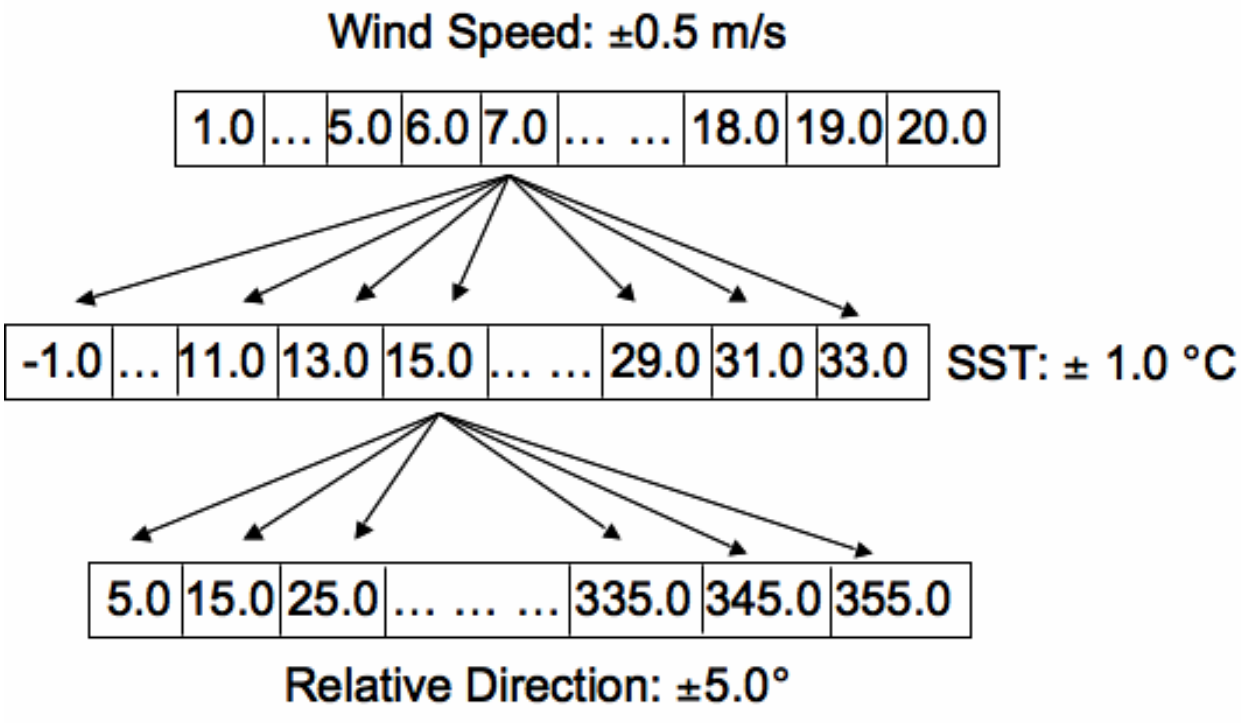

Figure 13: Dataset binning scheme.

***A*V-H**

Microwave radiometer antennas collect the naturally occurring microwave emission from the Earth's surface and its overlaying atmosphere. Both the oceanic and atmospheric physical parameters contribute to the total apparent brightness temperatures measured at the top of the atmosphere by a microwave radiometer. For higher microwave frequencies, the dominant brightness temperature signal contribution comes from the atmosphere. On the other hand, for lower microwave frequencies, the surface signal becomes strong enough to provide for wind speed retrievals using the vertical (V) or horizontal (H) polarization microwave observation; however, the wind direction signal is still very weak. Knowledge of the atmospheric brightness contributions are critical if the single polarization is to be used for full wind vector retrieval because a small error in the atmospheric corrections will lead to a significant error in the wind direction retrieval.

However, with the linear combination of the V and H brightness temperatures, the atmospheric correction may not be required. This linear combination was previously found to be mostly independent of the atmospheric parameters and is predominantly a function of the sea surface wind speed, wind direction and sea surface temperature (SST) [11, 12]. The brightness temperature combination may be expressed as $A\mathrm{T_{BV}}$-$\mathrm{T_{BH}}$ or simply *A*V-H, where *A* is a constant value dependent on microwave frequency used [12] and will be discussed in more detail below.

From the radiative transfer theory, the total apparent brightness temperature collected at the radiometer antenna may be expressed as [11]

$$T_B = T_{BU} + \tau \cdot eT_S + \tau \cdot r(1+\Omega)(T_{BD} + \tau \cdot T_C) \tag{3.1}$$

The T_{BU} and T_{BD} are upwelling and downwelling atmospheric brightness temperature respectively and are given by (3.2) [2, 11].

$$T_{BU} = \int_0^{\infty} \alpha(z)T(z)\tau(z,S)dz$$
$$T_{BD} = \int_0^{\infty} \alpha(z)T(z)\tau(0,z)dz \tag{3.2}$$

The $\alpha(z)$ and $T(z)$ are the atmospheric absorption and physical temperature profile at altitude z respectively. The atmospheric transmittance between two vertical points are defined in term of $\alpha(z)$ as [2, 11]

$$\tau(z_1,z_2) = \exp\left(-\int_{z_1}^{z_2} \alpha(z)dz\right) \tag{3.3}$$

The τ in (3.1), defined as $\tau(0,S)$ from (3.3), is the total atmospheric transmittance between the sea level and the top of the atmosphere, $z = S$ [11]. The emissivity e and reflectivity r in (3.1) are related by Kirchhoff's Law as $r = 1 - e$. The Ω is the relative diffuse surface scattering factor due to the wind roughen surface. The T_C is the cosmic brightness temperature equals to 2.7 K and the T_S is the sea surface temperature (SST) in degree Kelvin.

If the atmosphere is modeled as an equivalent single homogeneous layer, then the average atmospheric absorption $\alpha(z)$ is assumed to be a constant α and, likewise, the average of the atmospheric profile $T(z)$ is assumed to be a constant T, the integral in (3.2) reduces to [11]

$$T_{BU} = T_{BD} = \int_0^S \alpha \cdot T \cdot e^{-\alpha \cdot z} dz = (1 - e^{-\alpha \cdot S})T = (1 - \tau)T \tag{3.4}$$

The atmosphere may be parameterized in terms of upwelling and downwelling effective air temperatures as [25]

$$T_U = \frac{T_{BU}}{(1-\tau)} \tag{3.4a}$$

$$T_D = \frac{T_{BD}}{(1-\tau)} \tag{3.4b}$$

These effective temperatures are an indicative of the air temperature averaged over the lower to mid troposphere and are very similar in value given that the absence of significant rain [25]. This defined an atmospheric effective temperature $T_{eff} \equiv T_U \approx T_D$. To show the similarity of these effective temperatures using the above approximation, the differences between downwelling and upwelling effective temperature are plotted as a function of water vapor and frequency as given in Fig. 14 [26].

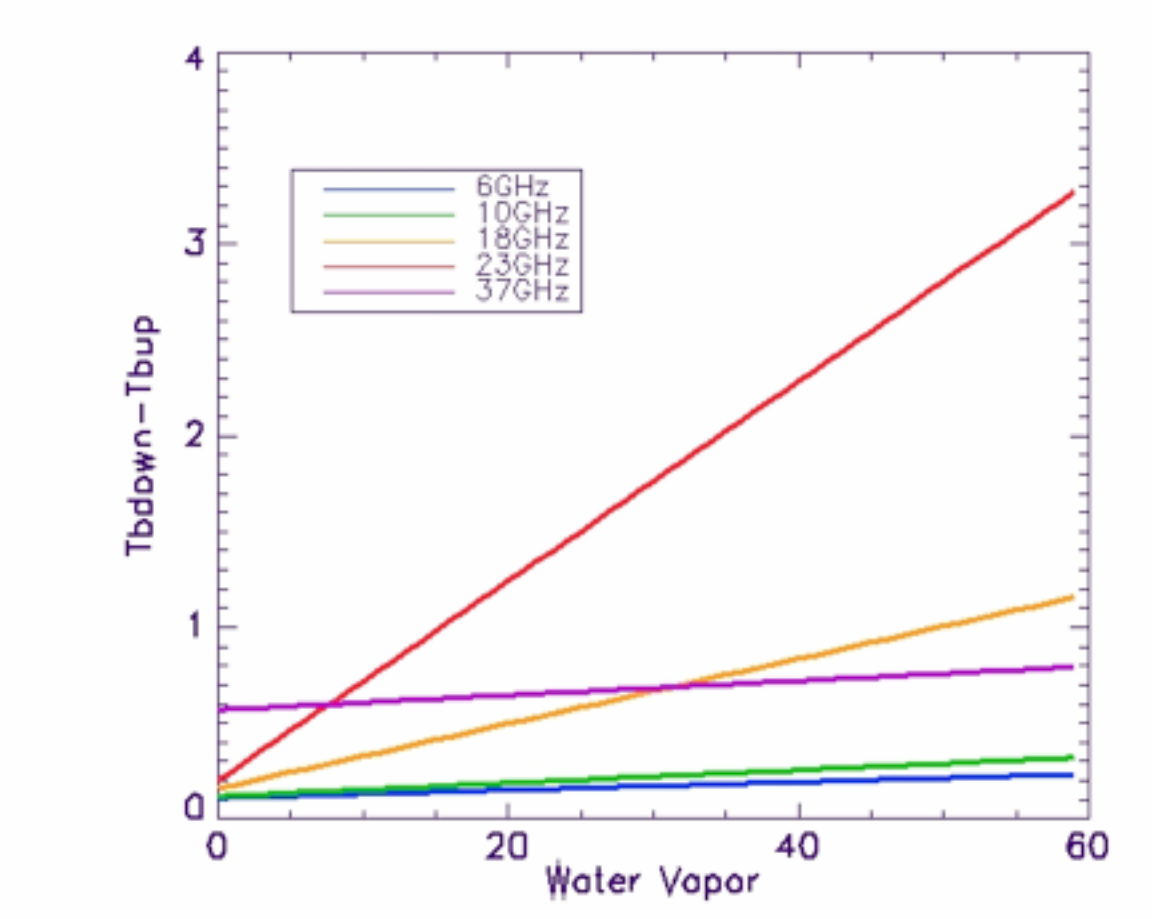

Figure 14: Effective upwelling/downwelling difference (Courtesy of Z. Jelenak) [26].

When substitute (3.4) into (3.1), the (3.1) becomes [11]

$$T_B \approx (1 - r \cdot \tau^2) T_{eff} + \tau \cdot \Delta (1 - r) + r \cdot \tau (1 - \tau) \Omega T_{eff} + (1 + \Omega) \cdot r \cdot \tau^2 T_C \qquad (3.5)$$

The last two terms in (3.5) are negligible and the total apparent brightness temperature now reduces to [11]

$$T_B \approx (1 - r \cdot \tau^2) T_{eff} + \tau \cdot \Delta (1 - r) \qquad (3.6)$$

where $\Delta = T_S - T_{eff}$.

Now let a polarimetric reflectivity ratio "*A*" be defined as the ratio of the H and V-polarization surface reflectivity, R_H and R_V respectively.

$$A \equiv \frac{R_H}{R_V} \tag{3.7}$$

When using the simplified approximation given in (3.6), the brightness temperatures can be rewritten in term of R_V as

$$T_{BV} \approx (1 - R_V \tau^2) T_{eff} + \tau \cdot \Delta (1 - R_V) \tag{3.8a}$$

$$T_{BH} \approx (1 - A R_V \tau^2) T_{eff} + \tau \cdot \Delta (1 - A R_V) \tag{3.8b}$$

When we multiply (3.8a) by *A* and subtract (3.8b), the combined brightness temperatures become

$$A T_{BV} - T_{BH} \approx (A - 1) T_{eff} + \tau \cdot \Delta (A - 1) \tag{3.9}$$

From (3.7), the *A* depends on the surface reflectivity at the time of observations. Since the surface reflectivity is a function of several parameters, some of which may not be available, it is not possible to calculate for the polarimetric reflectivity ratio. However from (3.9), the *A* may be derived as

$$A \approx \frac{T_{BH} - T_{eff} - \tau \cdot \Delta}{T_{BV} - T_{eff} - \tau \cdot \Delta} \tag{3.10}$$

To further simplify the derivation of the *A* parameter, the effective temperature T_{eff} over lower to mid troposphere and the sea surface temperature T_S is assumed to be approximately equal [11], that is $T_{eff} = T_S$, thus, $\Delta = T_S - T_{eff} = 0$, then from (3.10), the *A* reduces to

$$A \approx \frac{T_{BH} - T_S}{T_{BV} - T_S} \tag{3.11}$$

and from (3.9), the combined brightness temperature reduces to

$$A T_{BV} - T_{BH} \approx (A - 1) T_S \tag{3.12}$$

When taking a partial derivative of (3.12) with respect to τ, this brightness temperature combination becomes

$$\frac{\partial(AT_{BV} - T_{BH})}{\partial\tau} \approx 0 \tag{3.13}$$

This leads to a simple linear polarization brightness temperature combination of AT_{BV}-T_{BH} (simplify called *A*V-H) that is approximately independent of the atmospheric transmittance, which means that this combination of brightness temperature measurements is almost independent of atmospheric variables such as water vapor and low cloud liquid water (< 0.1 mm).

For the specular reflection, the reflectivity is a function of frequency, polarization, incidence angle, and the dielectric constant of the seawater. This occurs when there is no wind and the sea surface is smooth. However as the sea surface roughens by the increasing wind speed, the reflectivity decreases. Since *A* is defined as a ratio of the surface reflectivity given in (3.7), and this reflectivity is a function of several parameters including wind speed, dielectric constant of the seawater which is also a function of water temperature, foam, white caps as well as salinity, the *A* should also be a function of all these parameters; however, only wind speed and sea surface temperature was taken into account here.

To see how the simplified form of *A* given by (3.11) performs for atmospheric cancellation, a plot of *A*V-H as a function of water vapor, for the three AMSR frequency channels, is shown in Fig. 15. Overall, the 18 GHz has the flattest curve with near zero slope for most water vapor bins. All three frequencies asymptotically approach zero slope for high atmospheric water vapor > 40 mm; and at 10 GHz for water vapor < 40 mm, there is some

variability due to the high correlation between water vapor and SST. Finally, for 37 GHz the atmospheric cancellation is least successful.

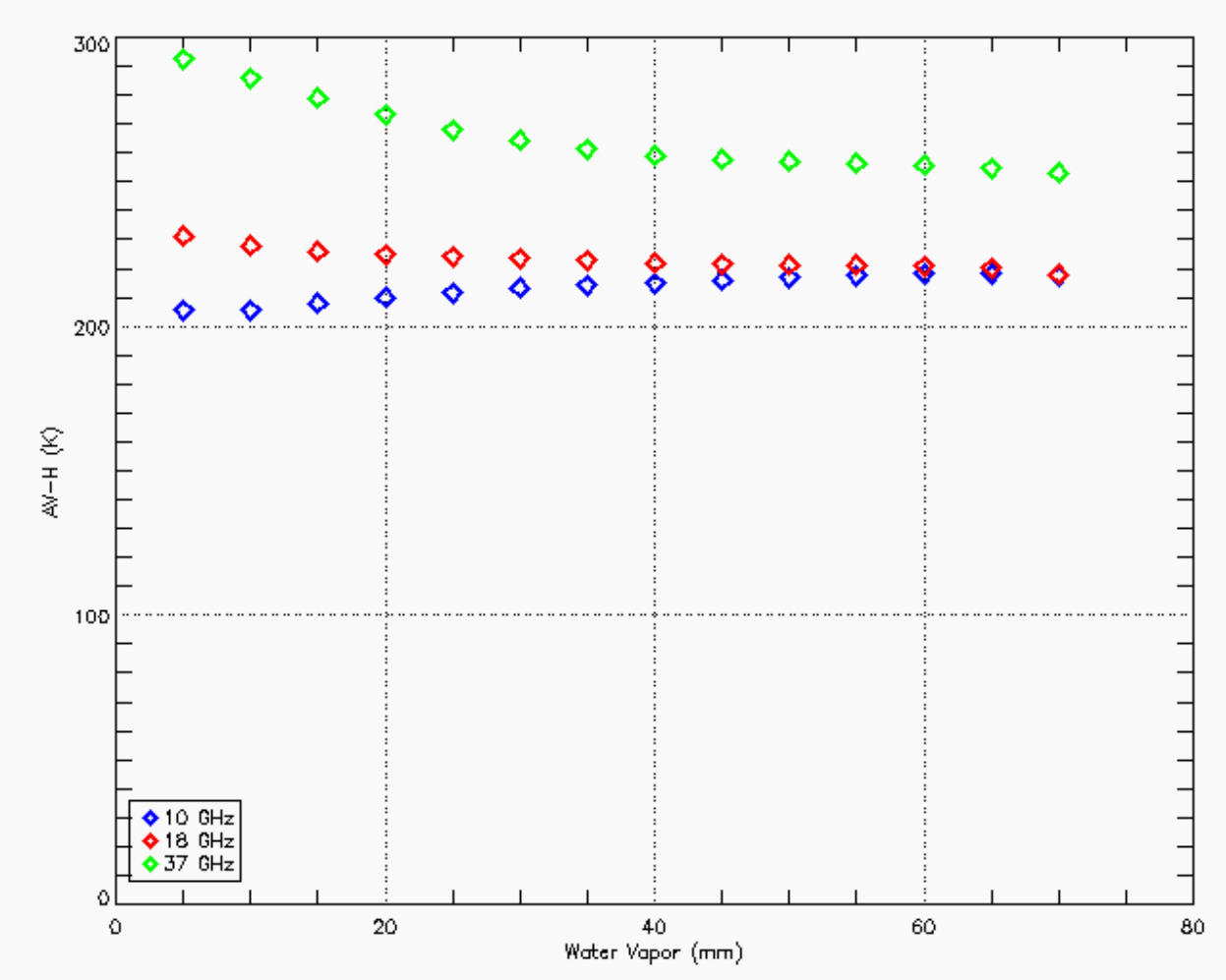

Figure 15: *A*V-H dependence on water vapor for AMSR 10, 18 and 37 GHz channels.

Using the binned dataset discussed in the previous section, the V and H brightness temperature for AMSR 10, 18 and 37 GHz channels, and the corresponding GDAS SST in (3.11), the *A* parameters are calculated for each wind speed and SST bins. A typical example of

A given in Fig. 16 (for 18 GHz in the 7 m/s and 19 °C bin) shows approximately Gaussian variability in *A* with a small variance. More examples are given in Fig. 17, where the mean values of *A* and their corresponding standard deviations (shown as error bars) are given as a function of wind speed at a fixed 19 °C SST for all three frequencies. Finally, using all wind speed and SST bins, the mean values of *A* are shown for 10, 18 and 37 GHz respectively in Fig. 18 – 20.

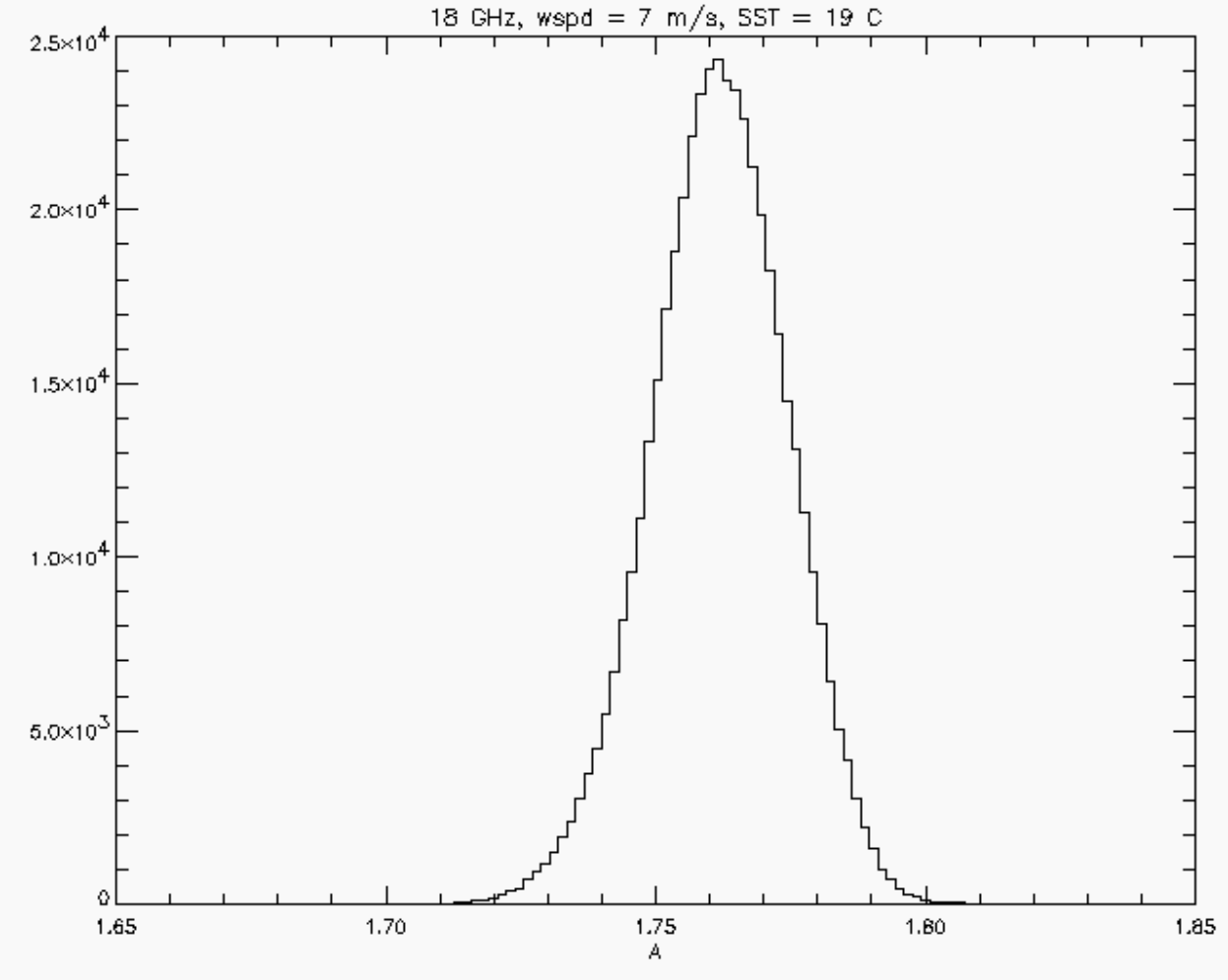

Figure 16: The *A* parameter distribution at 18 GHz for 7 m/s and 19 °C bin.

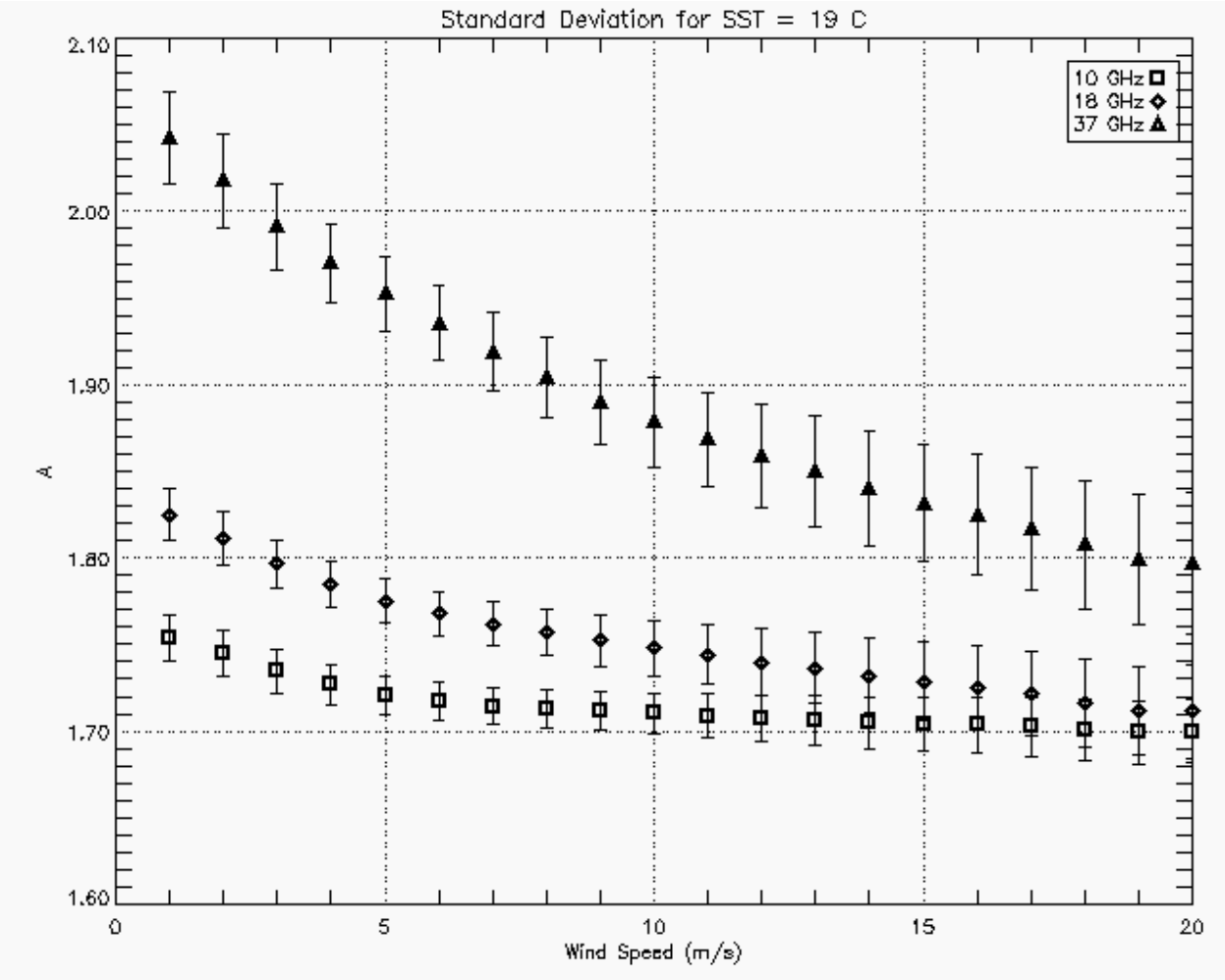

Figure 17: Mean and standard deviation of the *A* parameter as a function of wind speed for SST of 19 °C and AMSR channels of 10, 18, and 37 GHz.

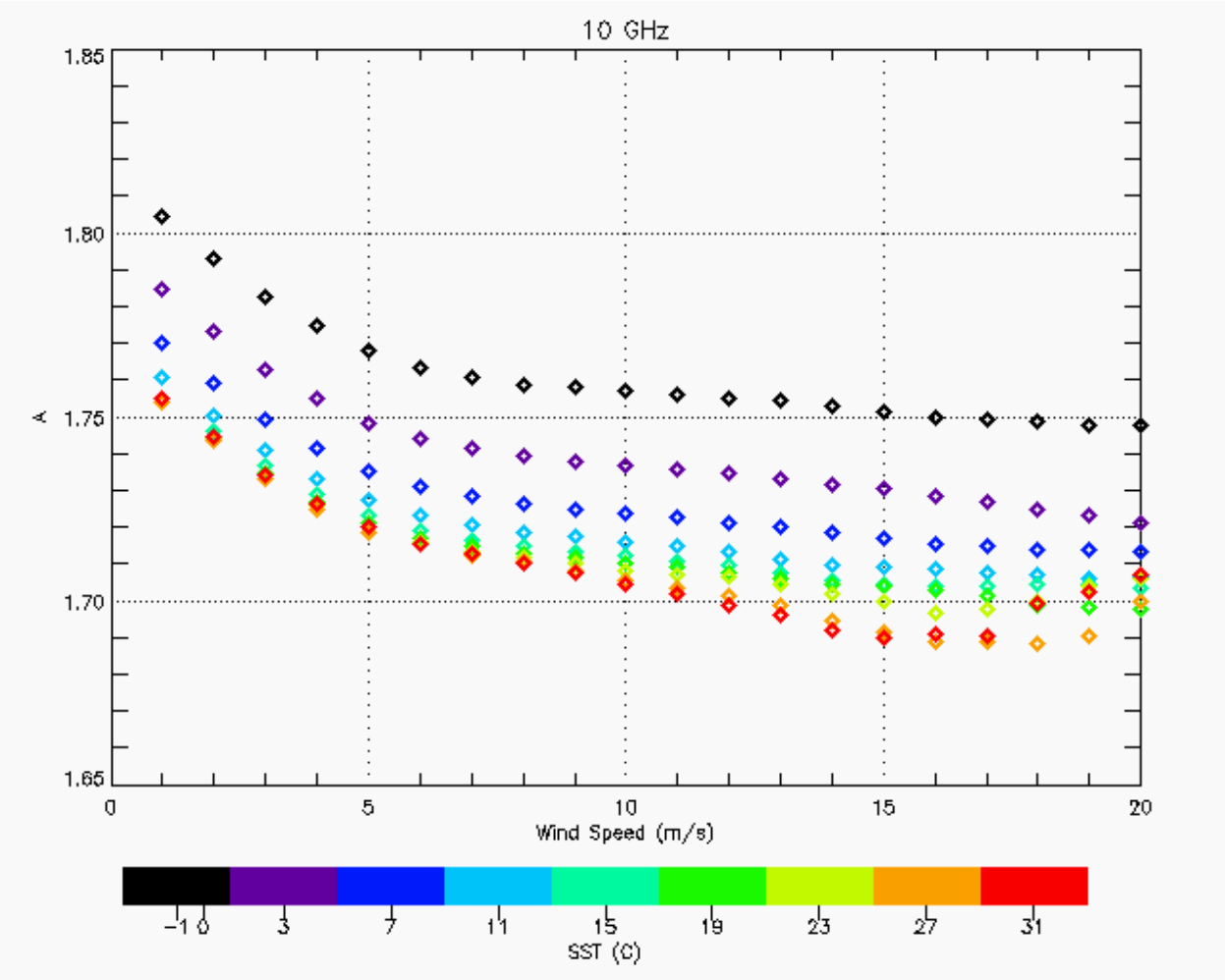

Figure 18: The *A* parameter as a function of wind speed and SST for 10 GHz.

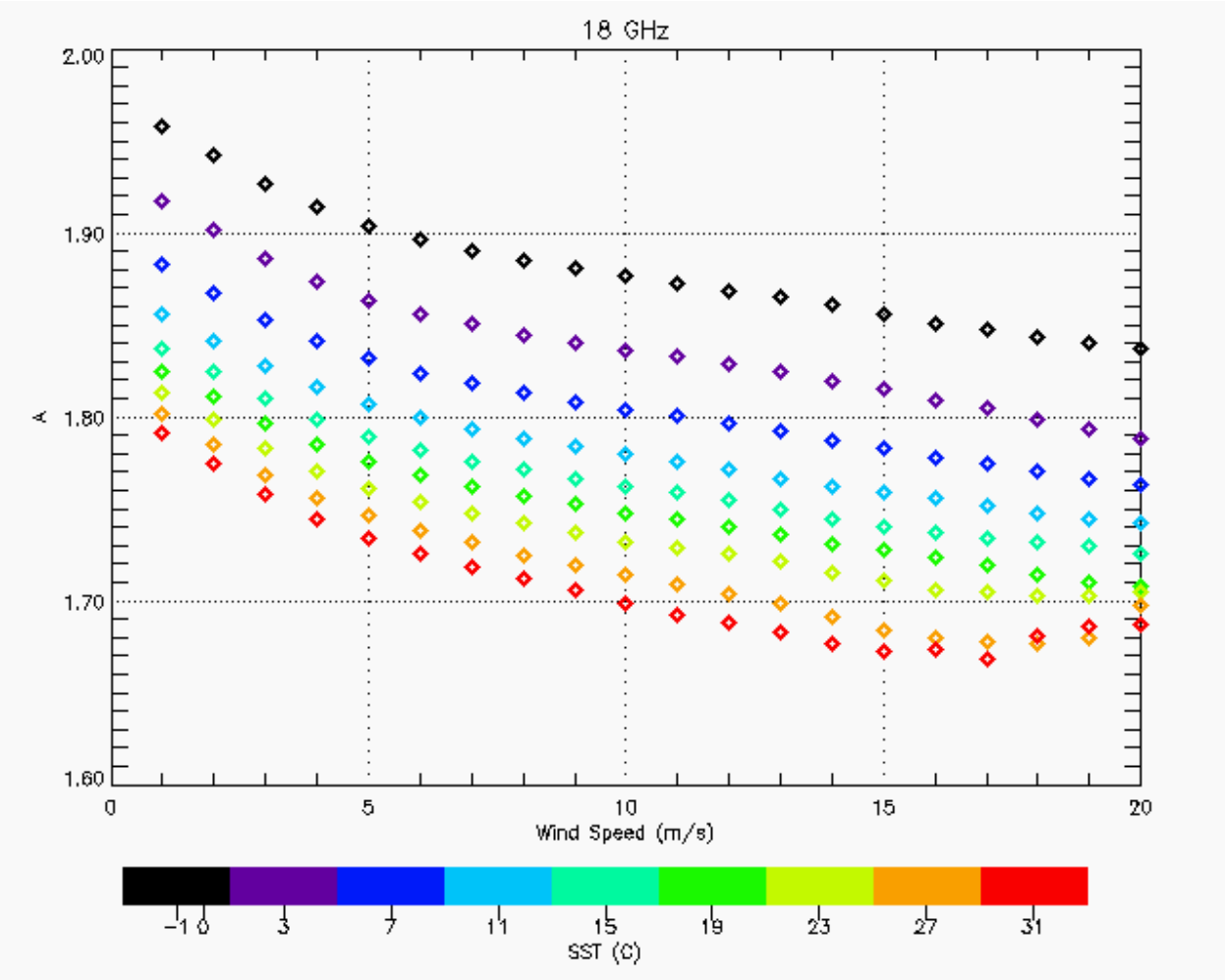

Figure 19: The *A* parameter as a function of wind speed and SST for 18 GHz.

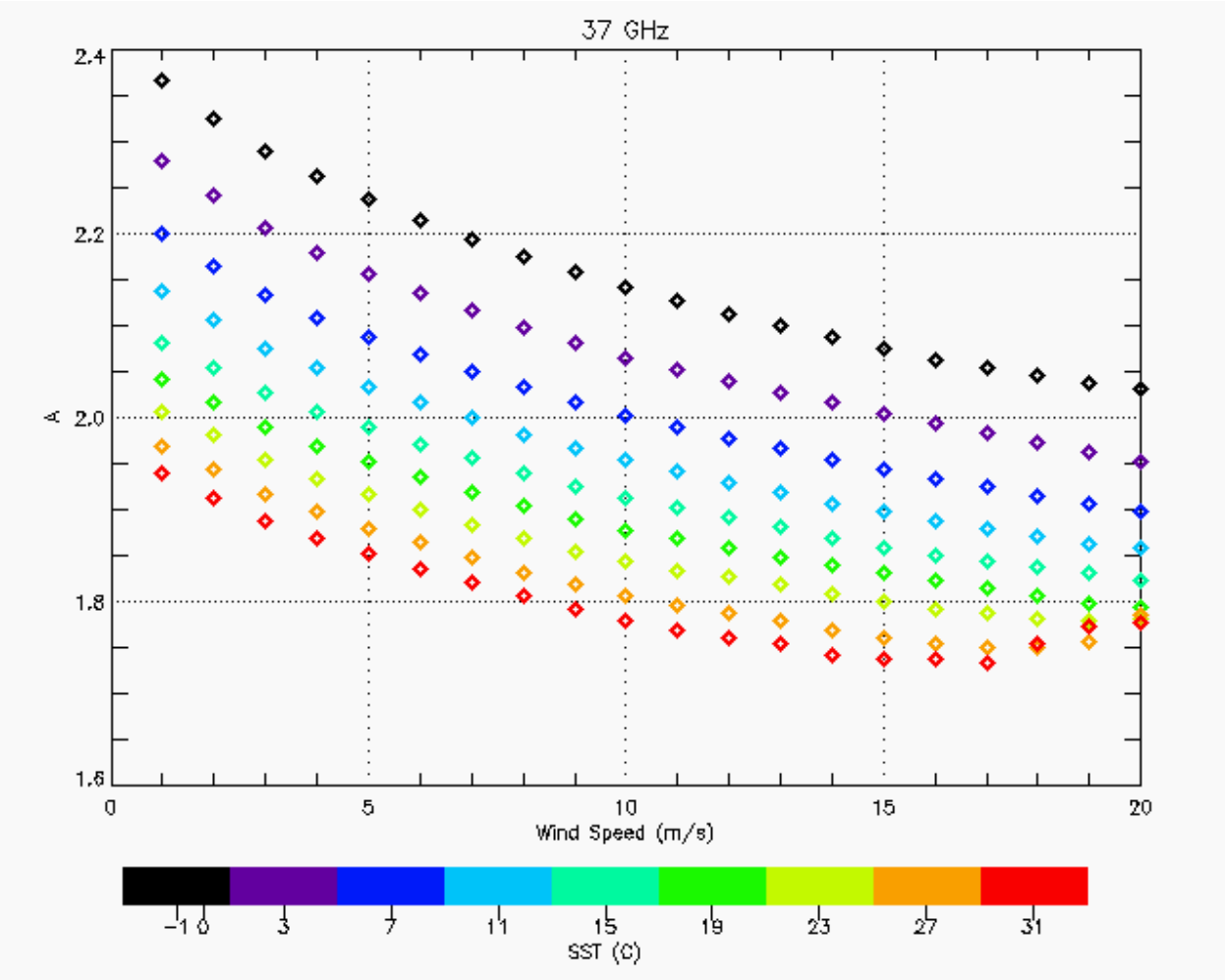

Figure 20: The *A* parameter as a function of wind speed and SST for 37 GHz.

The *A*V-H brightness temperature is now characterized as a function of wind speed and SST. By simply apply the *A* values calculated from (3.11) with the corresponding V and H AMSR brightness temperature, the average of *A*V-H is found (as a function of wind speed and SST bins) and is shown in Fig. 21 – 23. As seen in the figures, the *A*V-H relationship decreases with increasing wind speed, and the *A*V-H curves for fixed SST are approximately parallel for most of the SST bins. An exception is for the higher SST bins with wind speed greater than 15 m/s, where these data are not considered reliable due to insufficient number of data points. This characteristic allows us to model the *A*V-H as two independent additive terms that are a function of wind speed and SST as shown in (3.14). These two terms represent the average over all wind directions or the dc term of the *A*V-H GMF.

$$AT_{BV} - T_{BH} = F(WSPD) + F(SST) \tag{3.14}$$

When specular reflection occurs, the surface is smooth and the wind speed is assumed to be zero and the brightness temperature in (3.14) would be a function of only SST. The initial *F(SST)* may be found by extrapolating the *A*V-H models to wind speed equal to zero. The resulting *A*V-H as a function of SST (assuming zero wind speed and for all three frequencies) is given in Fig. 24. If the *A*V-H curves for fixed SST in Fig. 21 – 23 were perfectly parallel, they should lie on top of each other after subtracting the *F(SST)* from (3.14). However, since the curves are not perfectly parallel, the average values over all SST bins were calculated for each wind speed bins and presented by the “square symbols” in Fig. 25 – 27. These average values actually represent the *A*V-H as a function of wind speed or the *F(WSPD)* term in (3.14).

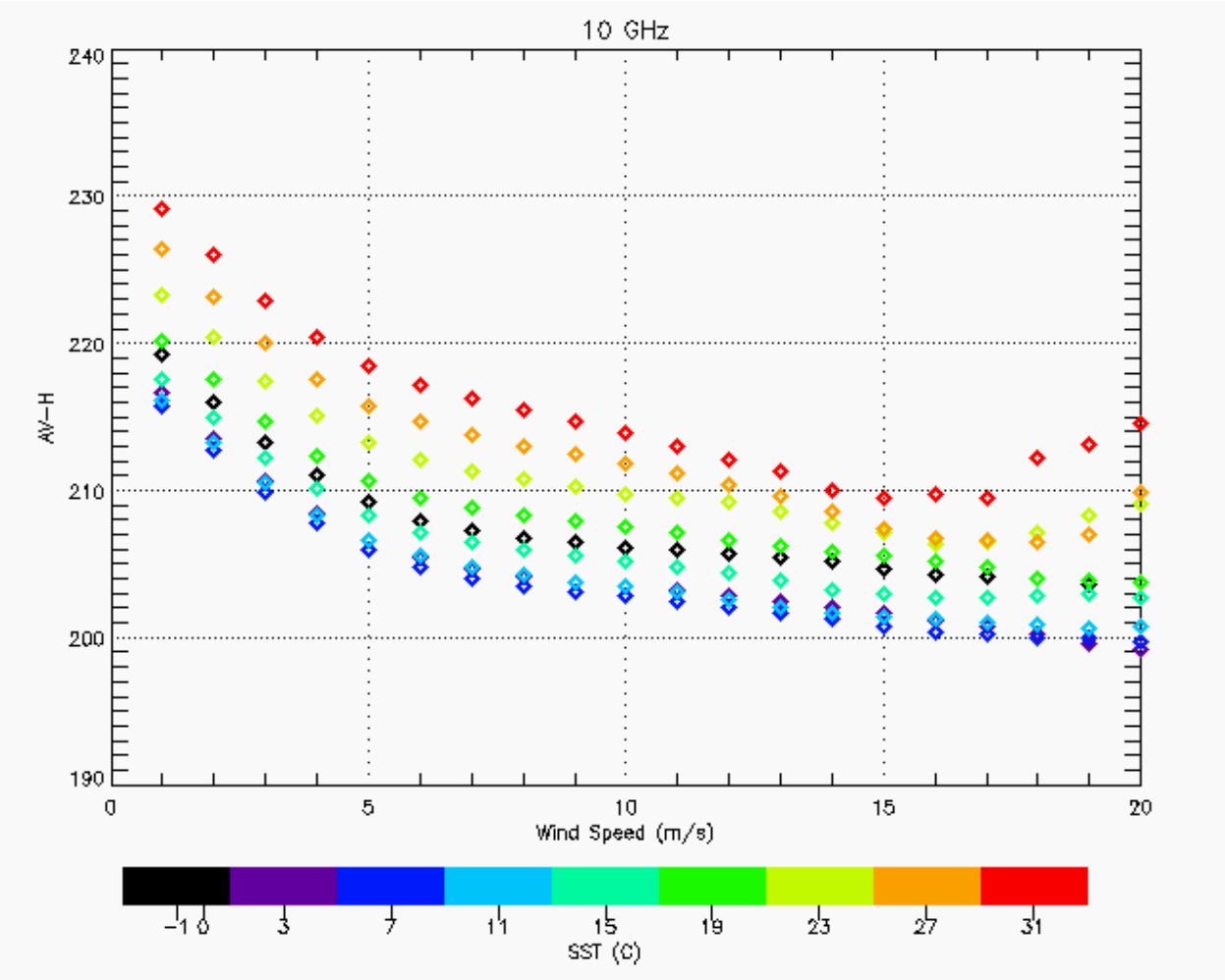

Figure 21: The *A*V-H characteristic for 10 GHz.

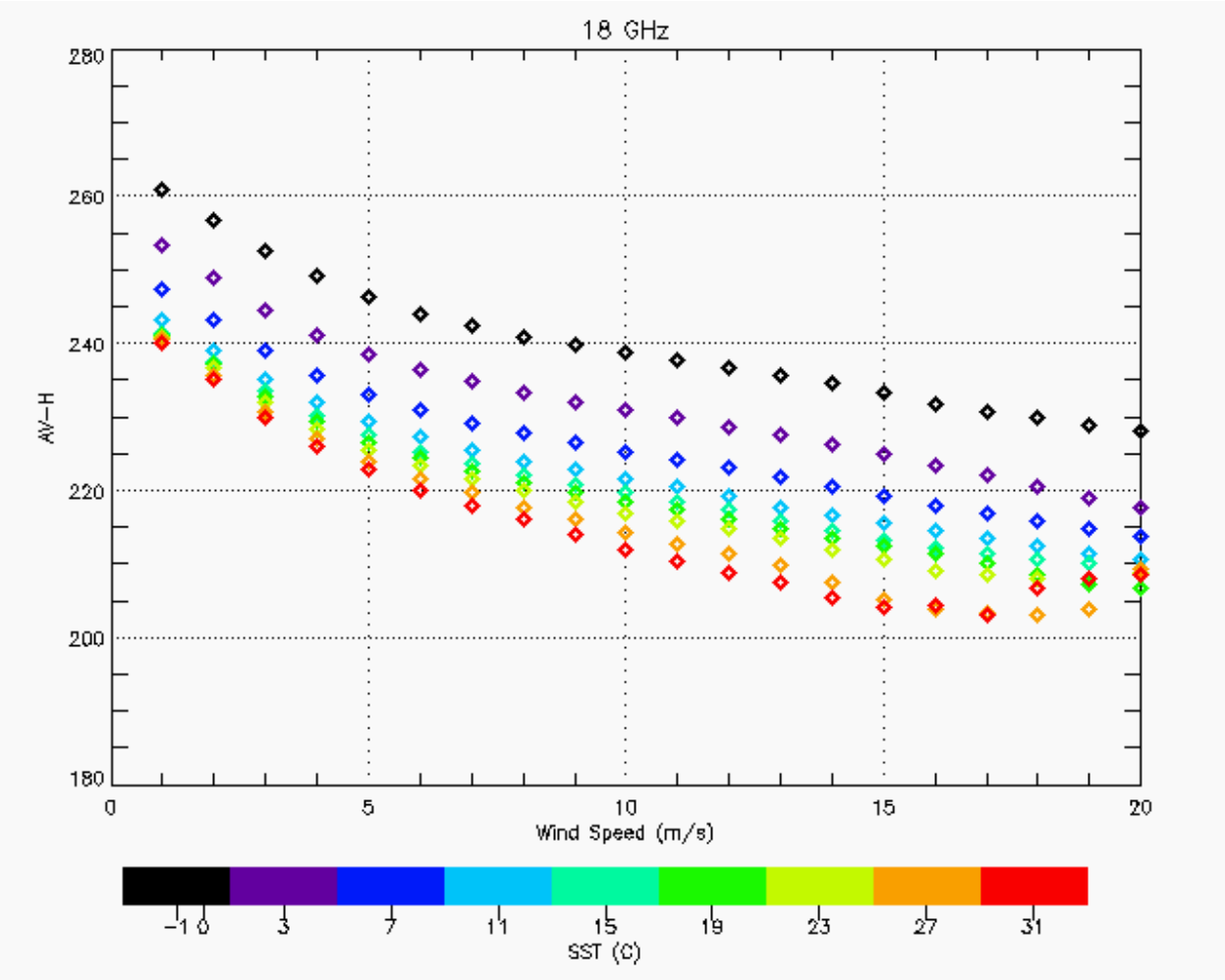

Figure 22: The *A*V-H characteristic for 18 GHz.

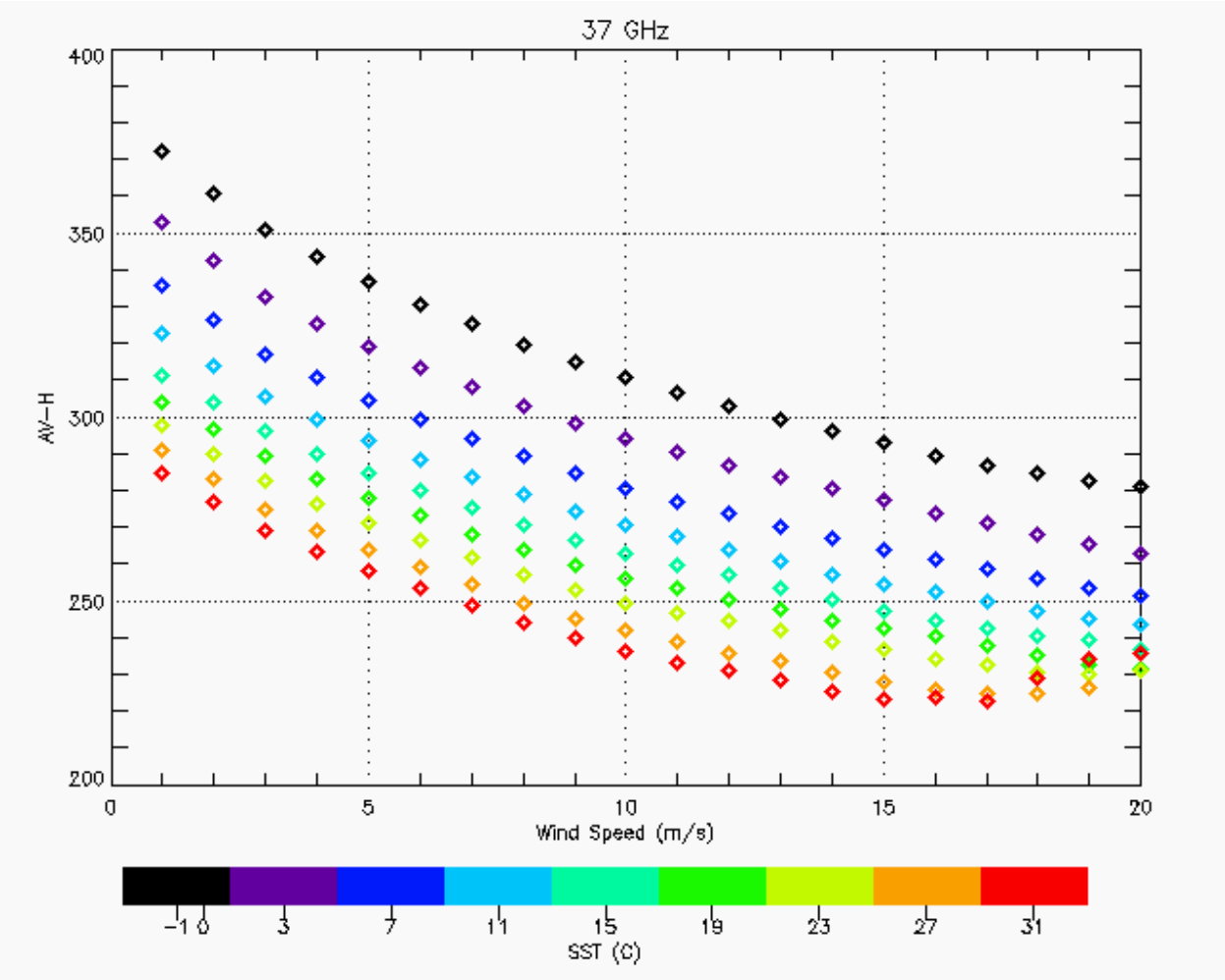

Figure 23: The *A*V-H characteristic for 37 GHz.

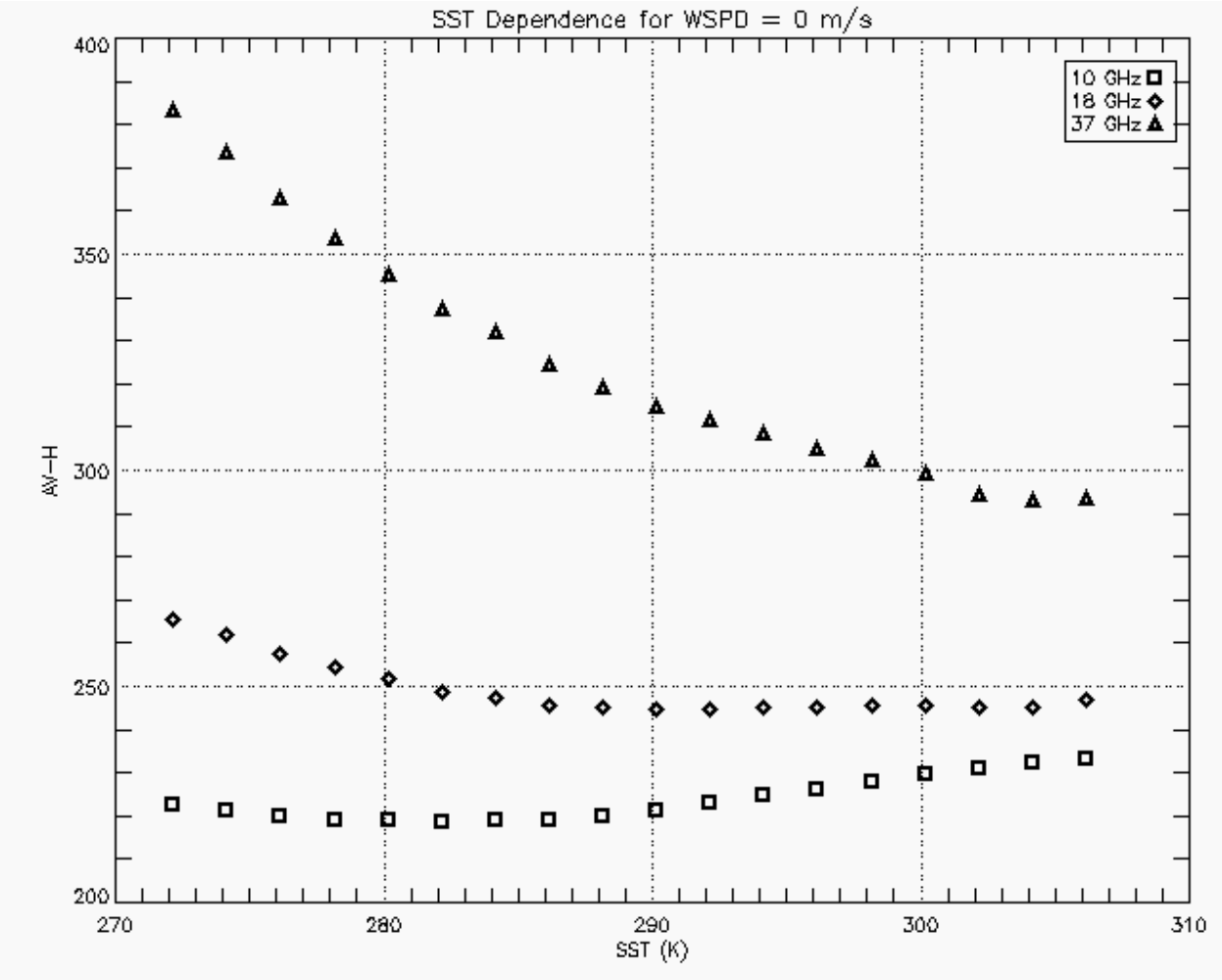

Figure 24: Initial *A*V-H for zero wind speed and AMSR 10, 18, and 37 GHz channels.

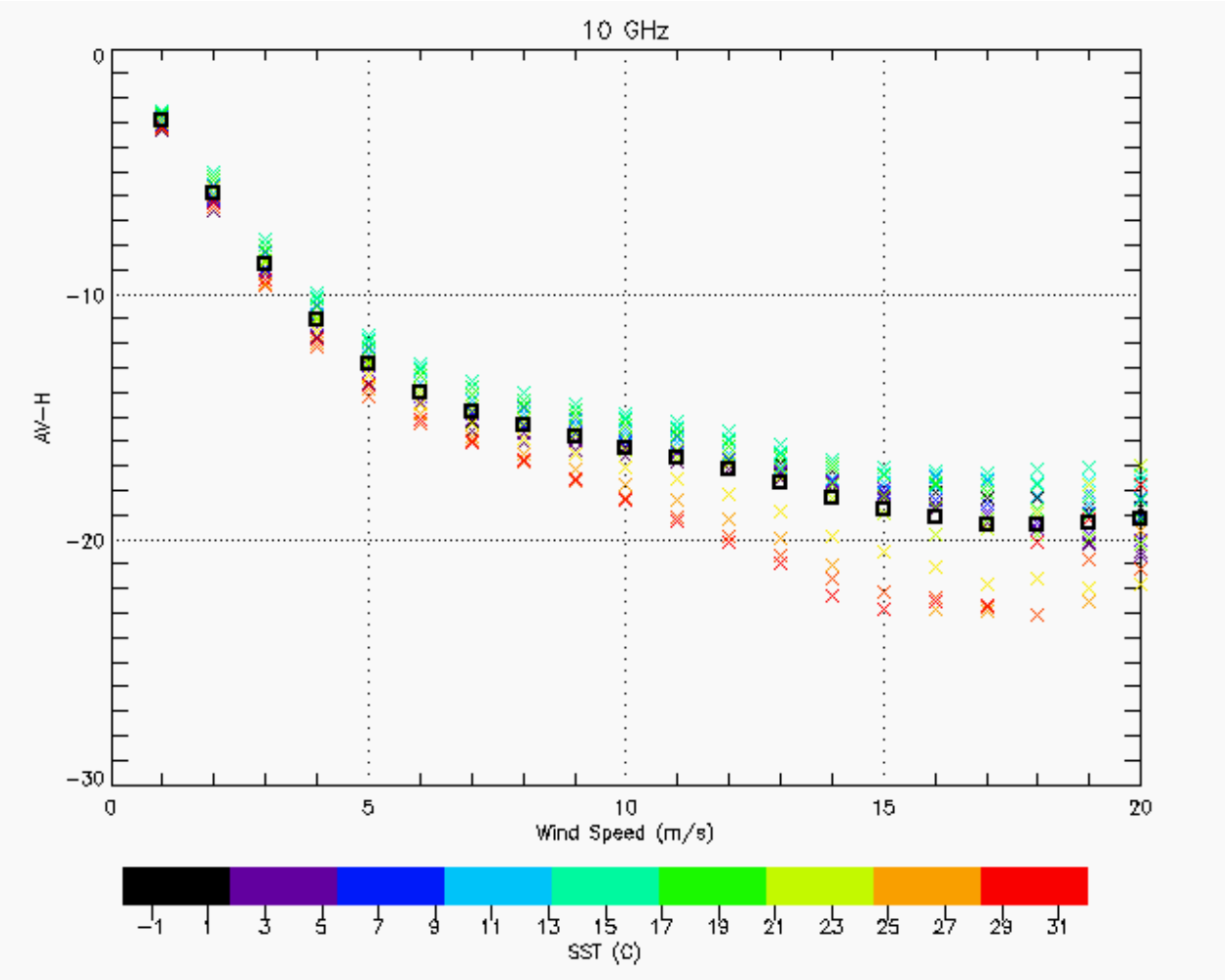

Figure 25: The *A*V-H as a function of wind speed for 10 GHz (averaged SST).

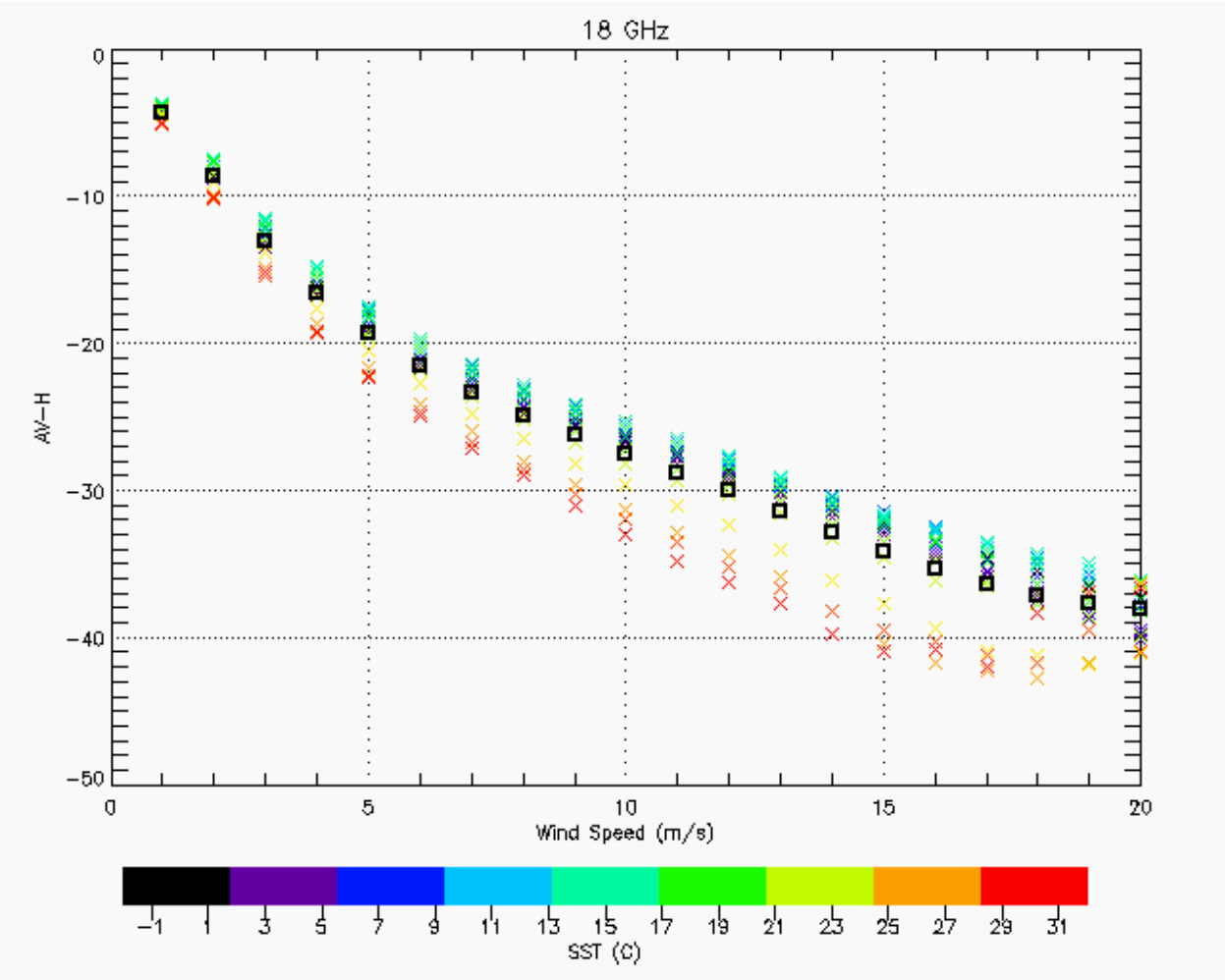

Figure 26: The *A*V-H as a function of wind speed for 18 GHz (averaged SST).

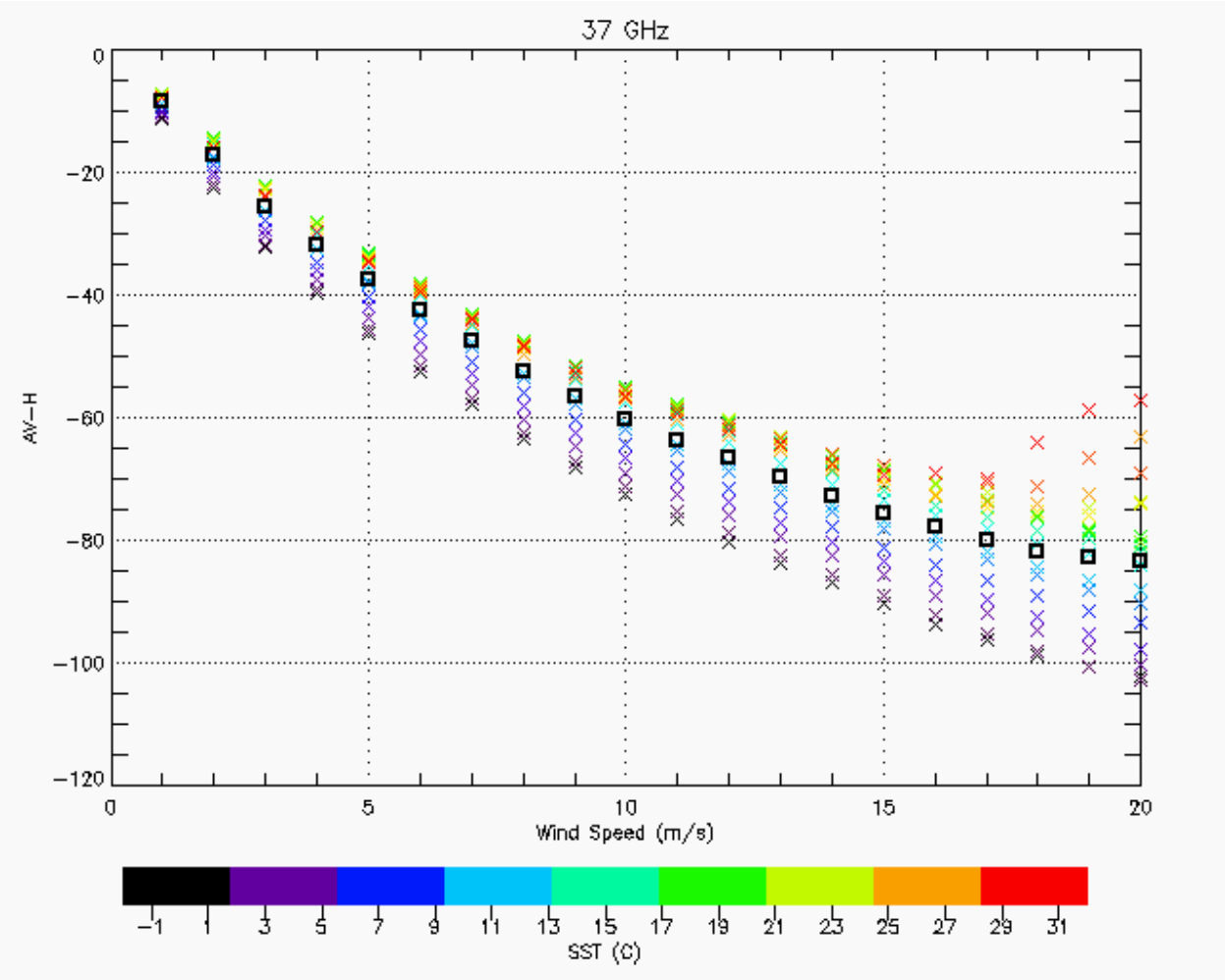

Figure 27: The *A*V-H as a function of wind speed for 37 GHz (averaged SST).

Now the averaged *A*V-H was found as a function of wind speed and SST respectively from *F(WSPD)* and *F(SST)* for a given wind speed and SST bins. In addition to wind speed and SST, the sea surface reflectivity exhibits anisotropic behavior with respect to relative wind direction [10]. The *A*V-H combinations calculated above are simply the dc terms that average over all wind direction. Thus, in order to model the azimuthal dependence of *A*V-H, additional terms were added in (3.14) and modeled by using the two harmonic cosine functions as given in (3.15)

$$AT_{BV} - T_{BH} = \underbrace{F(WSPD) + F(SST)}_{dc} + C_1(WSPD) \cdot COS(\chi) + C_2(WSPD) \cdot COS(2\chi) \quad (3.15)$$

The relative wind direction here is defined as the difference between the AMSR observed azimuth angle and the wind direction with respect to North. The meteorological wind direction convention was used in this analysis, and the true wind direction was assumed to be the selected solution obtained from SeaWinds scatterometer's retrieved directions. The relative wind direction concept is illustrated in Fig. 28. This may be expressed mathematically as

$$\chi = Azimuth - Direction \quad (3.16)$$

The wind direction dependence of *A*V-H is expressed through the last two terms of (3.15). It can be calculated by subtracting the dc wind speed and SST dependence terms from the overall *A*V-H measurement and this defines the vector wind dependence as

$$F(WDIR) = C_1(WSPD) \cdot COS(\chi) + C_2(WSPD) \cdot COS(2\chi) \quad (3.17)$$

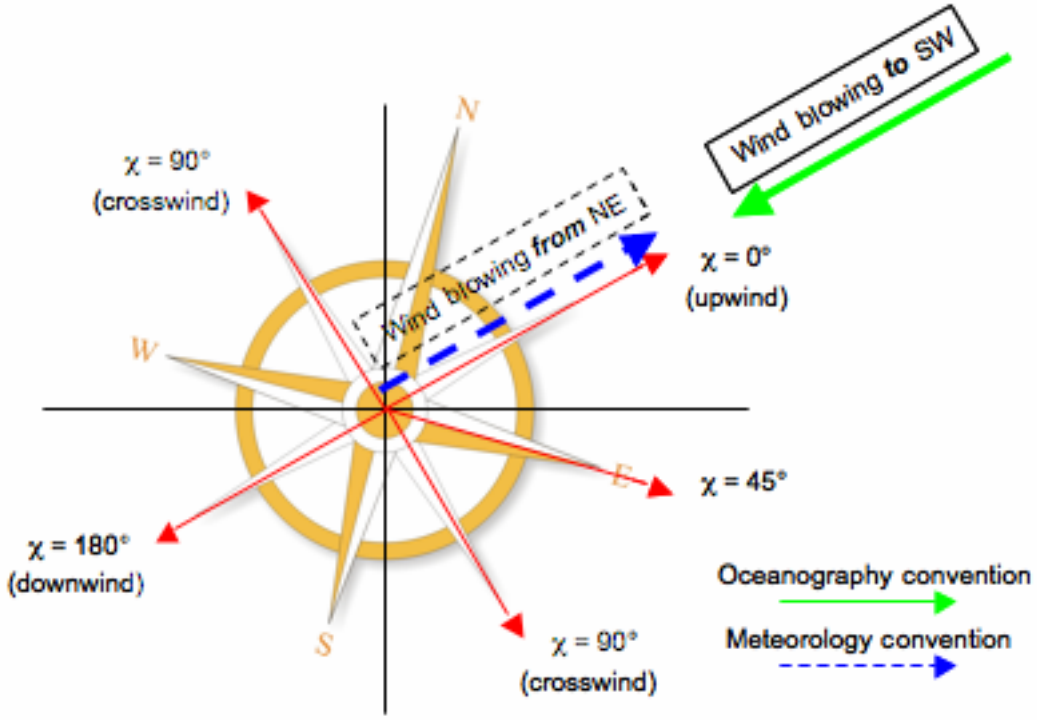

Figure 28: Relative wind direction convention [*background compass from http://2004.njsummerreading.org/librarians/logs/compass_300dpi.jpg*].

The *F(WDIR)* is a function of the relative wind direction as well as the wind speed. This was empirically determined by calculating the average *F(WDIR)* for the relative wind direction binned every 10°, and the results at 7 m/s are presented for the three AMSR channels in Fig. 29. Note that the mean *F(WDIR)* over all relative wind directions should equal to zero as predicted in (3.17), however, in Fig. 29 the mean *F(WDIR)* has a bias due non-cancelled surface and atmospheric variation. This bias is caused by the following: error in the initial *F(SST)* by assuming zero wind speed, error in the estimated values of *F(WSPD)* by taking the mean values over all SST, and error caused by non-cancelled water vapor variation because of the estimated

value for the *A* parameter. To reduce these errors, the directional dependence *F(WDIR)* was calculated by regressing the measurements using a double cosine harmonic function plus a dc term that is a function of wind speed as given in (3.18). The new term, C_0, is equivalent to the *F(WSPD)* described above.

$$F(WDIR) = C_0(WSPD) + C_1(WSPD) \cdot COS(\chi) + C_2(WSPD) \cdot COS(2\chi) \tag{3.18}$$

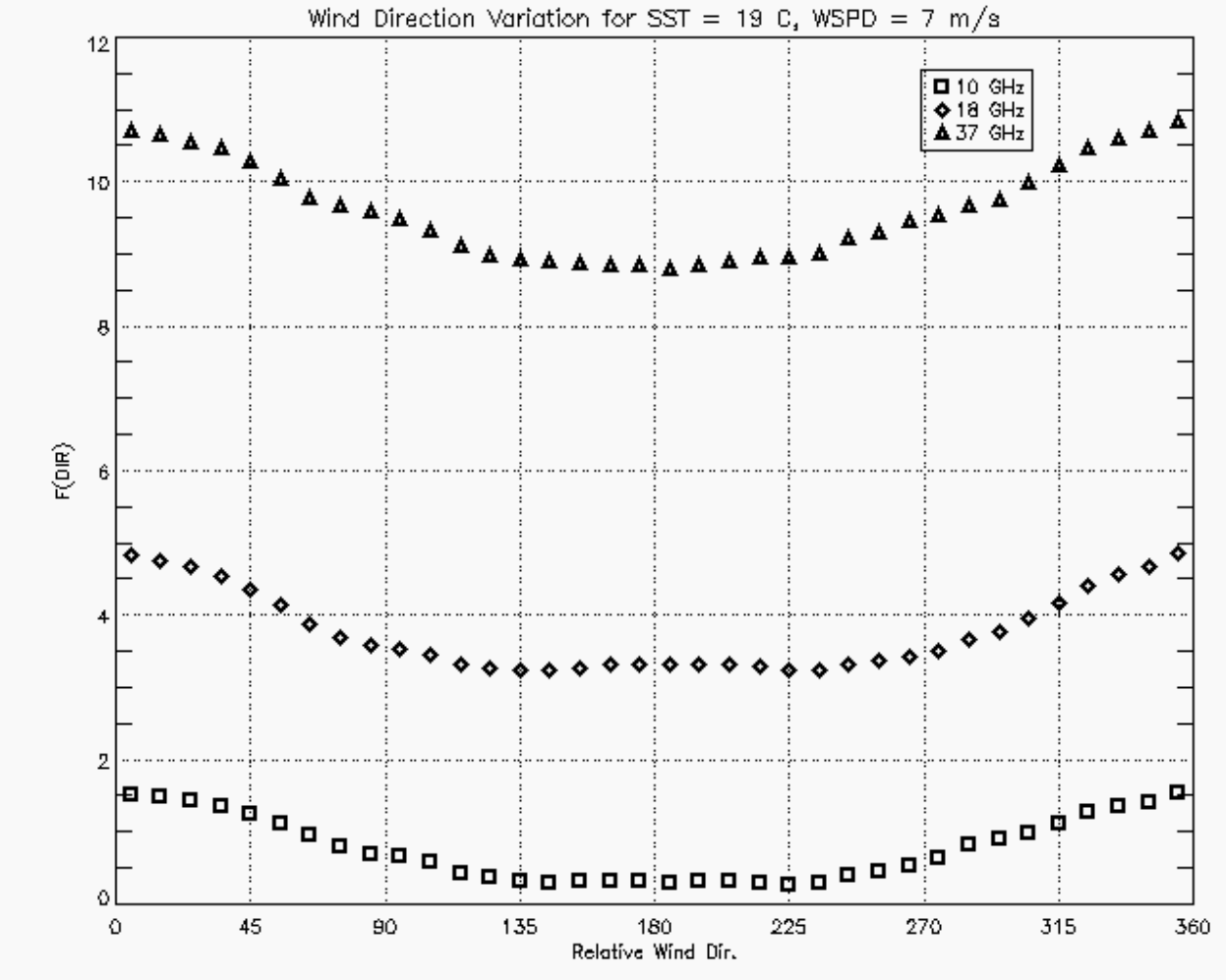

Figure 29: Example *F(WDIR)* wind direction anisotropy for SST = 19 °C and WSPD = 7 m/s.

Model Function

In this section, the procedure used to obtain the passive model function coefficients is described. The model function was found by using a proper mathematical function to regress the averaged *A*V-H measurements as a function of the appropriate parameters. From (3.15), the *A*V-H model may be rewritten in the form

$$AV-H = F(SST) + C_0(WSPD) + C_1(WSPD)\cdot COS(\chi) + C_2(WSPD)\cdot COS(2\chi) \qquad (3.19)$$

The initial *F(SST)* was found as shown in Fig. 24 by assuming a specular reflection (WSPD = 0). This initial *F(SST)* was the average of the *A*V-H measurements in 2.0 °C bins based on the GDAS model SST. A regression analysis was performed to model the SST dependence, and the resulting best fit for these initial *F(SST)* measurements is shown in Fig. 30 for 10, 18 and 37 GHz channels. Note that the *F(SST)* here is a function of SST in Kelvin.

Next using this function and subtracting from the individual measurement of *A*V-H, the resulting wind vector dependence term is modeled in (3.20).

$$(AV-H) - F(SST) = C_0(WSPD) + C_1(WSPD)\cdot COS(\chi) + C_2(WSPD)\cdot COS(2\chi) \qquad (3.20)$$

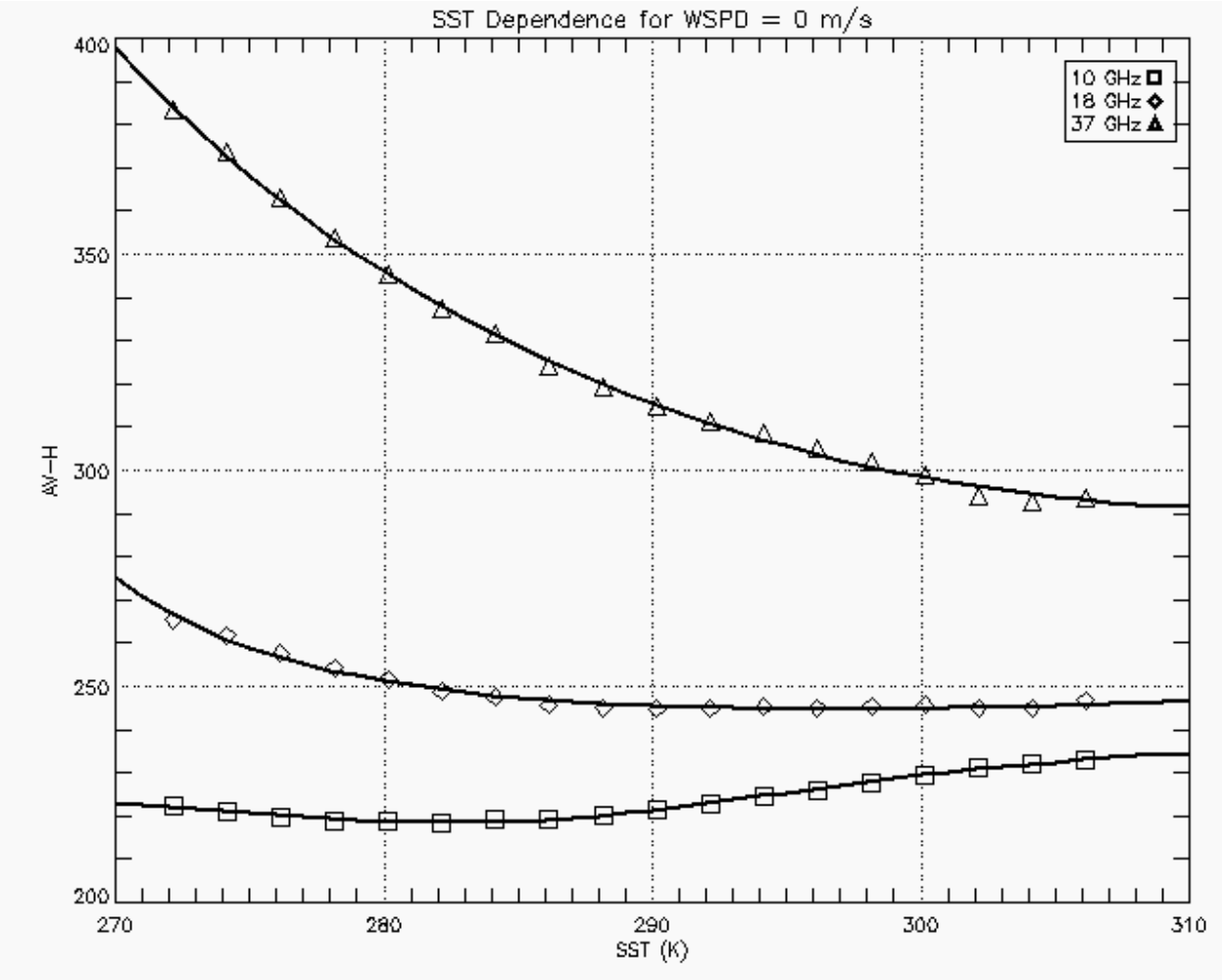

Figure 30: Initial *F(SST)* dependence function for zero wind speed and three AMSR channels.

After removing the SST contribution from each *A*V-H measurement and sorting them within wind speed and relative wind direction bins, the mean values for each bin were calculated. These data were used to calculate the geophysical model function (C_0, C_1 and C_2) as shown in (3.20). An example of the model function fit is shown for the 18 GHz channel with selected wind speeds in Fig. 31. Since the *"C"* coefficients were found for discrete value of wind speed, an additional regression step was required to obtain analytical functions that were the coefficients that were valid across the entire wind speed range. With this initial function of *"C"* coefficients, an iteration process was established.

The second iteration was started by refining the *F(SST)* function. In the first iteration, the initial F(SST) was found by assume zero wind speed; but now the initial wind speed and direction dependence function is available. By subtracting using this GMF that is defined for all wind speed values from the measured *A*V-H, the remaining result is a function of SST only as shown in (3.21).

$$(AV-H)-[C_0(WSPD)+C_1(WSPD)\cdot COS(\chi)+C_2(WSPD)\cdot COS(2\chi)]=F(SST) \quad (3.21)$$

The procedure was repeated to find the proper mathematical form that best fit the mean values for each SST bin and the new coefficients for *F(SST)* was found. The new GMF coefficients were found by repeating this process with newly evaluated *F(SST)* subtracted from the *A*V-H measurements.

After several iterations, the final functional form for *F(SST)* and the GMF *"C"* coefficients converged and remained the same. The GMF after the last iteration represents the empirical model for *A*V-H brightness temperature as a function of SST and vector wind as defined in (3.19). The empirical model equations and model coefficients used are presented in Table 2 and Table 3 respectively.

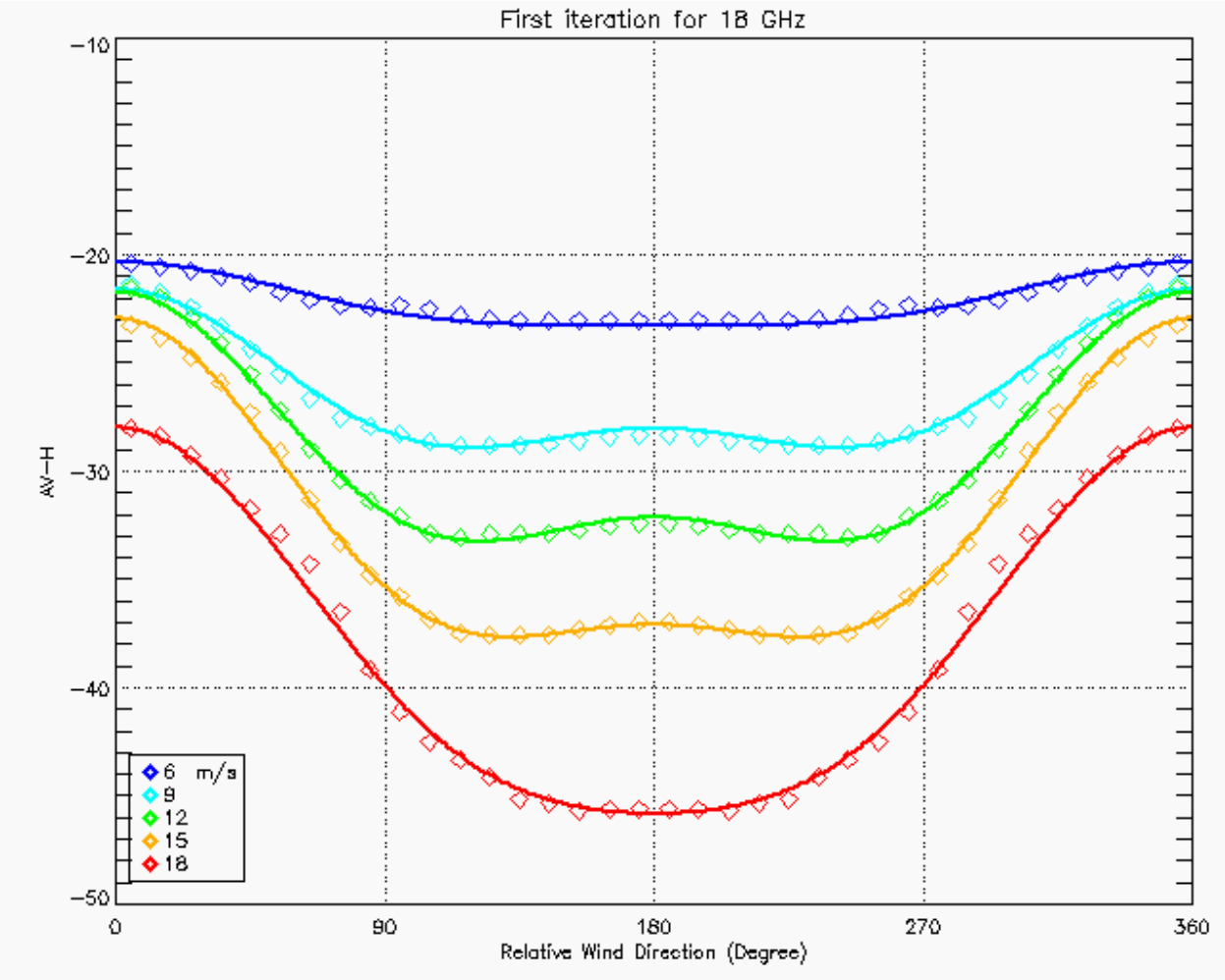

Figure 31: GMF first iteration wind vector dependence for 18 GHz, after removal of *F(SST)*.

Table 2 The model function mathematical forms.

	F(SST)	C_0(WSPD)
10 GHz	$\frac{a+c\cdot x+e\cdot x^2}{1+b\cdot x+d\cdot x^2}$ *	$\frac{a+c\cdot x+e\cdot x^2+g\cdot x^3}{1+b\cdot x+d\cdot x^2+f\cdot x^3}$
18 GHz	$\frac{a+c\cdot x}{1+b\cdot x}$ *	$\frac{a+c\cdot x+e\cdot x^2+g\cdot x^3}{1+b\cdot x+d\cdot x^2+f\cdot x^3}$
37 GHz	$\frac{a+c\cdot x}{1+b\cdot x}$ *	$\frac{a+c\cdot x+e\cdot x^2+g\cdot x^3}{1+b\cdot x+d\cdot x^2+f\cdot x^3}$
* Last points was excluded.		

	C_1(WSPD)	C_2(WSPD)
10 GHz	$\frac{a+c\cdot x+e\cdot x^2}{1+b\cdot x+d\cdot x^2}$	$\frac{a+c\cdot x+e\cdot x^2+g\cdot x^3}{1+b\cdot x+d\cdot x^2+f\cdot x^3+h\cdot x^4}$ **
18 GHz	$\frac{a+c\cdot x+e\cdot x^2}{1+b\cdot x+d\cdot x^2}$	$\frac{a+c\cdot x+e\cdot x^2+g\cdot x^3}{1+b\cdot x+d\cdot x^2+f\cdot x^3+h\cdot x^4}$ **
37 GHz	$\frac{a+c\cdot x+e\cdot x^2}{1+b\cdot x+d\cdot x^2}$	$\frac{a+c\cdot x+e\cdot x^2+g\cdot x^3}{1+b\cdot x+d\cdot x^2+f\cdot x^3+h\cdot x^4}$ **
** First four points was weighted half.		

Table 3 The model function coefficients.

	F(SST)	C_0(WSPD)
10 GHz	a= 253.621158785647065 b= -0.00718552626221650191 c= -1.82060139588702884 d= 1.30310069705454942e-05 e= 0.00329423915253750657	a= 0.00965187186398981844 b= -0.149622985574859288 c= -3.19049794244812171 d= 0.013897639314581152 e= 0.577524219142330443 f= 0.00325949020888421041 g= -0.0943273507983251161
18 GHz	a= 235.470095002711386 b= -0.0038033763341366219 c= -0.899638800928911108	a= 0.000522257751556204275 b= -0.109963903887493617 c= -4.27608876205248015 d= 0.0292254372104173536 e= 0.212675747064022248 f= 0.00040128736418452545 5 g= -0.0684580012788550327
37 GHz	a= 198.585358511920311 b= -0.00419021758632681259 c= -0.920565333848179437	a= -0.0289749115449385766 b= -0.339940338334251616 c= -8.11442835793787668 d= 0.0809213778926692934 e= 2.52238113104073392 f= 0.00307056353121112192 g= -0.688302938249477265

Note: The required number of significant digits are presented.

	C_1(WSPD)	C_2(WSPD)
10 GHz	a= 0.00053663753165292882 b= 0.104823539762490071 c= -0.130910317196439013 d= -0.000244988375917665765 e= 0.0526074869350466518	a= 0.0371722137190973911 b= -0.260046164406998058 c= -0.171088458328255879 d= 0.0401384406482446197 e= 0.0339172741279560395 f= -0.00233126655136227377 g= -0.00109950329124836926 h= 5.07900772194225948e-05
18 GHz	a= 0.0213593249397492412 b= -0.0196333164316611127 c= -0.235462617832914204 d= 0.00541353696011305504 e= 0.0746486614629487237	a= 0.0694756696559167866 b= -0.215505224381576415 c= -0.378361771322239182 d= 0.0381164648662323972 e= 0.0830858379714277173 f= -0.00226187916136070823 g= -0.00289484158905869134 h= 5.08760324294707472e-05
37 GHz	a= 0.0446546397222031288 b= -0.00236642705693845145 c= -0.54781788770743733 d= 0.00728694872741907987 e= 0.158276587392093172	a= 0.071686328123967732 b= -0.331596694406877809 c= -0.865627335524183424 d= 0.106960182097611076 e= 0.183194512996184008 f= -0.00875918330908980999 g= -0.00666264554142661347 h= 0.000232121210383896865

Note: The required number of significant digits are presented.

Using the functional forms and corresponding coefficients from Table 2 and Table 3 for three AMSR frequency channels, the model function is plotted for each component of the model: *F(SST)*, C_0, C_1 and C_2 as shown in Fig. 32 – 35 respectively. The symbols represent the mean value of the measurements and the solid lines represent the model functions. From these *C* coefficients, the wind vector anisotropy is plotted with dc term C_0 removed as shown in Fig. 36 – 38 for 10, 18 and 37 GHz respectively with some selected wind speed ranges.

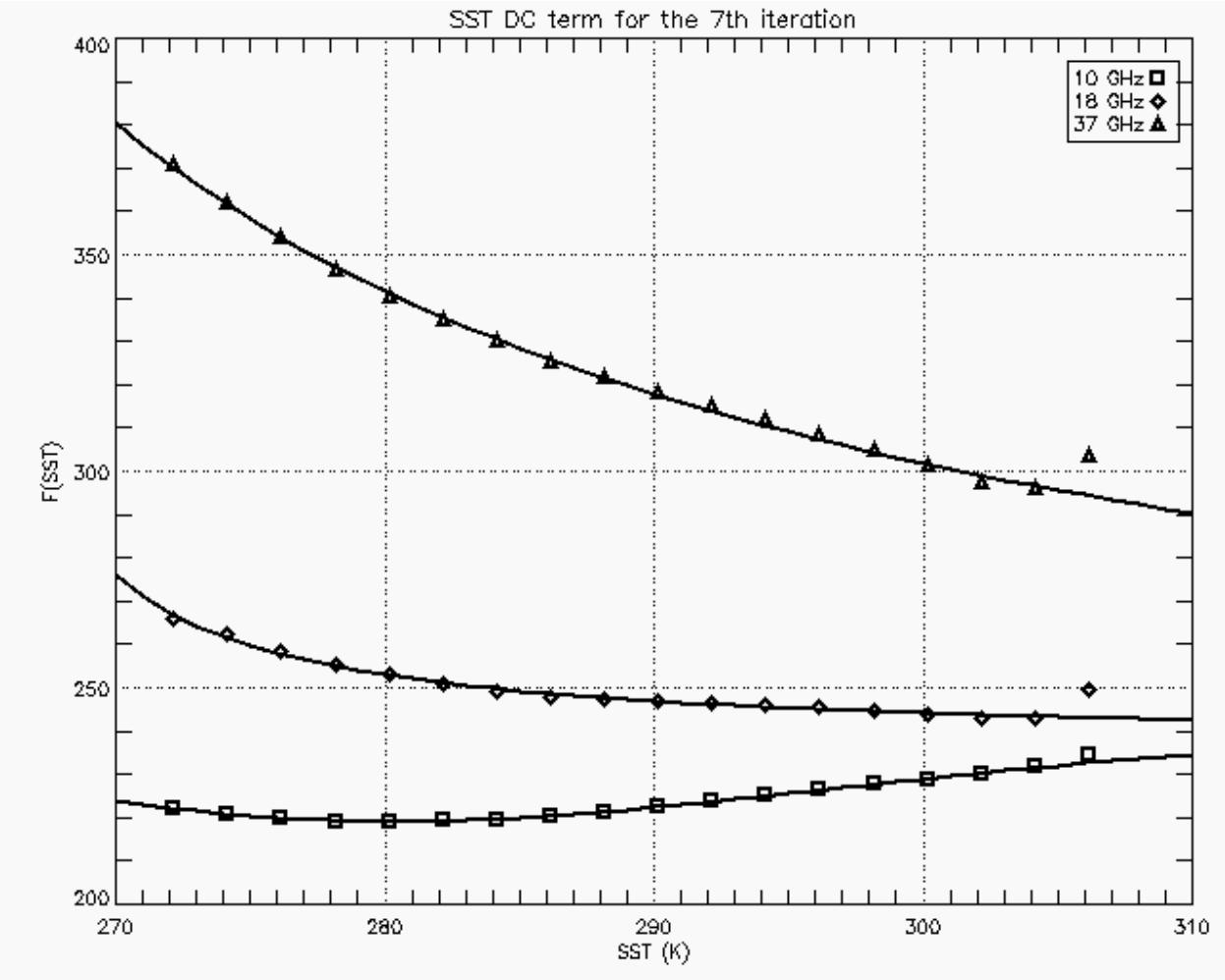

Figure 32: The model function dependence of sea surface temperature, *F(SST)*.

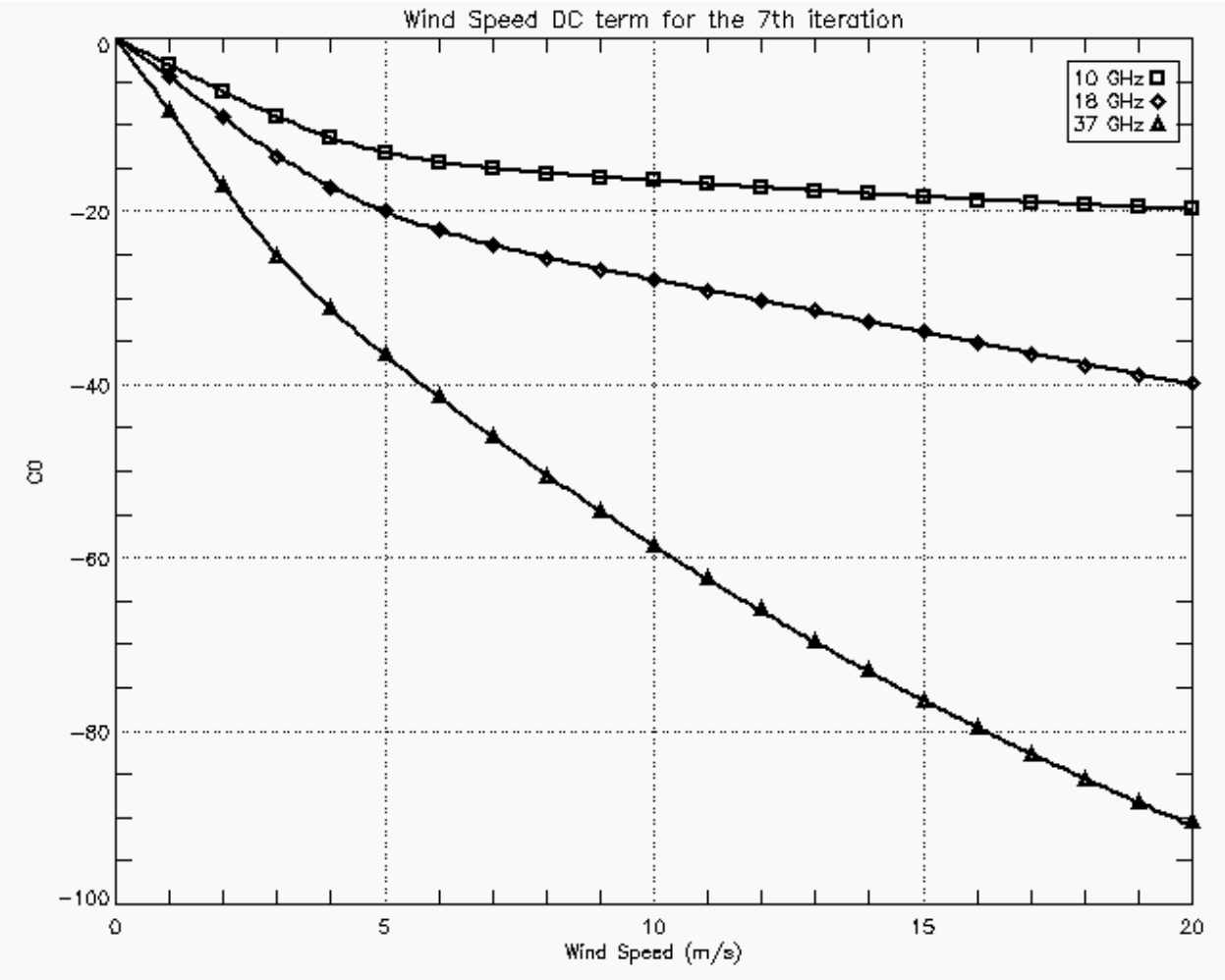

Figure 33: The DC model function dependence of wind speed, C_0.

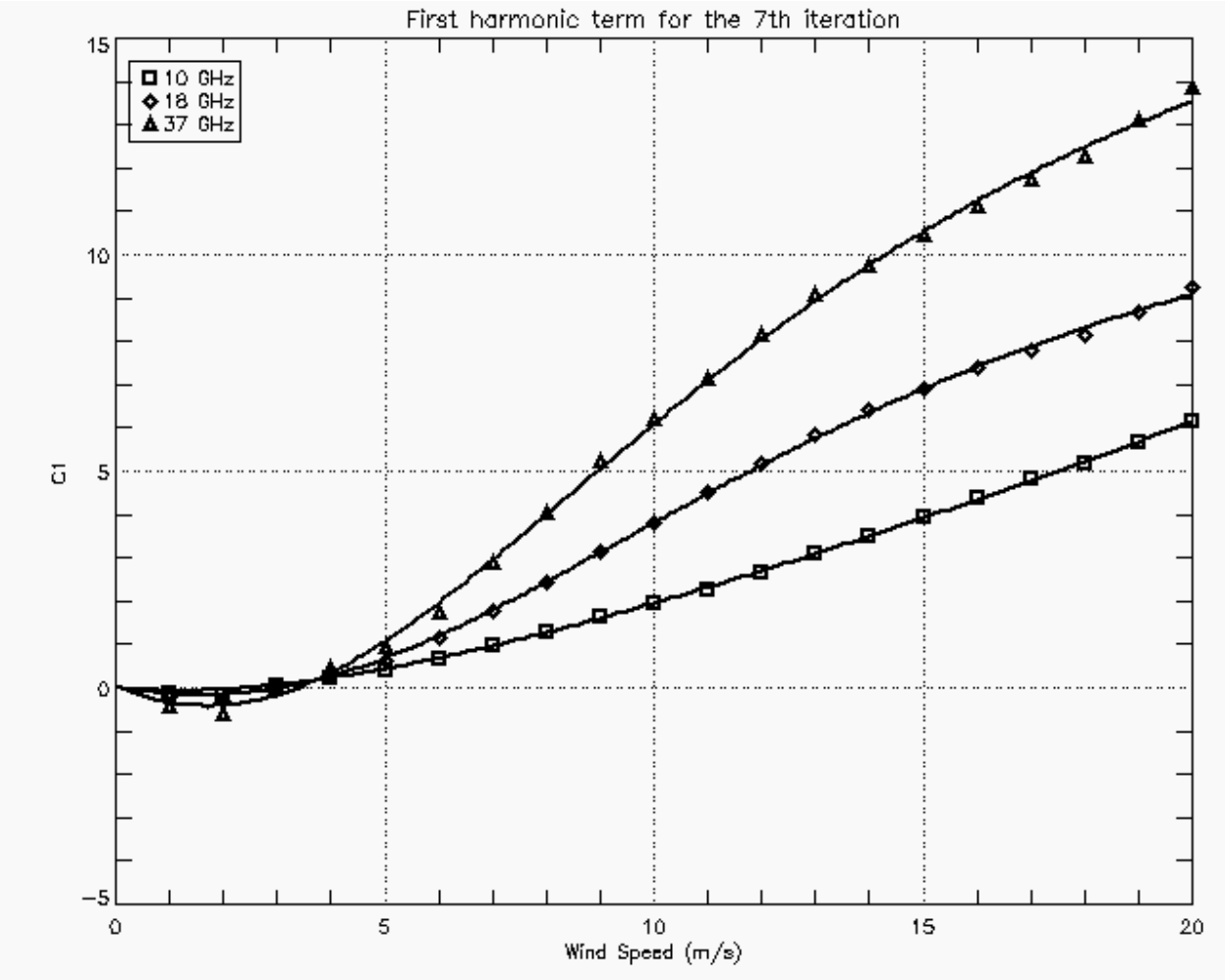

Figure 34: First harmonic wind direction dependent term, C_1.

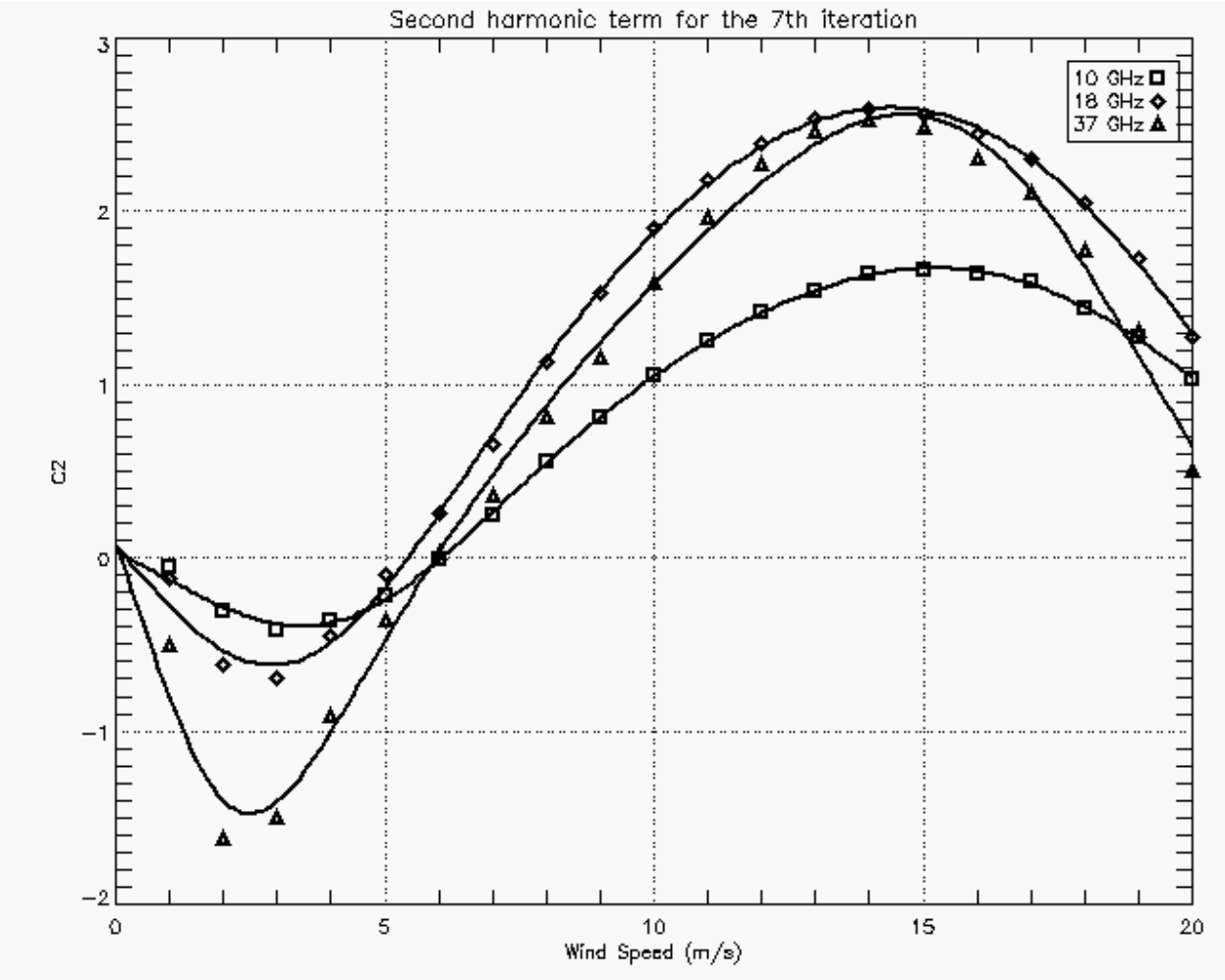

Figure 35: Second harmonic wind direction dependent term, C_2.

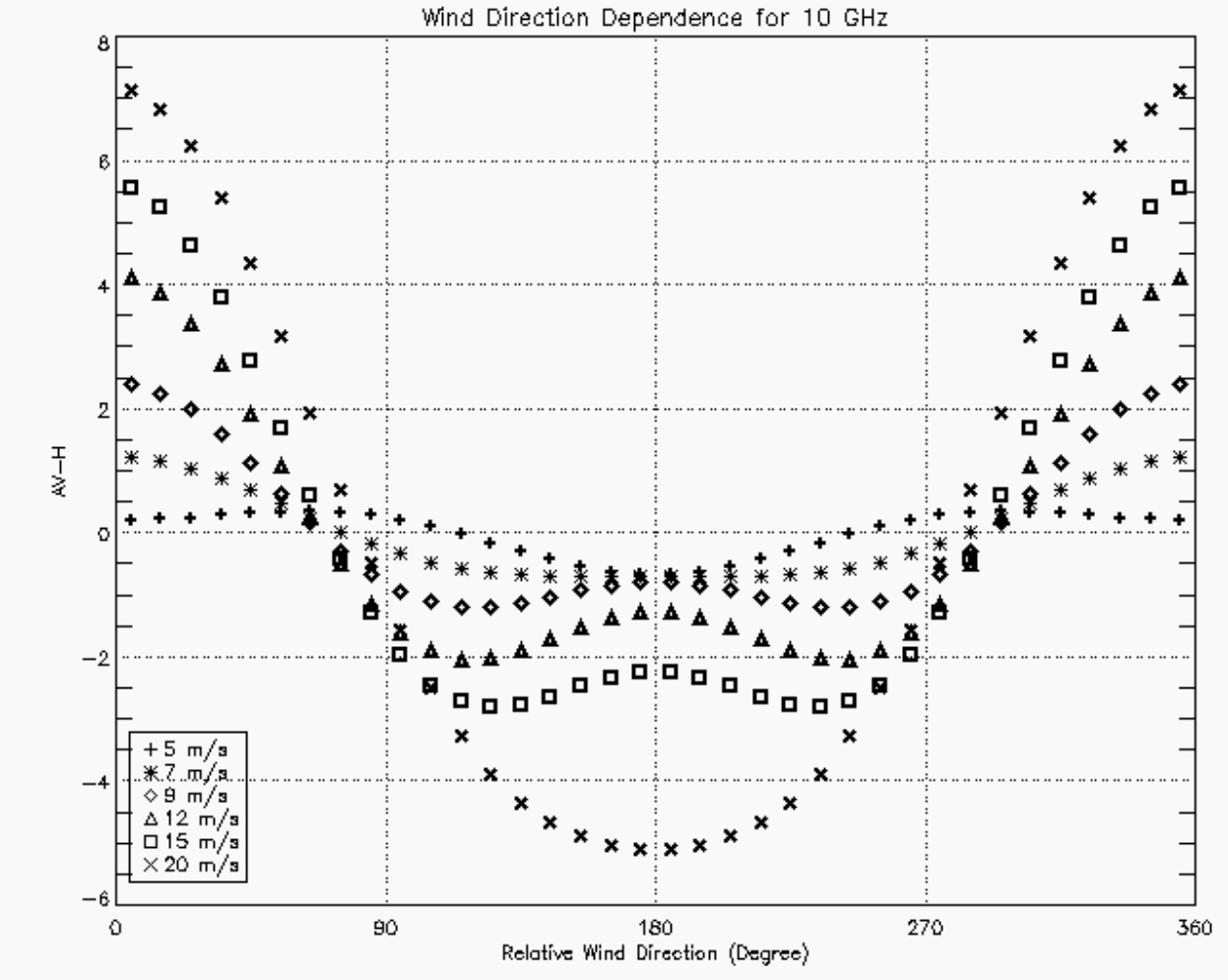

Figure 36: Wind vector model for 10 GHz (DC term removed).

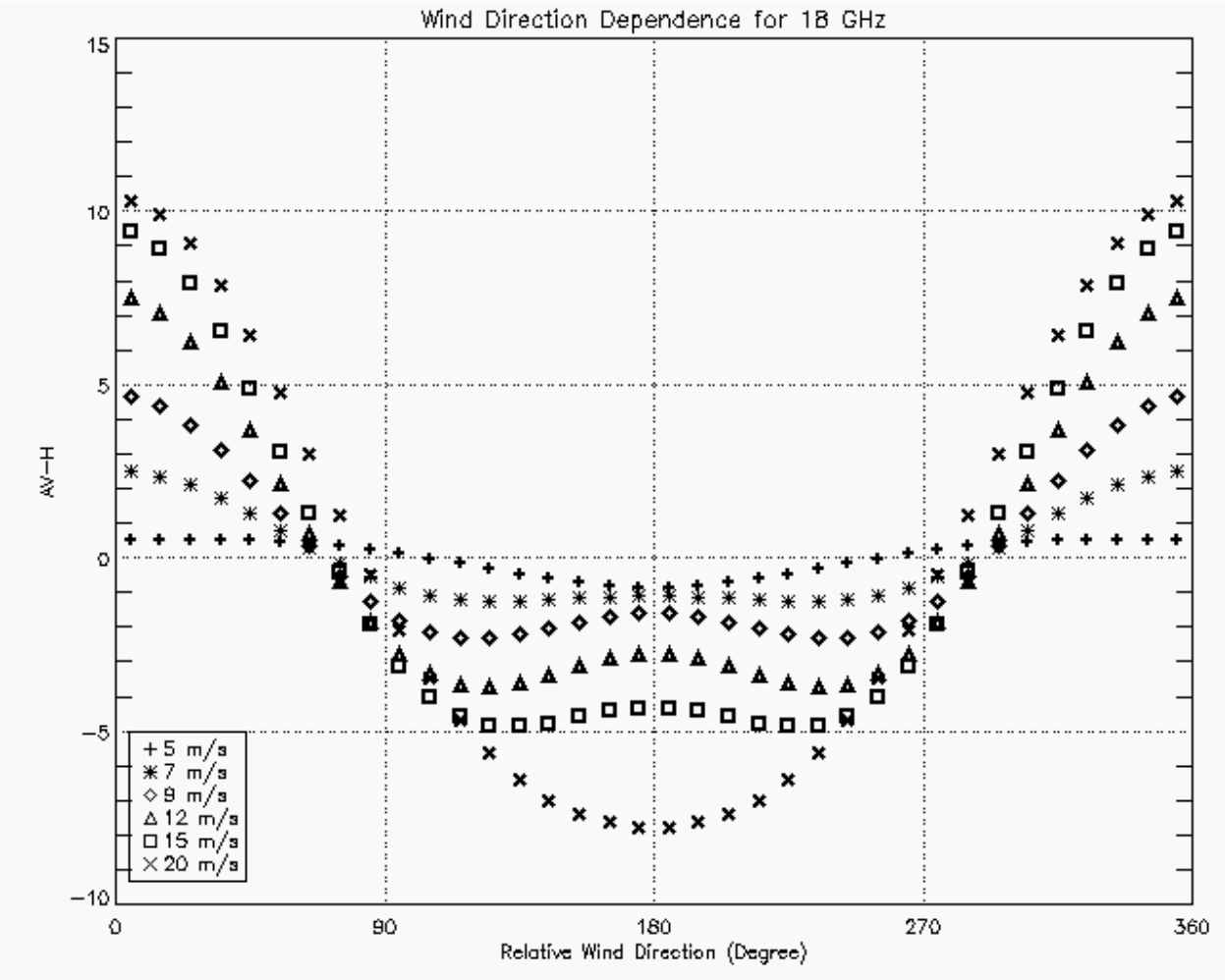

Figure 37: Wind vector model for 18 GHz (DC term removed).

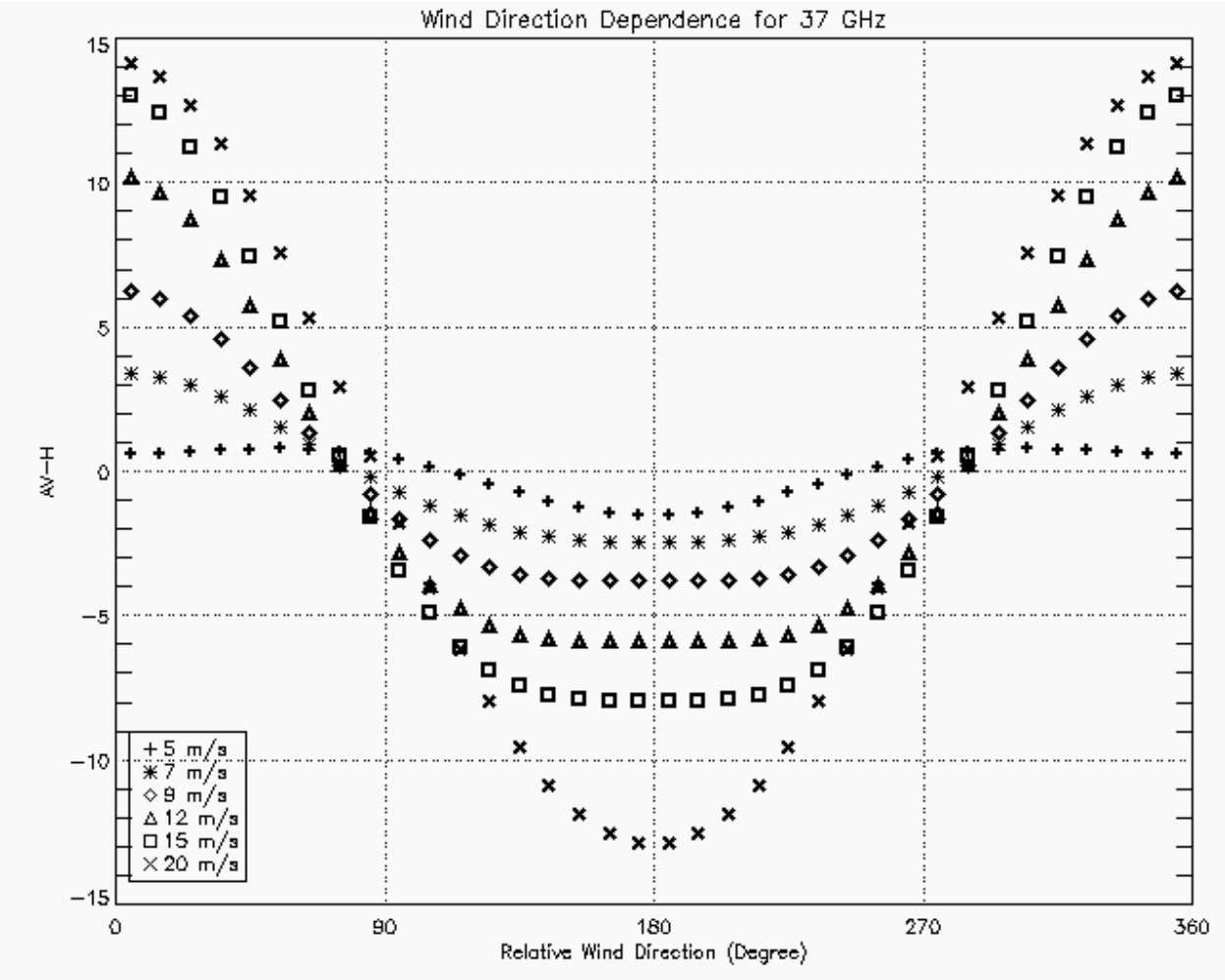

Figure 38: Wind vector model for 37 GHz (DC term removed).

***A*V-H GMF Validation**

Next, the model function was validated by comparison with independent measurements from the "withheld" test data set. As shown in Fig. 39, the individual *A*V-H measurements (minus *F(SST)* and C_0) for 10 GHz were plotted as a function of relative wind direction for wind speed 5 – 20 m/s. The dc values were subtracted from the *A*V-H measurements using the model C_0 coefficient and *F(SST)* dc terms and were compared with the GMF wind directional model (with the dc terms also removed) as indicate by the red solid line. Note that the GMF does a good job in representing the wind speed and wind direction dependence of *A*V-H; and the independent measurements scatter about the GMF. The amplitude of the wind directional signal grows with increasing wind speed whereas the measurement "geophysical" noise is relatively constant. This results in a reasonable signal to noise ratio for wind speeds > 9 m/s; however, for wind speed < 9 m/s, the wind directional signal to noise ratio is too small for reliable wind direction retrieval.

Similar plots are shown for 18 and 37 GHz channel in Fig. 40 – 41 respectively. For these channels, the wind directional signal amplitude becomes larger; however, in a similar manner, the measurement geophysical noise dominates for wind speeds < 9 m/s. For the 37 GHz channel, the geophysical noise is notably larger than the two lower frequencies. The most likely cause is the increased atmospheric sensitivity at 37 GHz to water vapor and cloud liquid that results in an increased non-cancelled atmospheric contribution.

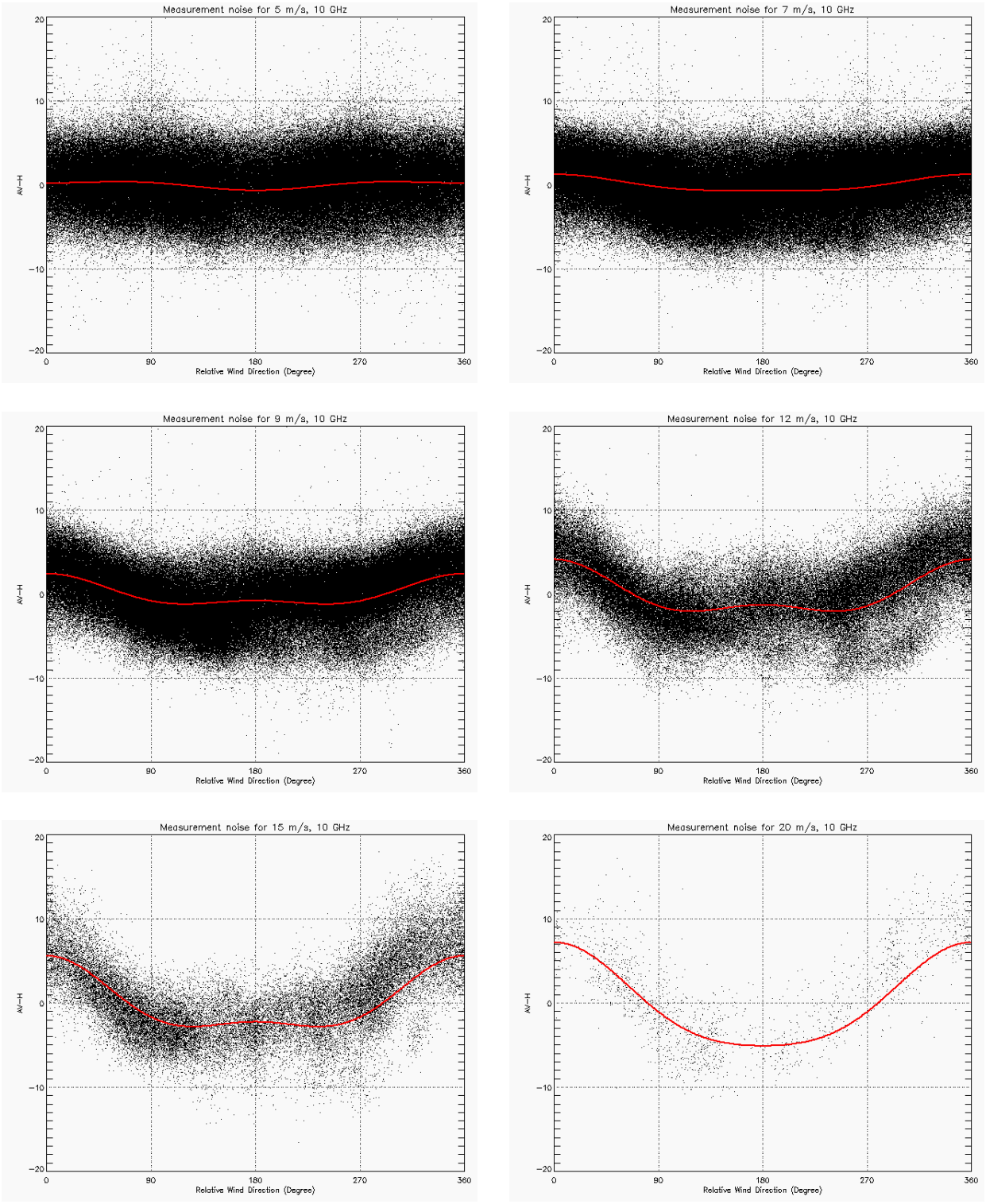

Figure 39: Independent *A*V-H measurement comparisons with GMF (red curve) for 10 GHz.

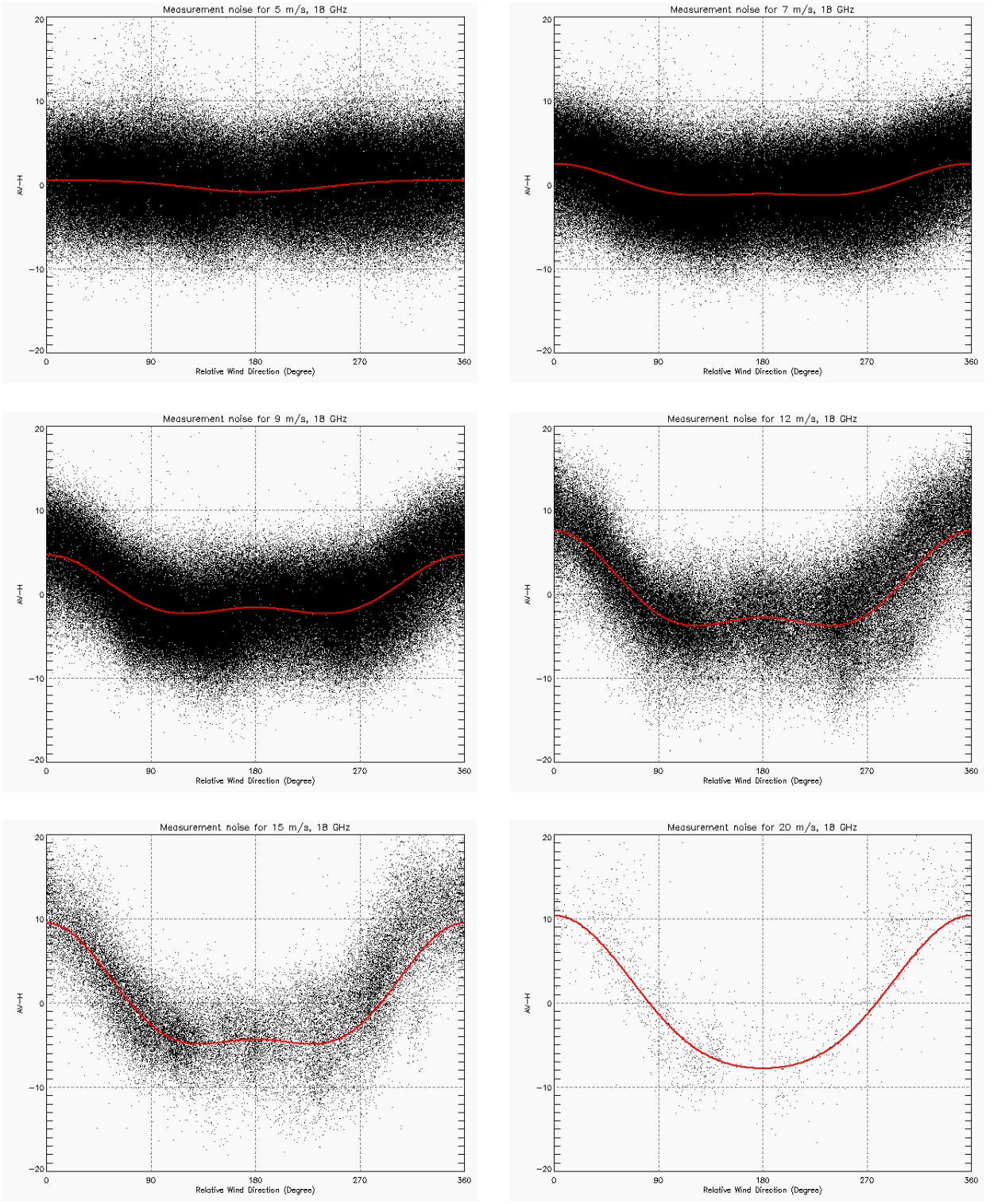

Figure 40: Independent *A*V-H measurement comparisons with GMF (red curve) for 18 GHz.

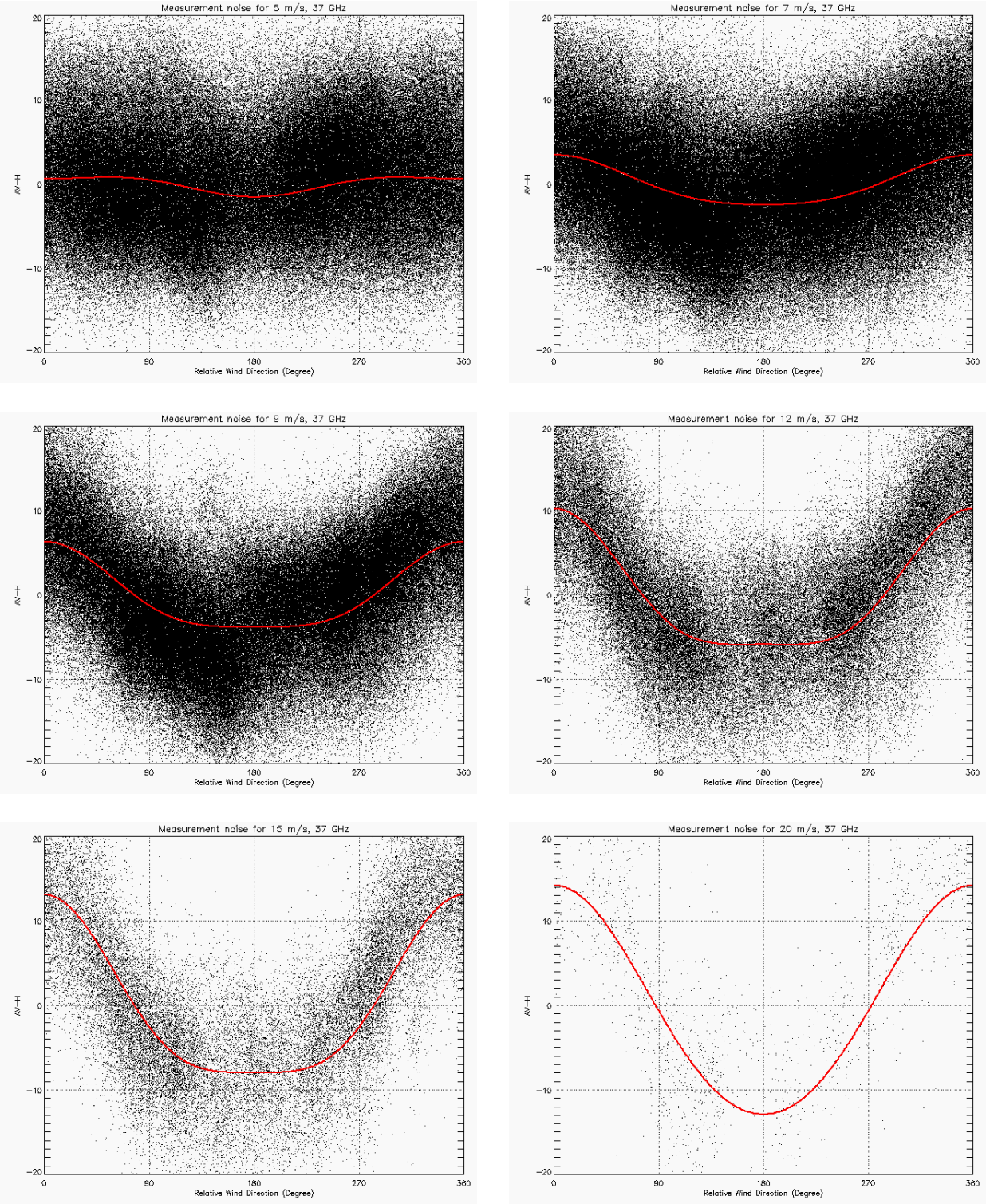

Figure 41: Independent *A*V-H measurement comparisons with GMF (red curve) for 37 GHz.

To evaluate the performance of the model function, the overall mean and root-mean-square (RMS) of errors (measured minus model) for wind speed ranges between 5 – 20 m/s were calculated and are given in Table 4 and Table 5 respectively. These results represent a quantitative analysis of the measurement-to-model goodness of fit for the three frequency channels shown in Fig. 39 – 41. The mean and standard deviation errors are also calculated for each relative wind direction of 10° bins as a function of frequencies and wind speeds. These results are found in Appendix C.

Table 4: GMF Validation: Mean Errors in Kelvin.

	10 GHz	***18 GHz***	***37 GHz***
5 m/s	0.105	0.394	0.627
7 m/s	-0.044	0.220	0.176
9 m/s	-0.016	0.057	-0.015
12 m/s	0.133	0.488	0.332
15 m/s	0.524	1.042	0.466
20 m/s	0.841	1.464	1.954

Table 5: GMF Validation: RMS Errors in Kelvin.

	10 GHz	***18 GHz***	***37 GHz***
5 m/s	3.020	3.663	6.555
7 m/s	2.834	3.454	6.115
9 m/s	2.838	3.535	6.056
12 m/s	3.276	4.065	6.586
15 m/s	3.415	4.341	6.598
20 m/s	3.653	5.002	8.508

CHAPTER FOUR: APPLICATION: WIND VECTOR RETRIEVAL

This chapter focuses on the remote sensing application of the passive *A*V-H model function previously developed of which the obvious use is wind vector retrieval. Given measured vertical and horizontal-pol brightness temperatures measurements and a-priori SST information, one can use the *A*V-H model function to retrieve wind speed and wind direction.

Traditionally, the ocean wind estimation algorithm used in microwave scatterometry is based on classical estimation theory. As describe by Chi and Li [27], they evaluated performance of several estimation algorithms and showed that all performed reasonably close to each other. A general form of the objective function of each algorithm used in wind estimation was expressed as [27]

$$J(wspd, wdir) = \sum_{N} \left| \frac{e_i}{\sigma_i} \right|^p + q \ln \sigma_i^{\,p} \tag{4.1}$$

where e_i = (measured σ^0 – model σ^0) for ith measurement

σ^2_i = variance of e_i

p = polarization 1 or 2 (V or H) and

q = 0 or 1 depending on the algorithm used

As described by Pak and Dunbar [21], the σ^0 residuals are normally distributed with the probability density of the ith measurement given by

$$P_i = \frac{1}{\sqrt{2\pi}\sigma_i^{\,2}} \exp\left(-\frac{1}{2} \frac{\left(\sigma^0{}_{i,meas} - \sigma^0{}_{i,\mathrm{mod}\,el}\right)^2}{\sigma_i^{\,2}} \right) \tag{4.2}$$

The likelihood function J from N measurements is a product of the individual measurements. The maximum likelihood estimator (MLE) objective function is then applied to

search for the wind vector solutions that maximize the joint probability of the residual measurements [21].

By taking a negative logarithm of the joint probability function, the MLE objective function becomes [21]

$$J = -\ln P = \frac{1}{2}\sum_{N}\left(\ln(2\pi\sigma_i) + \frac{\left(\sigma^0{}_{i,meas} - \sigma^0{}_{i,\mathrm{mod}\,el}\right)^2}{\sigma_i^{\,2}}\right) \tag{4.3}$$

As suggested by Pak and Dunbar [21], the negative logarithm does not affect the maximum/minimum of *J*. In addition, dropping off the constant term in the summation does not affect the properties of *J*, thus the objective function *J* reduces to [21]

$$J = \sum_{N}\frac{\left(\sigma^0{}_{i,meas} - \sigma^0{}_{i,\mathrm{mod}\,el}\right)^2}{\sigma_i^{\,2}} \tag{4.4}$$

This form of the objective function is also recognized as the weighted least squares (WLS) estimator. However, in scatterometry the objective function estimator that is used is usually referred to as the maximum likelihood estimator (MLE) according to its original usage.

Wind Retrieval Algorithm

As mentioned previously, one possible application of the *A*V-H model function developed in Chapter 3 is the wind vector retrieval. Since the GMF depends on both wind speed and wind direction, ultimately both of these parameters can be retrieved from the *A*V-H measurements. Unfortunately, for wind speeds < 9 m/s, the anisotropy of the brightness temperature is weak and lies within the measurement geophysical noise level. This poor signal to noise ratio makes it impractical to use only passive microwave measurements for the wind

direction retrievals over all wind speeds. The example of measurement noise of *A*V-H for the 18GHz channel and wind speed of 15m/s is repeated again in Fig. 42. As shown in this figure, the measurement brightness is normally distributed around the model function (solid line). Even though the wind directional signal increases for higher wind speeds, the measurement noise standard deviation is still high; so in order to use the model for wind retrievals, the variance of the measurement was empirically found for all wind speed and relative wind directions. The variance was modeled In Fig. 43. The standard deviation of the measurement is shown as a function of relative wind direction for 15 m/s. The variance was modeled the same way as the empirical model function of the *A*V-H measurement – as a function of both wind speed and relative wind direction. Knowing the measurements for each frequency channel, the wind vector retrieval can be achieved by using the principle of the maximum likelihood estimator (MLE). In Fig. 43 the standard deviation of the measurement is shown as a function of relative wind direction for 15 m/s.

As seen in Fig. 42, the model function peak-to-peak amplitude is large, for higher wind speed compared to the measurement noise, thus yielding higher signal to noise ratio. Considering lower wind speeds < 9 m/s, the wind directional signal is weaker and lies within the measurement noise standard deviation as shown by dash-lines in Fig. 44 for the upwind direction. Therefore, using the *A*V-H measurements alone in the wind vector retrieval algorithms would not be able to retrieve the wind vector with desired accuracies.

On the other hand, a wind scatterometer measures ocean radar backscatter that has a strong dependence on both wind speed and direction. The scatterometer wind measurement technique requires that a wind vector cell located on the ocean surface be observed from multiple azimuth directions (forward and aft looking) in order to unambiguously retrieve wind vector.

However, if it could be made to work, a single forward-look scatterometer would be a more favorable simpler configuration from a satellite instrument/accommodation standpoint.

In this dissertation approach, a combined measurement of *A*V-H brightness temperature and a fore-look sigma-0 from a scatterometer were used together to investigate the possibility of this new wind retrieval algorithm. Using the favorable active and passive instrument configuration on the ADEOS-II, brightness temperature measurements were obtained from the AMSR radiometer and the sigma-0 measurements were obtained from the SeaWinds scatterometer.

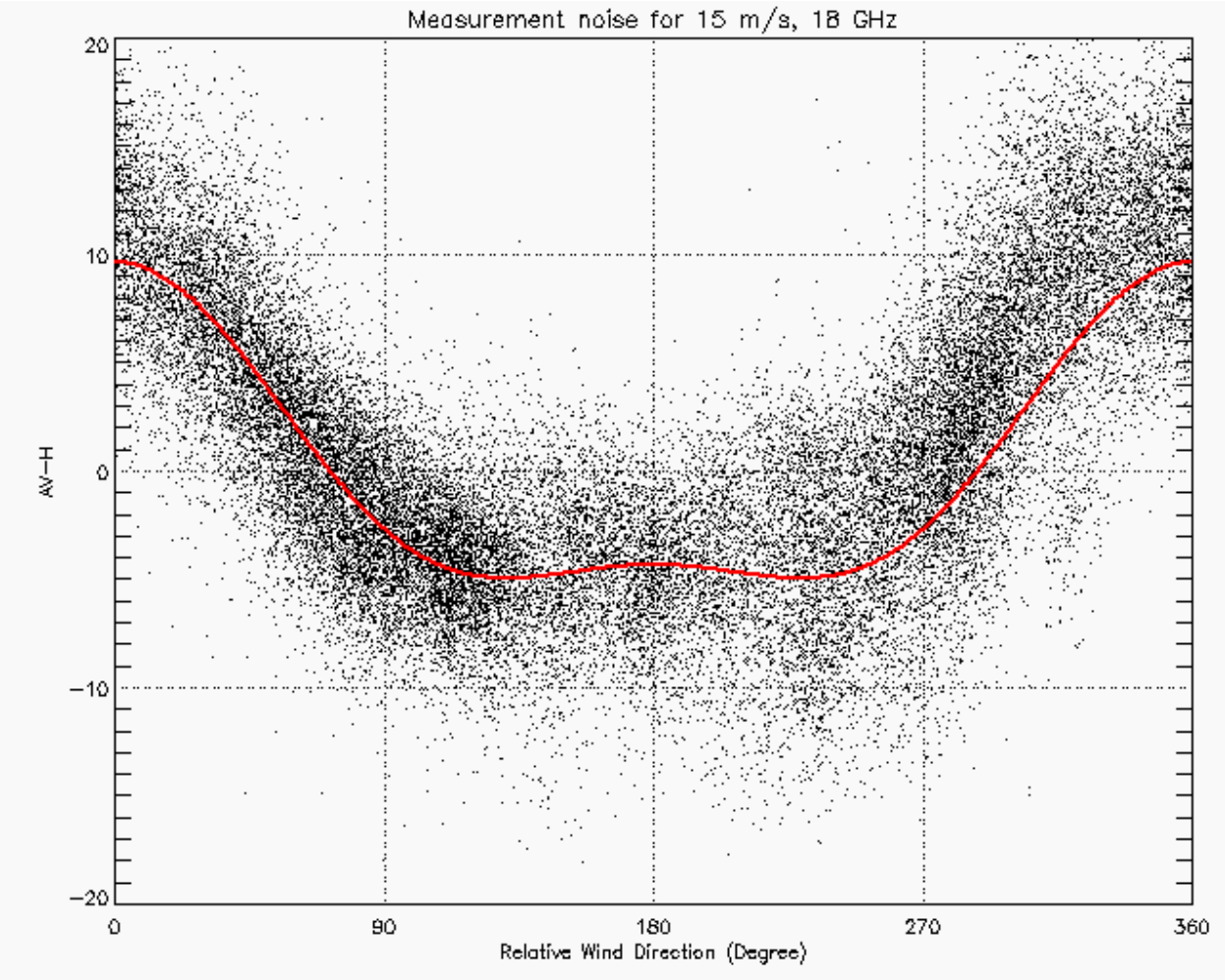

Figure 42: The *A*V-H measurement normally distributed about the model function.

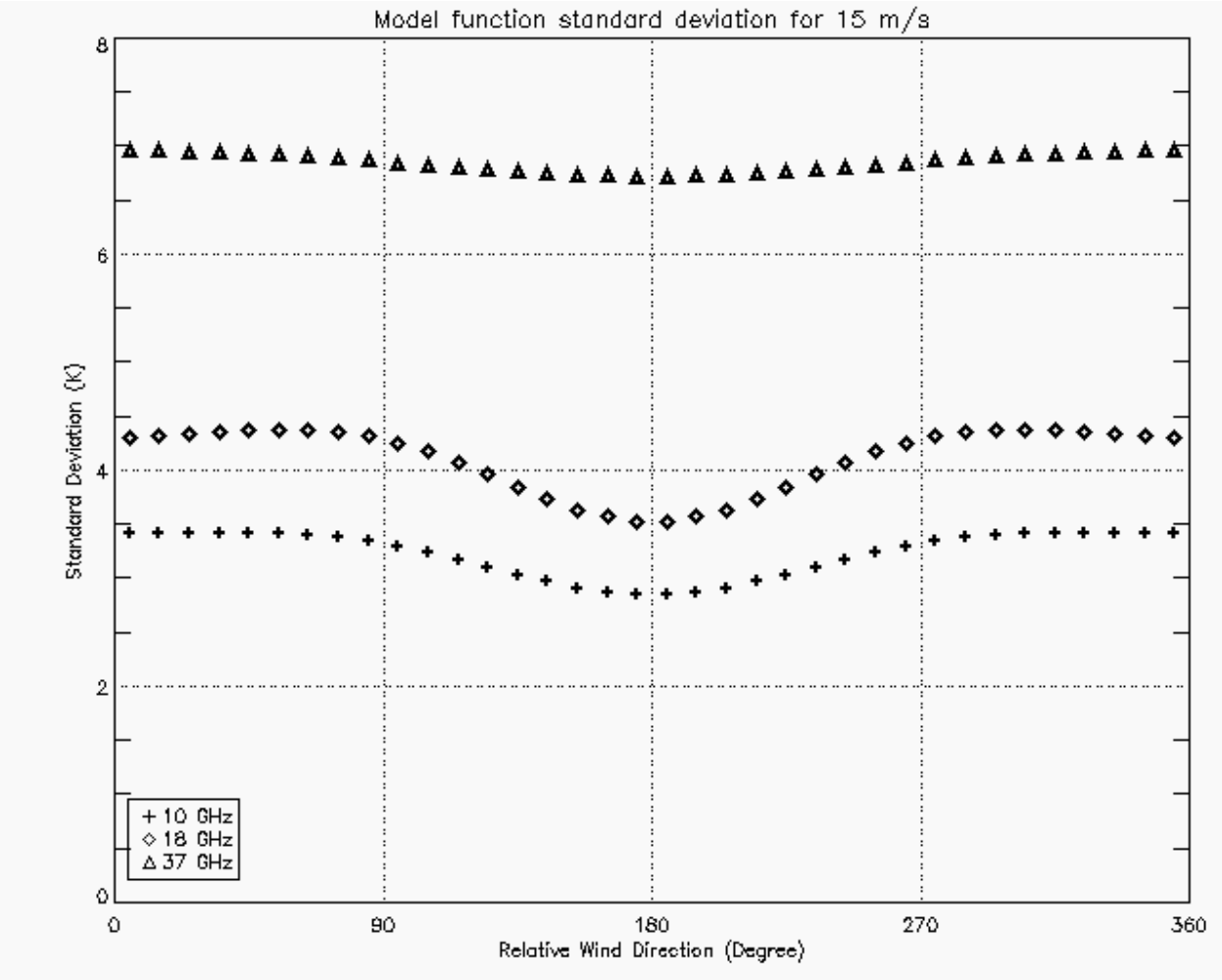

Figure 43: The measurement standard deviation.

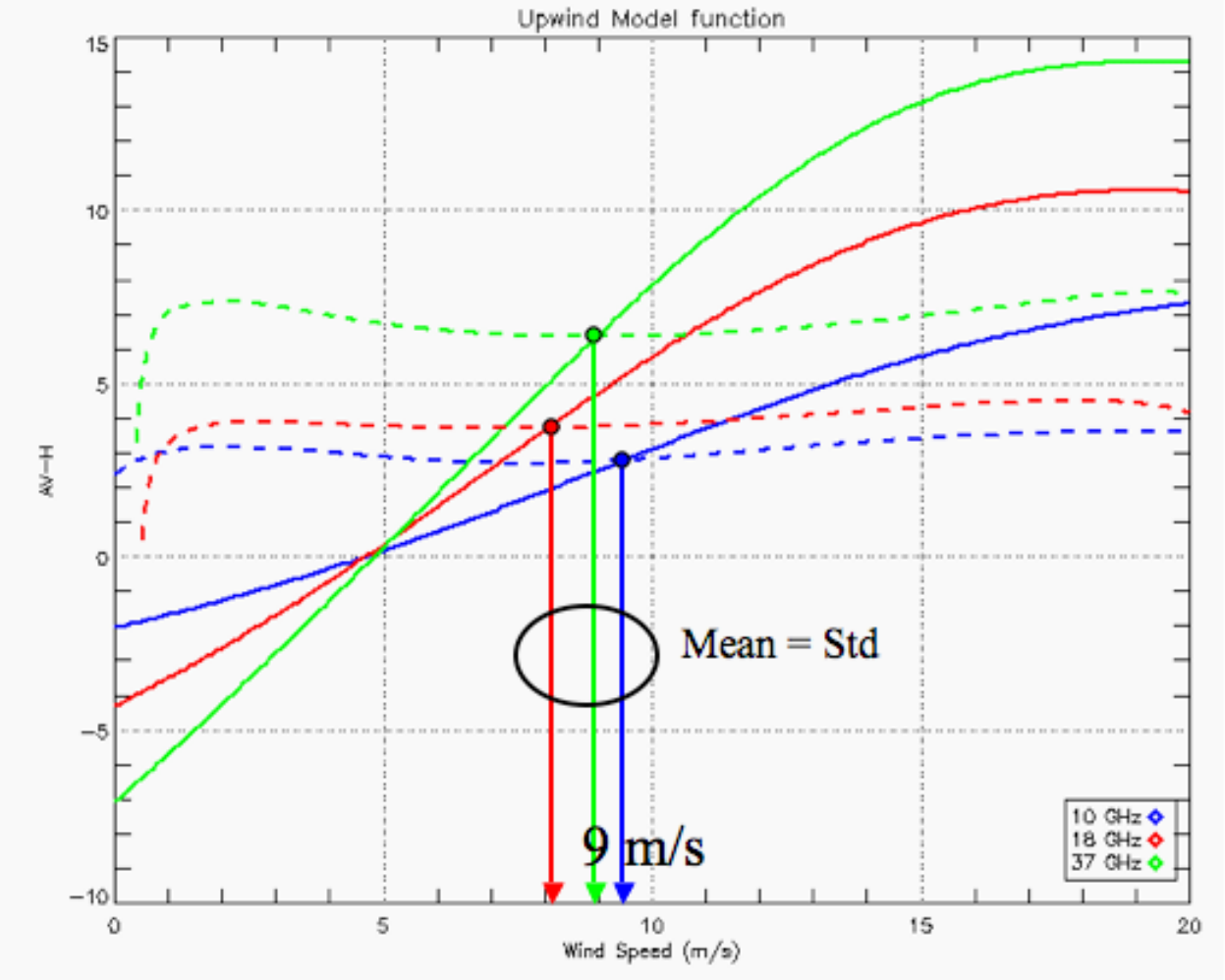

Figure 44: Upwind directional signal (solid) and the standard deviation (dash) for 10, 18 and 37 GHz channels.

To demonstrate the possibility of wind retrievals using this combined active/passive measurements, we assumed a-priori knowledge of wind speed and sea surface temperature, and only wind direction was retrieved. For this experiment, a priori wind speed was the AMSR retrieved wind speed (conventional product) and the SST was the GDAS standard product.

ADEOS-II combined active and passive measurements were used to perform wind direction retrievals. The fore-look active measurements were obtained from the SeaWinds fore-V pol and fore-H pol sigma-0's and the passive measurements were obtained from the AMSR *A*V-H brightness temperature using 10, 18 and 37 GHz frequency channels. In each of the wind vector cell (WVC) across the measurement swath, wind directions were retrieved by minimizing the objective function of the combined measurements as given in (4.5). Due to the biharmonic nature of both active and passive model functions and the noise from both backscatter and brightness temperature measurements, there were multiple wind direction solutions, or so-called ambiguities or aliases. The wind direction ambiguities correspond to the local minimum points of the objective function and they were ranked according to the inverse values of the objective function, i.e., the 1st ranked solution is the direction that gave the lowest minimum values in (4.5), the 2nd ranked solution is the second minimum, and so on.

$$J(wspd,wdir) = \sum_{freq=10,18,37GHz} \frac{\left(AVH_{Meas} - AVH_{Model}(wspd,rel.dir,SST)_{freq}\right)^2}{Variance_{AVH}(wspd,rel.dir)_{freq}} + \sum_{pol=V,H} \frac{\left(\sigma_0 - GMF(wspd,rel.dir)_{pol}\right)^2}{Variance_{\sigma_0}(wspd,rel.dir)_{pol}} \tag{4.5}$$

The first summation in (4.5) represents the normalized residual of the *A*V-H brightness temperature between the measured and the modeled signal. The squared-residual was normalized by the measurement variance. The second summation in (4.5) represents the residual between the

measured sigma-0 and the scatterometer GMF, where the squared-residual was normalized by their corresponding variance [28]. Given the wind speed, SST and the related geometry parameters, the wind direction solutions may be found by searching for the directions that correspond to the local minimum of the objective function. The multiple wind direction solutions were kept up to four possible values (ranked 1^{st} – 4^{th}). For example, as shown in Fig. 45, the normalized residuals were shown for three passive (10, 18, and 37 GHz) and two active (V and H-pol) measurements. The resulting three ambiguities shown correspond to the three local minima of (4.5).

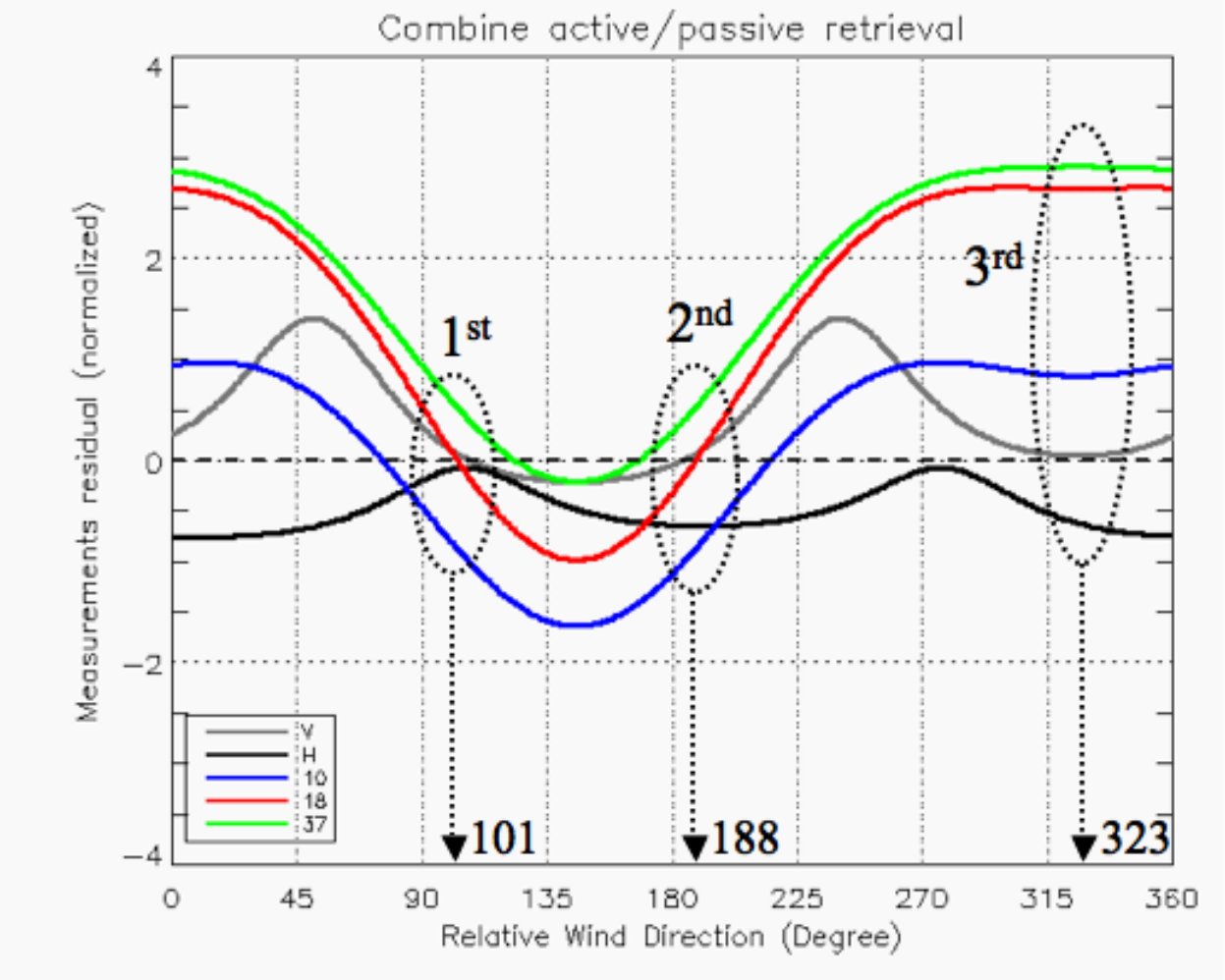

Figure 45: Weighted normalized residuals for MLE wind retrieval.

Comparisons

By using the withheld testing dataset, the combined active and passive wind direction retrievals were evaluated. For comparison purposes, an independent set of wind directions from the GDAS was used as surface truth to evaluate the performance of this algorithm. As the wind directions were kept up to four possible solutions, the solutions that are closest to the GDAS wind direction were selected. The corresponding selected solution rankings were also recorded so that the retrieval skill could be evaluated.

Scatter plots showing a comparison of the closest wind direction using the combined active/passive algorithm with the GDAS's values are given in Fig. 46 for some selected wind speeds. The resulting retrieval standard deviation errors are presented in Table 6 for wind speed range between 5 – 20 m/s. The standard deviations were calculated for the difference between the closest ambiguities wind direction retrieval using the combined active/passive algorithm and the GDAS surface truth. Note in Table 6, the active/passive algorithm when excluding the 37 GHz channel, which is known to be the most noisy due to the atmospheric sensitivity, has slightly improved standard deviation errors compared to using all three frequency channels together. A comparison is also shown for a traditional four-look scatterometer wind direction retrieval of the SeaWinds with the GDAS surface truth.

For higher wind speeds (> 9 m/s), in approximately 80 – 90% cases, with the active/passive algorithm, combined 1^{st} and 2^{nd} ranked ambiguities were the closest wind direction to the true GDAS wind direction as given in Table 7. This means that this algorithm using combined measurements represent relatively high retrieval skill. The probability of the 1^{st} and the 2^{nd} ranked ambiguities being the correct solution for these higher wind speeds are

therefore very similar to those of the wind ambiguities retrieved from the traditional multiple-look scatterometer measurements. Thus, it would be reasonable to apply a similar median filtering ambiguity removal algorithm for the ambiguities resulting from the combined active/passive algorithm [29, 30]. However, for low to moderate wind speed, the skill for the first two ranked ambiguities were lower and the probability of the 3rd ranked solutions being the correct solution increased. As compare to the traditional scatterometer measurement; although the combined retrieval algorithm present higher standard deviation errors (but within < 20° for wind speed > 9 m/s) and lower skill for lower wind speeds, the combined *A*V-H and fore-look sigma-0 measurements provide comparable accuracy to the current wind scatterometer for most of the wind speed range.

Further, the retrieval performance shown here was wind direction retrieval only; however, when wind speed and direction are retrieved simultaneously, the optimal wind speed and direction will be found to maximize the objective function. Thus, the resulting wind direction is expected to have improved standard deviation errors. These results are encouraging to show the potential of combining passive and single-look active microwave measurement into a common instrument, which could provide an attractive alternative choice for future ocean surface wind vector remote sensing.

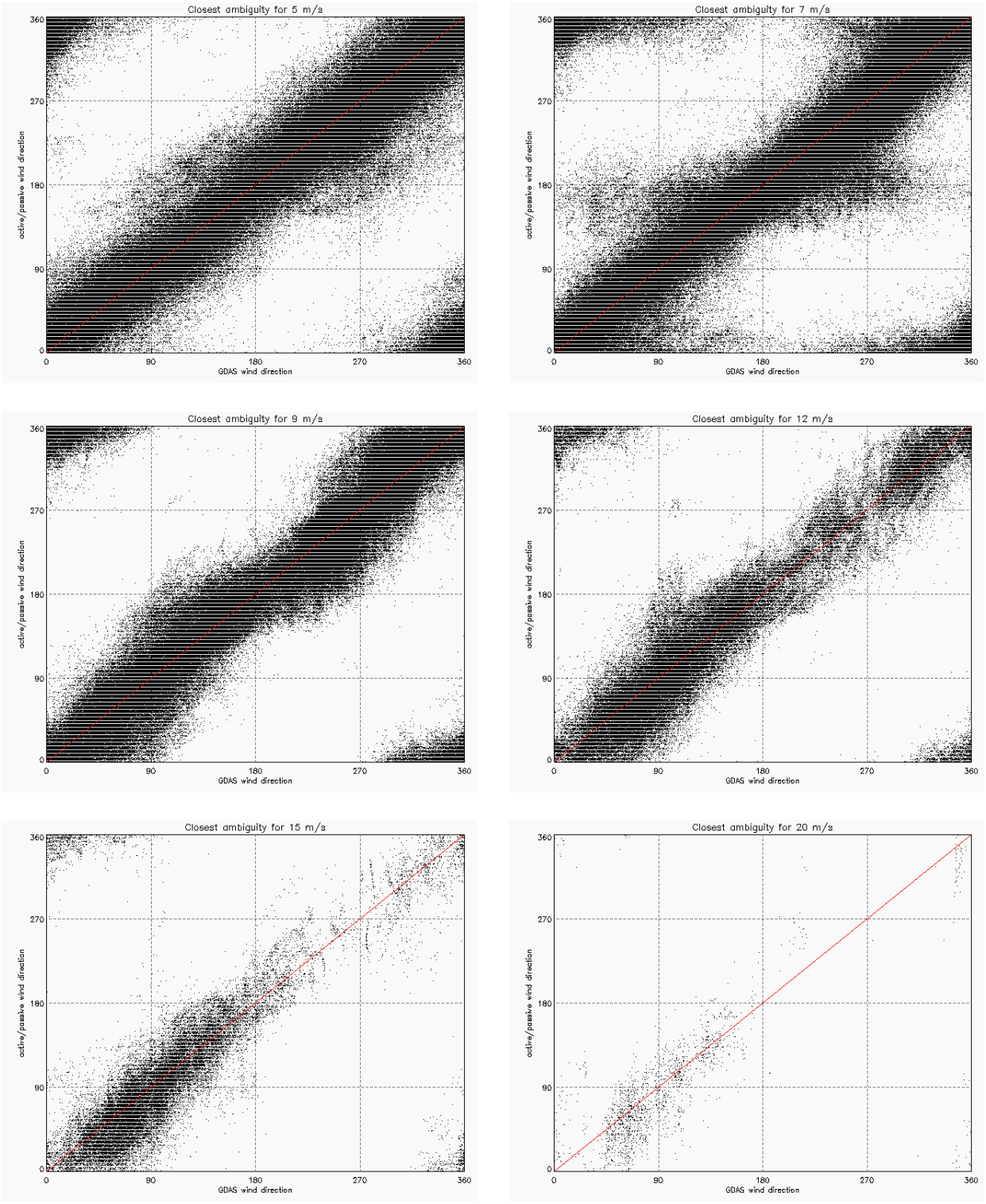

Figure 46: Closest retrieved direction comparison.

Table 6 Wind direction retrieval accuracy.

Wind Speed (meter/sec)	Number of Points	Standard Deviation Error (GDAS-retrieval)		
		Passive + fore-look Scat	Passive (exclude 37 GHz) + fore-look Scat	Scatterometer
5	337493	20.8°	19.0°	19.7°
7	441818	23.6°	20.4°	13.1°
9	309717	17.4°	16.8°	10.5°
12	99563	17.5°	16.9°	10.1°
15	33520	17.1°	16.9°	9.7°
20	1680	19.1°	18.5°	13.3°

Table 7 Wind direction retrieval skill.

Wind Speed (meter/sec)	Closest Ambiguity Ranking			
	1st	2nd	3rd	4th
5	30 %	35 %	23 %	13 %
7	30 %	34 %	23 %	13 %
9	30 %	37 %	27 %	6 %
12	61 %	28 %	10 %	1 %
15	82 %	15 %	2 %	1 %
20	91 %	9 %	0 %	0 %

CHAPTER FIVE: CONCLUSION AND DISCUSSION

A novel passive microwave ocean surface wind vector model function was developed for the AMSR radiometer on the ADEOS-II satellite. The model function relates the linear combination of the vertical and horizontal polarization brightness temperatures (AT_{BV}-T_{BH}) (measured at 10, 18 and 37 GHz) to the ocean surface wind vector and sea surface temperature (SST). The derivation of a linear coefficient *A* was presented as a function of measured brightness temperatures and the sea surface temperature. This brightness temperature combination has shown that it can significantly reduce the sensitivity to the atmosphere and therefore is more suitable for surface retrievals such as vector wind than conventional vertical and horizontal polarizations. The wind directional model function coefficients were derived for each of the channels of the AT_{BV}-T_{BH}, which was modeled as a three-term Fourier series with respect to relative wind direction.

Using this modeled linear combination of brightness temperature measurements alone may not contain sufficient information for retrieval of full ocean surface wind vector to the required accuracy, however, when used together with a scatterometer sigma-0 measurement, the wind direction retrievals are possible. Using the radar backscatter measurement from the collocated SeaWinds scatterometer, only the fore-look sigma-0 measurements were combined with the *A*V-H brightness temperatures from the AMSR. With the *A*V-H model function and the scatterometer GMF, for the first time, wind direction retrievals are possible using only fore-look measurements.

A demonstration of the wind direction only retrieval using single-look combined active/passive measurements showed that this technique could achieve required accuracy of <

20°, which is comparable performance to a traditional multi-look (forward and aft) scatterometer. This new wind retrieval technique demonstrates one of the applications of the passive model function developed for AMSR. With this model, an alternative, or option, for future satellite missions using only fore-look combined active/passive measurements may provide for relatively simple and cost effective instrument designs for wind vector retrieval. In addition, other geophysical information for the atmosphere and surface may be simultaneously retrieved as well.

For future research, there are several possible improvements for the passive model function development. First, the *A* parameter was derived as a function of the effective temperature T_{eff}; which was assumed constant air/sea temperature and equal to the sea surface temperature (SST). To the degree that this assumption is not met, there is uncertainty in the *A* value, which causes the atmosphere not to be significantly cancelled. Secondly, another uncertainty in the *A* parameter is that the *A* was defined as the ratio of the ocean polarized surface reflectivity. In this dissertation, only the SST and wind speed were taken into account; however, there are other parameters that can modify the surface reflectivity such as braking ocean waves and sea foam which could effect the *A* parameter. Finally, further study is necessary to characterize the effect of incidence angle variation in the satellite observation. As a result the *A*V-H combination would be affected by these uncertainties in the *A* parameter.

Also, further research is needed in the active/passive wind vector retrieval algorithm development. The present research performed only limited wind direction retrievals using the active/passive technique. The future work should optimize the active/passive retrieval algorithm for both wind speeds and wind directions that maximize the objective function. Also future work should develop a practical ambiguity removal algorithm that could achieve similar skill as current multi-look scatterometer techniques.

Finally, instrument trade studies and simulations should be conducted to explore the possibilities of future active/passive satellite instruments for ocean/atmosphere geophysical parameter remote sensing.

APPENDIX A: DATA PRODUCT CONTENT

AMSR overlay level 2A

Variable Name	Size/Dimension
ROW_NUMBER	Double Array [1702]
NUM_SIGMA0_PER_CELL	Double Array [80, 1702]
NUM_WVC_AMSR_TB	Double Array [12, 80, 1702]
MEAN_WVC_AMSR_TB	Double Array [12, 80, 1702]
STD_DEV_EVC_AMSR_TB	Double Array [12, 80, 1702]
LAT	Double Array [4, 80, 1702]
LON	Double Array [4, 80, 1702]
AMSR_ATM_ATTN	Double Array [4, 80, 1702]
AMSR_ATM_BACKSCATTER	Double Array [4, 80, 1702]
AMSR_ATM_ATTN_UNCERT	Double Array [4, 80, 1702]
AMSR_ATM_BACKSCATTER_UNCERT	Double Array [4, 80, 1702]
ABSORPTION_COEF_PER_METER	Double Array [4, 80, 1702]
WVC_QUAD_RAIN_INDICATOR	Double Array [4, 80, 1702]
WVC_QUAD_QUAL_FLAG	Double Array [4, 80, 1702]
AMSR_TB_RES_QUAL_FLAG	Double Array [4, 80, 1702]
AMSR_SST	Double Array [4, 80, 1702]
AMSR_WIND_SPEED	Double Array [4, 80, 1702]
AMSR_WATER_VAPOR	Double Array [4, 80, 1702]
AMSR_LIQUID	Double Array [4, 80, 1702]
AMSR_GRAUPEL	Double Array [4, 80, 1702]
AMSR_SNOW	Double Array [4, 80, 1702]
AMSR_RAIN_RATE	Double Array [4, 80, 1702]
AMSR_TB_OBS	Double Array [12, 4, 80, 1702]
AMSR_TB_18GHZ_RES	Double Array [6, 4, 80, 1702]

SeaWinds' science data level 2A

Variable Name	Size/Dimension
LON	Float Array [810, 1702]
LAT	Float Array [810, 1702]
AZIMUTH	Float Array [810, 1702]
EIA	Float Array [810, 1702]
SIGMA0	Float Array [810, 1702]
KPA	Float Array [810, 1702]
KPB	Float Array [810, 1702]
KPG	Float Array [810, 1702]
QUAL_FLAG	Float Array [810, 1702]
MODE_FLAG	Float Array [810, 1702]
CELL	Float Array [810, 1702]

Seawinds' science data level 2B

Variable Name	Size/Dimension
WVC_ROW	Double Array [1624]
WVC_LAT	Double Array [76, 1624]
WVC_LON	Double Array [76, 1624]
WVC_INDEX	Double Array [76, 1624]
NUM_IN_FORE	Double Array [76, 1624]
NUM_IN_AFT	Double Array [76, 1624]
WVC_QUALITY_FLAG	Double Array [76, 1624]
ATTEN_CORR	Double Array [76, 1624]
MODEL_SPEED	Double Array [76, 1624]
MODEL_DIR	Double Array [76, 1624]
NUM_AMBIGS	Double Array [76, 1624]
WIND_SPEED	Double Array [4, 76, 1624]
WIND_DIR	Double Array [4, 76, 1624]
WIND_SPEED_ERR	Double Array [4, 76, 1624]
WIND_DIR_ERR	Double Array [4, 76, 1624]
MAX_LIKELIHOOD_EST	Double Array [4, 76, 1624]
WVC_SELECTION	Double Array [76, 1624]
WIND_SPEED_SELECTION	Double Array [76, 1624]
WIND_DIR_SELECTION	Double Array [76, 1624]
MP_RAIN_PROBABILITY	Double Array [76, 1624]
NOF_RAIN_INDEX	Double Array [76, 1624]
AMSR_RAIN_INDICATOR	Double Array [76, 1624]
SRAD_RAIN_RATE	Double Array [76, 1624]

NOAA/NESDIS' GDAS data

Variable Name	Size
RECNUM	Long
TDIFF_JDSECS	Double
PRESS_SURF	Double
TEMP_SURF	Double
TEMP_2M	Double
TPW_COL	Double
CLW_COL	Double
ICE	Double
LAND	Integer
WIND_MAG_SURF	Double
WIND_DIR_SURF	Double

APPENDIX B: IDL ROUTINE

AMSR azimuth calculation

```
FUNCTION rel_az
R = 940; AMSR scan radius in km
wvc = FINDGEN(160)+1. ;cell number 1-160
arg = (wvc-80.5)*12.5/R
agt1 = WHERE(ABS(arg) GT 1.0)
ale1 = WHERE(ABS(arg) LE 1.0)
a = FLTARR(N_ELEMENTS(arg))
a(agt1) = !VALUES.F_NAN
a(ale1) = ASIN(arg[ale1])/!DTOR
RETURN, a
END

FUNCTION flightang
wi = FINDGEN(3404) + 0.5 ;WVC row center
u = wi*(360./3404.) - 90. ;argument of latitude at each WVC row
measured from equator crossing
cosu = COS(!DTOR*u) ;cos(arg.lat)
inc = 98.71*!DTOR ;orbit inclination
tani = TAN(inc)
arg = 1./(cosu*tani) ;tan(inclination)
ang = ATAN(arg)/!dtor ;flight angle in degrees relative to north
FOR i=1702,3403 DO ang(i) = -(180. - ang(i)) ;descending portion
needs to be flipped
RETURN,ang
END


PRO amsr_l2a_azimuth_get,azimu
az = FLTARR(160,3404)
```

```
f = flightang()
a = rel_az()
FOR i=0,3404-1 DO az[*,i]=REPLICATE(f(i),160,1)+a
az4 = FINDGEN(4,80,1702)
FOR i=0,1702-1 DO az4[0,*,i]=az[FINDGEN(80)*2,i*2+1] ;fore-left
FOR i=0,1702-1 DO az4[1,*,i]=az[FINDGEN(80)*2+1,i*2+1] ;fore-
right
FOR i=0,1702-1 DO az4[2,*,i]=az[FINDGEN(80)*2,i*2] ;aft-left
FOR i=0,1702-1 DO az4[3,*,i]=az[FINDGEN(80)*2+1,i*2] ;aft-right
az4f = FINITE(az4)
idazf = WHERE(az4f EQ 1)
;Convert azimuth to 0-360 deg range
i_lt0 = WHERE(az4(idazf) LT 0.0,ct0)
IF (ct0 GT 0) THEN az4(idazf(i_lt0)) = az4(idazf(i_lt0))+360.0
i_ge360 = WHERE(az4(idazf) GE 360.0,ct360)
IF (ct360 GT 0) THEN az4(idazf(i_ge360)) = az4(idazf(i_ge360)) -
360.0
azimu = az4
END
```

APPENDIX C: MODEL FUNCTION EVALUATION

10 GHz

Mean Errors in degree Kelvin.

	5 °	***15 °***	***25 °***	***35 °***	***45 °***	***55 °***	***65 °***	***75 °***	***85 °***
5 m/s	0.308	0.378	0.159	0.041	-0.039	-0.169	-0.211	-0.083	0.085
7 m/s	0.423	0.263	0.155	0.160	0.143	-0.105	-0.246	-0.379	-0.484
9 m/s	0.546	0.355	0.176	0.180	0.083	0.010	-0.197	-0.416	-0.442
12 m/s	0.823	0.493	0.267	0.187	-0.147	-0.541	-0.670	-0.840	-1.029
15 m/s	1.135	0.225	-0.117	-0.259	-0.685	-0.928	-1.196	-1.119	-1.031
20 m/s	-0.270	0.103	0.619	-0.354	0.370	0.705	0.422	0.685	-1.009
	95 °	***105 °***	***115 °***	***125 °***	***135 °***	***145 °***	***155 °***	***165 °***	***175 °***
5 m/s	0.108	-0.051	-0.179	-0.325	-0.395	-0.249	-0.086	0.090	0.192
7 m/s	-0.512	-0.590	-0.707	-0.831	-0.860	-0.903	-0.801	-0.500	-0.344
9 m/s	-0.501	-0.601	-0.735	-0.876	-1.276	-1.392	-1.375	-1.070	-0.504
12 m/s	-0.869	-0.561	-0.517	-0.572	-0.666	-0.865	-0.625	-0.412	-0.242
15 m/s	-0.701	-0.494	-0.465	-0.397	-0.359	-0.502	-0.242	-0.227	-0.927
20 m/s	-0.310	-1.325	-0.978	-1.077	-0.154	-0.246	1.198	1.630	0.805
	185 °	***195 °***	***205 °***	***215 °***	***225 °***	***235 °***	***245 °***	***255 °***	***265 °***
5 m/s	0.194	0.178	0.126	0.154	0.289	0.393	0.479	0.549	0.364
7 m/s	-0.179	0.064	0.194	0.289	0.252	0.280	0.377	0.481	0.347
9 m/s	-0.184	-0.003	0.239	0.419	0.524	0.661	0.604	0.614	0.616
12 m/s	-0.388	-0.296	0.154	0.324	0.755	0.779	0.456	0.651	1.160
15 m/s	-0.795	0.223	0.574	1.050	1.031	0.730	0.992	1.588	2.064
20 m/s	0.722	-0.739	0.672	1.282	1.717	1.207	2.768	2.582	3.402
	275 °	***285 °***	***295 °***	***305 °***	***315 °***	***325 °***	***335 °***	***345 °***	***355 °***
5 m/s	0.394	0.316	0.064	-0.087	-0.017	0.119	0.306	0.301	0.389
7 m/s	0.479	0.478	0.319	0.305	0.237	0.251	0.402	0.414	0.508
9 m/s	0.559	0.714	0.741	0.802	0.638	0.629	0.718	0.633	0.622
12 m/s	1.372	1.082	0.530	0.407	0.788	0.987	1.059	1.137	0.955
15 m/s	1.929	2.199	2.667	3.271	2.387	2.110	1.874	1.521	1.553
20 m/s	2.937	3.815	3.421	3.245	3.142	2.621	3.147	2.127	1.682

RMS Errors in degree Kelvin.

	5 °	***15 °***	***25 °***	***35 °***	***45 °***	***55 °***	***65 °***	***75 °***	***85 °***
5 m/s	2.942	2.832	2.774	2.727	2.887	2.805	2.934	2.968	3.007
7 m/s	2.792	2.729	2.616	2.496	2.530	2.729	2.591	2.622	2.666
9 m/s	2.750	2.717	2.649	2.467	2.562	2.422	2.414	2.495	2.541
12 m/s	2.964	2.797	2.764	2.689	2.696	2.657	2.539	2.686	3.095
15 m/s	3.304	3.088	2.970	2.882	2.804	2.679	2.620	2.544	2.411
20 m/s	3.180	2.891	2.572	3.404	2.896	3.553	3.185	3.823	3.236
	95 °	***105 °***	***115 °***	***125 °***	***135 °***	***145 °***	***155 °***	***165 °***	***175 °***
5 m/s	3.130	3.027	3.005	3.021	3.055	3.136	3.090	3.054	2.999
7 m/s	2.689	2.765	2.737	2.776	2.864	2.942	3.063	3.054	2.941
9 m/s	2.451	2.446	2.517	2.659	2.736	2.822	2.900	2.925	3.013
12 m/s	2.700	2.591	2.745	2.731	2.721	2.788	2.947	2.913	3.230
15 m/s	2.477	2.419	2.240	2.570	2.905	3.282	2.894	2.803	2.734
20 m/s	3.579	3.430	3.933	2.541	2.649	2.922	4.150	2.949	2.948
	185 °	***195 °***	***205 °***	***215 °***	***225 °***	***235 °***	***245 °***	***255 °***	***265 °***
5 m/s	3.205	3.196	3.075	3.063	3.060	2.926	2.955	3.010	3.254
7 m/s	2.961	2.927	2.789	2.727	2.770	2.776	2.765	2.868	2.956
9 m/s	2.966	3.088	2.822	2.779	2.927	2.893	2.879	2.695	2.867
12 m/s	3.426	3.732	3.202	2.955	3.232	3.172	3.309	3.668	3.656
15 m/s	2.792	2.730	2.616	3.245	3.108	3.238	3.253	3.515	3.982
20 m/s	2.959	2.182	3.025	3.712	2.762	2.566	2.973	3.063	3.647
	275 °	***285 °***	***295 °***	***305 °***	***315 °***	***325 °***	***335 °***	***345 °***	***355 °***
5 m/s	3.070	3.084	2.978	3.053	3.017	2.999	3.043	2.933	2.881
7 m/s	2.768	2.647	2.772	2.823	2.933	2.977	2.982	2.929	2.896
9 m/s	2.892	2.841	2.764	2.852	2.933	2.965	2.940	2.869	2.854
12 m/s	3.677	4.223	4.079	4.231	3.834	3.664	3.240	3.047	3.184
15 m/s	3.614	3.613	3.683	3.293	4.098	4.126	3.304	3.251	3.341
20 m/s	2.422	3.505	2.959	3.867	4.467	3.979	2.187	3.070	2.648

18 GHz

Mean Errors in degree Kelvin.

	5 °	***15 °***	***25 °***	***35 °***	***45 °***	***55 °***	***65 °***	***75 °***	***85 °***
5 m/s	0.559	0.694	0.488	0.382	0.286	0.145	0.096	0.196	0.384
7 m/s	0.773	0.578	0.417	0.485	0.428	0.101	-0.038	-0.142	-0.033
9 m/s	0.919	0.766	0.593	0.532	0.360	0.145	-0.243	-0.363	-0.264
12 m/s	1.391	0.883	0.699	0.670	0.321	-0.134	-0.329	-0.383	-0.609
15 m/s	1.217	0.177	0.153	0.212	0.129	-0.289	-0.485	-0.402	-0.061
20 m/s	-0.720	-0.459	1.645	1.428	1.697	3.437	2.500	2.918	-0.365
	95 °	***105 °***	***115 °***	***125 °***	***135 °***	***145 °***	***155 °***	***165 °***	***175 °***
5 m/s	0.472	0.257	0.067	-0.082	-0.087	0.097	0.291	0.546	0.665
7 m/s	0.006	-0.046	-0.269	-0.427	-0.504	-0.549	-0.412	-0.071	0.125
9 m/s	-0.135	-0.206	-0.492	-0.628	-0.987	-1.124	-1.197	-0.924	-0.446
12 m/s	-0.305	0.127	0.103	-0.060	-0.175	-0.349	0.010	0.079	0.012
15 m/s	0.228	0.245	0.346	0.197	0.446	0.071	0.365	0.641	-0.349
20 m/s	-0.089	-1.866	-1.006	-0.863	1.075	1.280	3.030	3.240	1.629
	185 °	***195 °***	***205 °***	***215 °***	***225 °***	***235 °***	***245 °***	***255 °***	***265 °***
5 m/s	0.634	0.639	0.582	0.572	0.612	0.693	0.824	0.835	0.579
7 m/s	0.176	0.297	0.459	0.528	0.501	0.566	0.738	0.819	0.623
9 m/s	-0.085	0.168	0.368	0.568	0.750	0.881	0.739	0.632	0.546
12 m/s	-0.246	-0.223	-0.004	0.265	0.849	0.953	0.553	0.820	1.496
15 m/s	-0.458	0.213	0.263	0.624	0.954	0.549	0.969	1.711	2.482
20 m/s	2.088	-1.229	0.685	1.259	0.958	0.200	1.826	2.766	2.826
	275 °	***285 °***	***295 °***	***305 °***	***315 °***	***325 °***	***335 °***	***345 °***	***355 °***
5 m/s	0.488	0.329	0.163	0.033	0.112	0.314	0.564	0.545	0.612
7 m/s	0.427	0.211	0.123	0.153	0.173	0.300	0.515	0.752	0.928
9 m/s	0.244	0.046	0.067	0.254	0.174	0.321	0.610	0.859	0.943
12 m/s	1.593	1.167	0.536	0.629	1.081	1.274	1.600	1.675	1.680
15 m/s	2.409	2.780	3.374	4.389	3.340	2.705	2.329	2.065	1.760
20 m/s	3.460	5.053	4.102	3.619	3.036	3.364	3.716	1.276	0.934

RMS Errors in degree Kelvin.

	5 °	***15 °***	***25 °***	***35 °***	***45 °***	***55 °***	***65 °***	***75 °***	***85 °***
5 m/s	3.650	3.634	3.556	3.539	3.705	3.460	3.544	3.647	3.607
7 m/s	3.555	3.490	3.390	3.308	3.365	3.583	3.459	3.395	3.280
9 m/s	3.515	3.419	3.359	3.287	3.370	3.291	3.328	3.337	3.305
12 m/s	3.634	3.471	3.421	3.518	3.685	3.497	3.295	3.520	4.060
15 m/s	3.719	3.692	3.807	3.787	4.023	3.825	3.555	3.496	3.325
20 m/s	2.894	3.973	3.541	5.009	4.345	5.534	5.648	6.301	5.051
	95 °	***105 °***	***115 °***	***125 °***	***135 °***	***145 °***	***155 °***	***165 °***	***175 °***
5 m/s	3.734	3.562	3.591	3.606	3.582	3.584	3.585	3.494	3.462
7 m/s	3.221	3.231	3.221	3.243	3.277	3.357	3.476	3.421	3.387
9 m/s	3.143	3.096	3.174	3.341	3.409	3.438	3.514	3.576	3.490
12 m/s	3.418	3.298	3.308	3.457	3.388	3.460	3.606	3.559	3.644
15 m/s	3.106	2.916	2.848	3.099	3.516	3.813	3.413	3.179	3.034
20 m/s	4.378	3.426	4.414	3.216	3.542	2.282	3.677	3.085	4.213
	185 °	***195 °***	***205 °***	***215 °***	***225 °***	***235 °***	***245 °***	***255 °***	***265 °***
5 m/s	3.726	3.763	3.464	3.506	3.520	3.434	3.520	3.627	3.897
7 m/s	3.430	3.391	3.333	3.271	3.273	3.348	3.357	3.475	3.625
9 m/s	3.350	3.496	3.385	3.527	3.600	3.646	3.559	3.358	3.546
12 m/s	3.607	4.168	3.708	3.800	4.302	4.116	4.271	4.421	4.538
15 m/s	3.147	3.402	3.962	4.639	4.426	4.602	4.327	4.395	4.638
20 m/s	4.423	2.927	4.006	4.117	4.056	3.429	4.413	5.324	6.483
	275 °	***285 °***	***295 °***	***305 °***	***315 °***	***325 °***	***335 °***	***345 °***	***355 °***
5 m/s	3.746	3.911	3.765	3.797	3.800	3.835	3.751	3.657	3.555
7 m/s	3.478	3.475	3.639	3.679	3.768	3.698	3.694	3.649	3.581
9 m/s	3.651	3.754	3.680	3.795	3.918	3.938	3.882	3.748	3.603
12 m/s	4.499	5.177	5.053	5.386	4.937	4.617	3.963	3.685	3.808
15 m/s	4.622	4.719	4.976	4.834	5.475	5.166	3.967	3.813	3.778
20 m/s	5.088	5.534	4.936	4.378	5.922	4.899	2.713	3.581	3.018

37 GHz

Mean Errors in degree Kelvin.

	5 °	***15 °***	***25 °***	***35 °***	***45 °***	***55 °***	***65 °***	***75 °***	***85 °***
5 m/s	0.796	0.771	0.445	0.008	-0.243	-0.444	-0.617	-0.571	-0.025
7 m/s	0.861	0.257	-0.230	-0.200	-0.393	-1.019	-1.447	-1.485	-0.890
9 m/s	1.179	0.720	0.353	0.187	-0.246	-0.884	-1.589	-1.744	-1.436
12 m/s	0.926	0.576	0.704	0.742	0.039	-0.783	-1.373	-1.794	-1.809
15 m/s	-0.948	-1.440	-1.008	-0.495	-0.784	-1.219	-2.399	-2.365	-1.938
20 m/s	-2.595	-3.039	0.615	2.564	4.323	6.215	6.481	3.587	-1.965
	95 °	***105 °***	***115 °***	***125 °***	***135 °***	***145 °***	***155 °***	***165 °***	***175 °***
5 m/s	0.319	-0.041	-0.391	-0.715	-0.526	-0.003	0.471	0.903	1.077
7 m/s	-0.601	-0.779	-1.287	-1.621	-1.595	-1.514	-1.031	-0.276	0.060
9 m/s	-1.271	-1.355	-1.598	-1.689	-2.145	-2.427	-2.543	-1.981	-0.836
12 m/s	-1.872	-1.223	-0.647	-0.559	-0.906	-1.128	-0.449	-0.346	0.374
15 m/s	-0.984	-0.798	-0.443	-0.195	-0.505	-1.020	-0.771	0.297	0.173
20 m/s	-2.958	-4.362	-2.457	-1.546	1.597	2.774	6.041	3.952	3.011
	185 °	***195 °***	***205 °***	***215 °***	***225 °***	***235 °***	***245 °***	***255 °***	***265 °***
5 m/s	1.253	1.294	1.384	1.504	1.569	1.661	1.784	1.816	1.504
7 m/s	0.348	0.595	0.928	1.159	1.157	1.390	1.600	1.768	1.654
9 m/s	0.071	0.524	0.857	1.336	1.575	1.808	1.719	1.717	1.750
12 m/s	0.562	0.700	0.851	1.221	2.250	2.322	1.117	1.134	1.414
15 m/s	-0.093	0.320	-0.007	1.129	1.457	1.083	1.270	2.115	2.543
20 m/s	5.705	0.858	2.386	2.588	4.529	1.804	3.474	3.699	2.886
	275 °	***285 °***	***295 °***	***305 °***	***315 °***	***325 °***	***335 °***	***345 °***	***355 °***
5 m/s	1.356	0.911	0.679	0.624	0.663	0.904	1.273	1.334	1.067
7 m/s	1.448	1.107	0.902	0.981	0.918	1.020	1.136	1.411	1.486
9 m/s	1.188	1.279	1.201	1.257	1.103	1.322	1.422	1.535	1.455
12 m/s	1.262	1.112	0.459	0.508	1.271	1.431	1.962	2.362	1.854
15 m/s	2.309	3.142	3.927	5.305	3.144	2.302	1.857	0.826	0.018
20 m/s	5.678	6.708	5.416	4.644	4.490	1.773	1.735	0.656	-0.472

RMS Errors in degree Kelvin.

	5 °	***15 °***	***25 °***	***35 °***	***45 °***	***55 °***	***65 °***	***75 °***	***85 °***
5 m/s	6.630	6.620	6.443	6.410	6.592	6.339	6.402	6.457	6.370
7 m/s	6.340	6.196	5.969	5.874	6.001	6.434	6.143	5.925	5.825
9 m/s	6.181	6.015	6.129	6.042	6.129	5.983	5.785	5.729	5.602
12 m/s	6.564	6.491	6.153	6.650	7.034	6.792	6.249	6.323	6.955
15 m/s	5.498	6.061	6.372	7.302	7.272	6.912	6.080	6.495	6.062
20 m/s	4.318	5.678	4.862	7.704	7.392	9.838	9.270	12.609	9.058
	95 °	***105 °***	***115 °***	***125 °***	***135 °***	***145 °***	***155 °***	***165 °***	***175 °***
5 m/s	6.652	6.615	6.604	6.597	6.381	6.426	6.415	6.293	6.168
7 m/s	5.772	5.801	5.867	5.949	6.099	6.196	6.390	6.251	6.012
9 m/s	5.271	5.347	5.558	5.718	5.892	6.014	6.235	6.411	6.246
12 m/s	6.081	6.090	6.103	6.422	5.863	6.403	6.832	6.965	6.339
15 m/s	5.495	5.618	5.324	5.949	6.252	6.783	6.910	6.669	6.332
20 m/s	8.214	6.831	8.232	6.416	7.258	6.345	6.665	8.375	7.694
	185 °	***195 °***	***205 °***	***215 °***	***225 °***	***235 °***	***245 °***	***255 °***	***265 °***
5 m/s	6.537	6.568	6.093	6.029	6.125	5.976	6.065	6.183	6.588
7 m/s	5.976	5.845	5.697	5.566	5.679	5.814	5.575	5.647	5.942
9 m/s	6.011	5.932	5.661	5.719	5.846	5.851	5.731	5.380	5.601
12 m/s	6.145	6.340	5.831	6.059	6.679	6.124	6.148	6.046	5.997
15 m/s	5.908	5.707	6.044	7.014	6.194	6.336	5.868	5.619	6.086
20 m/s	7.526	4.750	6.062	5.706	5.829	6.646	5.911	7.825	9.264
	275 °	***285 °***	***295 °***	***305 °***	***315 °***	***325 °***	***335 °***	***345 °***	***355 °***
5 m/s	6.552	6.772	6.655	6.820	6.830	6.939	6.942	6.840	6.691
7 m/s	5.864	5.963	6.121	6.308	6.480	6.372	6.526	6.516	6.487
9 m/s	5.906	5.969	5.933	5.933	6.093	5.969	6.222	6.190	6.288
12 m/s	6.313	7.141	7.127	7.714	7.027	6.516	6.064	6.113	6.189
15 m/s	6.366	6.222	6.710	6.630	7.428	6.957	5.876	5.563	5.627
20 m/s	8.576	8.867	7.781	6.080	8.460	6.504	5.041	5.280	4.957

LIST OF REFERENCES

[1] C. Elanchi, *Introduction to the Physics and Techniques of Remote Sensing*. New York: John Wiley & Sons, 1987.

[2] F. T. Ulaby, R. K. Moore, and A. K. Fung, *Microwave Remote Sensing Active and Passive*, Vol. 1, *Microwave Remote Sensing Fundamentals and Radiometry*. Reading: Addison-Wesley, 1981.

[3] F. T. Ulaby, R. K. Moore, and A. K. Fung, *Microwave Remote Sensing Active and Passive*, Vol 2, *Radar Remote Sensing and Surface Scattering and Emission Theory*. Reading: Addison-Wesley, 1982.

[4] F. T. Ulaby, R. K. Moore, and A. K. Fung, *Microwave Remote Sensing Active and Passive*, Vol 3, *From Theory to Applications*. Norwood: Artech House, 1986.

[5] W. L. Jones, L. C. Schroeder, D. H. Boggs, E. M. Bracalente, R. A. Brown, G. J. Dome, W. J. Pierson, and F. J. Wentz, "The SEASAT-A satellite scatterometer: The geophysical evaluation of remote sensed wind vectors over the ocean," *J. Geophys. Res.*, vol. 87, no. C5, pp. 3297-3317, Apr. 1982.

[6] R. K. Moore and W. L. Jones, "Satellite scatterometer wind vector measurement – the legacy of the Seasat satellite scatterometer," *IEEE Geosci. Remote Sens. Newsletter*, no. 132, pp. 18-32, Sept. 2004.

[7] E. P. W. Attema, "The active microwave instrument on-board the ERS-1 satellite," *Proc. IEEE*, vol. 79, no. 6, pp. 791-799, June 1991.

[8] P. Gaiser et al., “The WindSat spaceborne polarimetric microwave radiometer: sensor description and early orbit performance,” *IEEE Trans. Geosci. Remote Sensing*, vol. 42, no. 11, pp. 2347-2361, Nov. 2004.

[9] K. Imaoka, T. Sezai, T. Takeshima, T. Kawanishi, and A. Shibata, “Instrument characteristics and calibration of AMSR and AMSR-E,” in *Proc. IGARSS*, June 2002, pp. 18-20.

[10] F. J. Wentz, “Measurement of oceanic wind vector using satellite microwave radiometers,” *IEEE Trans Geosci Remote Sens.*, vol. 30, no. 5, Sept. 1992.

[11] T. Meissner and F. Wentz, “An updated analysis of the ocean surface wind direction signal in passive microwave brightness temperature,” *IEEE Trans. Geosci Remote Sens.*, no. 6, June 2002.

[12] Z. Jelenak, T. Mavor, L. Connor and P. S. Chang, “Ocean wind vector retrievals from WindSat polarimetric measurements in extreme events 2004 hurricane season”, presented at Ocean Vector Wind Science Team Meeting, Seattle, March 2005.

[13] T. E. Oliphant and D. G. Long, “Accuracy of scatterometer derived winds using the Cramer-Rao bound,” *IEEE Trans. Geosci. Remote Sensing*, vol. 37, pp. 2642-2652, Nov. 1999. END CHAPTER 1

[14] R. K. Moore and A. D. Fung, “Radar determination of winds at sea,” *Proc. IEEE*, vol. 67, pp. 1504-1521, 1979.

[15] M. H. Freilich, D. G. Long, and M. W. Spencer, “SeaWinds: A scanning scatterometer for ADEOS II – science overview,” in *Proceedings of the International Geoscience and Remote Sensing Symposium*, 1994, pp. 960-963.

[16] M. I. Skolnik, *Introduction to Radar Systems*. New York: McGraw-Hill, 2001.

[17] F. J. Wentz, "A well calibrated ocean algorithm for special sensor microwave/imager," *J. Geophys. Res.*, vol. 102, pp. 8703-8718, 1997.

[18] L. C. Schroeder, D. H. Boggs, G. J. Dome, I. M. Halbertsam, W. L. Jones, W. J. Pierson, and F. J. Wentz, "The relationship between wind vector and normalized radar cross section used to derive SEASAT-A satellite scatterometer winds," J. Geophys. Res., vol. 87, no. C5, pp. 3318-3336, 1982.

[19] F. J. Wentz, S. Peterherych, and L. A. Thomas, "A model function for ocean radar cross sections at 14.6 GHz," J. Geophys. Res., vol. 89, no. C3, pp. 3689-3740, 1984.

[20] F. J. Wentz and D. K. Smith, "A model function for the ocean-normalized radar cross section at 14 GHz derived from NSCAT observations," *J. Geophys. Res.*, vol. 104, no. C5, pp. 11 499-11 54, May 1999.

[21] R. S. Dunbar, S. V. Hsiao, Y.-J. Kim, K. S. Pak, B. H. Weiss, and A. Zhang, "Science algorithm specification for SeaWinds on QuikSCAT and SeaWinds on ADEOS-II," Jet Propulsion Laboratory, Pasadena, CA, Tech. Rep. D-21978, 2001. END CHAPTER 2

[22] S. Soisuvarn, L. W. Jones, and Z. Jelenak, "Development of oceanic wind vector model function for AMSR radiometer on ADEOS-II satellite," *Proc. IGARSS*, 2006.

[23] L. N. Connor, P. S. Chang, Z. Jelenak, N.-Y. Wang and T. P. Mavor, "WindSat validation datasets: an overview," *Proc. IGARSS 2004*, 20-24 Sept. 2004.

[24] R. S. Dunbar (private communication), 2004.

[25] F. J. Wentz and T. Meissner, "Algorithm theoretical basis document; version 2; AMSR ocean algorithm," Remote Sensing Systems, Santa Rosa, CA, RSS Tech. Proposal 121599A-1, Nov. 2, 2000.

[26] Z. Jelenak (private communication), 2006. END CHAPTER 3

[27] C-Y. Chi, and F. K. Li, “A comparative study of several wind estimation algorithms for spaceborne scatterometers,” *IEEE Trans. Geosci Remote Sens.*, vol. 26, no. 2, Mar. 1988.

[28] R. E. Fischer, “Standard deviation of scatterometer measurements from space,” *IEEE Trans. Geosci. Electron*, vol. GE-10, pp. 106-113, March 1972.

[29] L. C. Schroeder et al., “Removal of ambiguous wind directions for a Ku-band wind scatterometer using three different azimuth angles,” *IEEE Trans. Geosci. Remote Sens.*, vol GE-23, pp. 91-100, March 1985.

[30] S. J. Shaffer, R. S. Dunbar, S. V. Hsiao, and D. G. Long, “A median-filter-based ambiguity removal algorithm for NSCAT,” I*EEE Trans. Geosci. Remote Sens.*, vol. 29, pp. 167-174, Jan. 1991. X